Journal of Catalysis 434 (2024) 115508

Contents lists available at ScienceDirect

Journal of Catalysis

journal homepage: www.elsevier.com/locate/jcat

Research article

A general method for studying reactive surface species, CT-SKAn: Charge-transfer spectrokinetic analysis

Alejandra Torres-Velasco [a,b], Bhagyesha S. Patil [a,b], Hongda Zhu [a], Yue Qi [c], Simon G. Podkolzin [c], Juan J. Bravo-Suárez [a,b,*]

[a] Center for Environmentally Beneficial Catalysis, The University of Kansas, Lawrence, KS 66047, USA
[b] Chemical & Petroleum Engineering Department, The University of Kansas, Lawrence, KS 66045, USA
[c] Department of Chemical Engineering and Materials Science, Stevens Institute of Technology, Hoboken, NJ 07030, USA

ARTICLE INFO

Keywords:
Charge transfer
Gold catalyst
Oxidation reaction
Oxygen species
In situ UV–Visible spectroscopy
Modulation excitation spectroscopy

ABSTRACT

A spectrokinetic methodology was developed to determine reactive surface species by combining operando ultraviolet–visible spectroscopy and charge transfer kinetic models. The methodology consisted of three general steps: 1) concomitant measurement of reaction rates and charge transfer via ultraviolet–visible spectroscopy; 2) development of rate expressions from kinetic models involving the adsorbed species of interest. These rate expressions relate reaction rates, charge transfer, and partial pressures of gas phase species; and 3) evaluation of the goodness of fit of the rate expressions to the experimental data. The species whose rate expressions show the best fit are the more likely reactive surface species for the studied reaction. An example is presented for the determination of reactive oxygen species during ethanol oxidation over Au/TiO_2. The charge transfer spectrokinetic analysis showed that surface hydroperoxyl, hydroxyl, and atomic oxygen species were reactive surface intermediates, whereas surface molecular oxygen was not.

1. Introduction

In heterogeneous catalysis, a powerful methodology to understand kinetic mechanisms and intermediate species is to combine kinetics, in situ/operando spectroscopy, and/or ab initio calculations. However, the combination of kinetics and spectroscopy is still in its infancy. Some examples of application of in situ spectroscopic measurements can be found in the literature for: identification of true reaction intermediates [1–4], quantification of catalysts degree of reduction [5–8], and determination of reaction rate [9], rate constant [10], and activation energies [11]. The main characteristic of these spectroscopic methods is the use of dynamic and transient conditions. Examples of these methods include jump or stopped-reactant type methods [1,9], steady-state isotopic transient kinetic analysis combined with diffuse reflectance infrared Fourier transform spectroscopy (SSITKA-DRIFTS) [2,3], and modulation excitation spectroscopy [12,13]. These techniques can provide information on active sites and intermediate species and, in some cases, their kinetic relevance, that is, if they are reactive intermediates or spectators. From these examples, in situ ultraviolet–visible (UV–Vis) spectroscopy was used to quantify the extent of reduction of transition metals [5–8] and to determine the location of adsorbed species on gold catalysts [14]. However, UV–Vis spectroscopy has rarely been employed to identify reactive surface species due to its poor specificity [15].

In the last decades, the utilization of ethanol as a feedstock to produce value-added derivatives has gained momentum. An interesting example is the direct conversion of ethanol to acetaldehyde and acetic acid in a one-step catalytic process at mild conditions and with high conversions [16–19]. Ethanol oxidation can be carried out in liquid and vapor-phase on various gold catalysts including Au/Al_2O_3, Au/TiO_2, Au/ZnO, and Au/SiO_2 [17,19–25]. In the liquid phase, ethanol oxidation with gold catalysts (i.e., Au/TiO_2, Au/ZnO, $Au/MgAl_2O_4$, Au/SiO_2) takes place in aqueous solution (~5 wt% ethanol) and at high oxygen pressures (>5 bar) to increase oxygen availability. At these conditions, the reaction proceeds with moderate ethanol conversions (up to 58 %) and high acetic acid selectivity (up to 83 %) [22]. While the liquid phase oxidation of ethanol on gold catalysts has shown an interesting catalytic performance, issues remain regarding the use of high oxygen pressures and product separation costs from dilute solutions. In the vapor phase, Haruta and co-workers investigated ethanol oxidation (100–280 °C, 1 atm, ethanol partial pressure ~ 0.8 kPa, 20000 $cm^3\,h^{-1}\,g_{cat}^{-1}$) on a variety

* Corresponding author.
E-mail address: jjbravo@ku.edu (J.J. Bravo-Suárez).

https://doi.org/10.1016/j.jcat.2024.115508
Received 29 December 2023; Received in revised form 11 April 2024; Accepted 19 April 2024
Available online 21 April 2024

of gold catalysts (Au loading 1–20.6 %). These authors found that the nature of the support (e.g., SiO_2, MoO_3, La_2O_3, ZnO, In_2O_3, MnO_2, CeO_2, Co_3O_4, and ZrO_2) had a significant impact on product selectivities and yields [26]. The different catalyst behaviors were assigned to different ethanol and surface oxygen species reactivities, but no spectroscopic evidence was provided.

Several reports can be found on in situ/operando infrared (IR) and UV–Vis spectroscopic techniques and DFT calculations to study surface reaction species and the mechanism of ethanol oxidation. For example, in situ IR was used to propose: 1) that hydroxyls density on highly dispersed Au can track with vapor phase ethanol oxidation activity on ZSM-5 and SiO_2 [27]; 2) that adsorbed bidentate ethoxy species on Au correlated with high activity and selectivity towards partial oxidation products on Co_3O_4, NiO, and CeO_2 supported Au [28]; 3) that the rate limiting step was the C-D cleavage at the Au-support interface from experiments with CH_3CD_2-OH on Au/TiO_2 [29]; 4) that reactants activation occurs near the Au-support interface during the photothermal oxidation of ethanol on Au/TiO_2 [30]; and 5) that the Au-support interface in Au/TiO_2 promotes ethanol dehydrogenation via cleavage of βC-H in the ethoxy species [31]. More recently, in situ UV–Vis was used to evidence adsorption of O_2 and H_2 species at the Au-support interface. This report employed Au maximum plasmon peak shifts (Au MaPPS) measurements in combination with Au geometric models for Au on SiO_2, Al_2O_3, ZrO_2, ZnO, and TiO_2 [14]. Moreover, recent DFT calculations of ethanol oxidation reported the formation of different oxygen species at the Au-support interface [32] and the effects of charge transfer to activate intermediate oxygen species [33,34]. Despite these advances, there is no clear consensus about the nature and kinetic relevance of active oxygen species present during reaction. Nevertheless, these experimental and theoretical results highlighted the importance of the Au-support interface where the reaction takes place between dissociated ethanol and active oxygen species.

In this work, we report a spectrokinetic methodology to study reactive surface species. This methodology named charge transfer spectrokinetic analysis (CT-SKAn) was enabled by a combination of charge transfer experiments (steady-state operando UV–Vis spectroscopy), kinetic models, and DFT calculations. An example is presented to evaluate the relevance of various surface oxygen species during ethanol oxidation on Au/TiO_2. To support the mechanistic proposal, UV–Vis Au MaPPS measurements will be shown to confirm oxygen species location at the Au-support interface. Moreover, modulation excitation – phase sensitive detection – diffuse reflectance UV–Vis (ME-PSD-UV–Vis) is used to provide information about the dependence of charge transfer on reaction conditions. Overall, the CT-SKAn methodology will show that HOO, HO, and O are kinetically relevant surface species during ethanol oxidation on Au/TiO_2.

2. Experimental section

2.1. Materials

Commercial gold catalysts: Au on titanium oxide (AUROlite™, Au/TiO_2, Au 1 ± 0.1 wt%) and Au on zinc oxide granulate (AUROlite™, Au/ZnO, Au 1 ± 0.1 wt%) were purchased from Strem Chemicals, Inc. All other chemicals including $HAuCl_4{\cdot}3H_2O$ (Alfa Aesar), silica support (SiO_2, Davisil XWP 1000A, a gift from W.R. Grace Co.), strontium titanate support ($SrTiO_3$, 99 %, metal basis, Sigma-Aldrich), barium sulfate (Sigma-Aldrich, used as a reference for UV–Vis), ethanol (99.5 %, Fisher Scientific) and HPLC grade water (Fisher Scientific) were used as received without further purification. Helium (UHP, 99.999 %), O_2 (UHP, 99.98 %), H_2 (UHP, 99.999 %), O_2 (10 % in Argon), and Argon (UHP, 99.999 %) gases were procured from Matheson. All the gas cylinders were equipped with moisture filters (Matheson, 450B series, type 451), and with oxygen (Perkin Elmer, P/N N9301179: for He, H_2, and CO), and hydrocarbons traps (Matheson, 450B series, type 454: for He, H_2, and O_2).

2.2. Catalyst preparation

Commercial Au/TiO_2 and Au/ZnO with Au loadings of ~ 1 wt%, and particle sizes around ~ 3 nm were used in this work. Two different gold deposition methods were employed to prepare other catalysts with a nominal metal loading of ~ 1 wt%: deposition–precipitation (DP) with NaOH solution as titrant for Au/$SrTiO_3$ and DP with ammonia solution titrant for Au/SiO_2. Further details on catalyst synthesis are provided in the supporting information (**Section S1**). All catalysts were calcined under static air conditions at 400 °C for 4 h (4 °C/min) in a muffle furnace (Thermolyne 48000, Barnstead International). Furthermore, after loading the catalyst in the in situ reaction cell, all the samples were pretreated in 10 %O_2/Ar at 400 °C for 1 h (10 °C/min) before reaction.

2.3. Ex situ catalyst characterization

TEM characterization was performed to determine the Au particle size distribution for the freshly calcined catalyst samples using a Hitachi Transmission Electron Microscope (Model H-8100) operated at 200 kV. In a typical analysis, a small amount of sample (~1 mg) was dispersed over a copper grid (ultrathin Lacey carbon film, 400 mesh, Ted Pella Inc.) previously soaked with ethanol. After drying the impregnated grid for five min at room temperature, TEM characterization was performed. The Au particle size distribution was determined by measuring more than 100 Au nanoparticles per sample with the ImageJ software (https://imagej.nih.gov/ij/). Elemental composition was determined by X-ray fluorescence (XRF) (PANalytical Zeltium instrument), which showed Au loadings of around ~ 1 %.

2.4. In situ UV–Vis spectroscopy H_2/O_2 cycles experiments: Au MaPPS

Au MaPPS (Au maximum plasmon peak shift) experiments were performed to determine the location of active sites for oxygen adsorption. The experimental set up and methodology are briefly described below.

2.4.1. Au MaPPS experimental set up

Au MaPPS experiments were carried out in an in situ high-temperature diffuse reflectance (DR) Harrick Scientific reaction cell. This cell was modified as previously reported [35] and with the following characteristics: a) a reduced dead volume due to glass bead addition; b) an in-house machined compact dome (blueprints and 3D model in ref. [35]) with a port for a high temperature diffuse reflectance probe and c) a thermocouple in direct contact with the catalyst sample to monitor and control the reaction temperature. The UV–Vis system consisted of a black comet (Stellar Net Inc.) UV–Vis miniature spectrometer. This unit was equipped with SL3 Deuterium and SL1-filter halogen lamps (Stellar Net) providing UV–Vis-NIR light in the 200–2300 nm range. A high temperature fiber optics probe (Avantes, FCR-7UVIR400-2-BX-HT-SR-6.35x76) was employed for in situ measurements. The UV–Vis spectra were referenced to freshly dried $BaSO_4$. The spectrometer is a concave grating equipment coupled with a CCD detector (Model C, Stellar Net). Additionally, to avoid deuterium lamp spikes, a U-330 filter was incorporated in the UV–Vis configuration. This modified reaction cell set-up enabled relatively fast UV–Vis spectra acquisition (within ~ 1 s, e.g., integration time = 700 ms, 1 scan). All spectra were collected and analyzed in the range between 250 and 1050 nm. Plots are presented as wavelength vs. pseudo absorbance, log (1/relative reflectance), which is labeled "Absorbance" for brevity.

For the Au MaPPS experiments, the meshed (38–75 μm) fresh catalysts were initially loaded to the sample cup in the UV–Vis cell (volume ~ 0.15 cm^3). The catalyst sample was then pretreated in 10 %O_2/Ar (35 cm^3/min) from 25 to 400 °C (10 °C/min). The temperature was maintained constant at 400 °C and after 1 h, the system was cooled down to 240 °C (10 °C/min). The pretreated sample was flushed with He (80 cm^3/min) for 20 min. Then, cycles between reducing and oxidizing gas

atmospheres began. In a cycle, the catalyst was exposed to pure O_2 (80 cm^3/min) for 30 min, flushed with He for 20 min, and followed by pure H_2 (80 cm^3/min). This sequence was repeated two more times for a total of three complete cycles. Results for four different gold catalysts (Au/TiO_2, Au/SiO_2, Au/$SrTiO_3$, and Au/ZnO) were also presented for comparison and to show the sensitivity and reproducibility of the measurements. All transfer lines to and from the in situ cell were heated (~80 °C) to avoid condensation of reactants and products.

2.4.2. Au MaPPS data analysis

The Au MaPPS is a relatively new method, and it is key to support our mechanistic proposal for ethanol oxidation at the metal-support interface. Therefore, it will be described in detail to ensure its reproducibility and impact. A large data set of in situ UV–Vis spectra was collected. This required an in-house Python code for the automated measurement of the gold plasmon resonance peaks. The software code was used to fit the spectra around the Au plasmon peak to a polynomial of order 5. This fitting procedure reduced data noise and facilitated the location of the plasmon maximum. Next, the general Au MaPPS methodology is described.

A. Multiple UV–Vis spectra are collected to cover the plasmon region. This could be done at steady state (as in this study) or under dynamic conditions (e.g., jump methods, MES, etc.).
B. The Au plasmon maximum is determined at the reaction conditions of interest, preferably by an automated method as described above, to minimize human error and bias.
C. The relative charge transfer change from reducing to oxidizing conditions or vice versa is determined by the following correlation [14]:

$$\frac{\Delta N}{N} = \frac{\lambda_m^2}{\lambda^2} - 1 \quad (1)$$

Where $\Delta N/N$ is the relative charge transfer change from/to Au, λ_m is the wavelength corresponding to maximum absorption (in reducing conditions), N is to the initial charge density (in reducing conditions), and λ is the shifted wavelength maximum after charge transfer.

D. A plot of the fraction of Au surface atoms vs. Au particle diameter is created as previously reported [14] (see Tables S1-S4). The plot can be made considering the fraction of different coordinatively unsaturated Au sites.
E. The relative charge transfer equation (ΔN/N) corresponds to the ratio of a surface phenomenon accounting for the charge change ΔN due to adsorption as measured by UV–Vis (a bulk technique). Therefore, the ΔN/N can be plotted directly in the Au dispersion figure to correlate the adsorption sites.

2.5. Modulation excitation spectroscopy (MES): In situ diffuse reflectance UV–Visible spectroscopy during dynamic ethanol oxidation

Diffuse reflectance UV–visible spectroscopy can be combined with MES and phase sensitive detection via Fourier analysis (ME-PSD-DR-UV–Vis or ME-UV–Vis for brevity). This combination provides significantly more sensitivity for the detection of likely intermediate species relative to other spectroscopic techniques. ME-UV–Vis was carried out to explore charge transfer on gold (e.g., plasmon) or the support (e.g., d-d transitions). The experimental set up and methodology followed closely those recently described for modulation excitation diffuse reflectance infrared Fourier transform spectroscopy (ME-DRIFTS) [13].

2.5.1. ME-UV–Vis experimental set up and procedure

A general representation of the in situ ME-UV–Vis system for the modulation excitation spectroscopy experiments is shown in Fig. 1. The in situ set up is composed of a system that feeds a reactant to the in situ cell such that its concentration changes in a periodic manner. This is

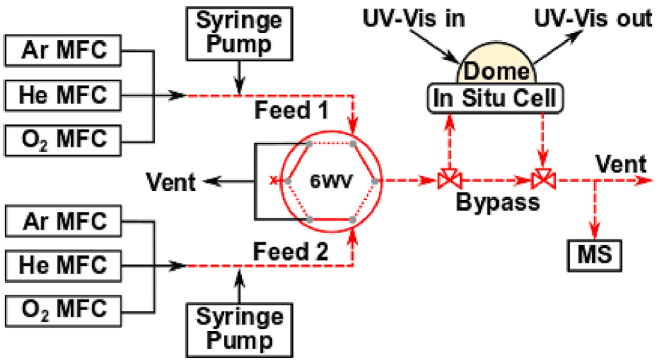

Fig. 1. Schematic representation of the in situ/operando ME-UV–Vis spectroscopic system. MFC = mass flow controller; 6WV = 6-port two position (dotted and solid lines) switching valve; MS = mass spectrometer; UV–Vis = UV–Vis light. The dotted and red color lines indicate that transfer lines are heated to avoid vapor condensation. (For interpretation of the references to color in this figure legend, the reader is referred to the web version of this article.) Adapted from ref. [36]

achieved in the present set up with periodic switches between two feeds of different composition by using a six-way valve (also possible with a four-way valve). For the operando measurements, charge transfer was tracked by the UV–Vis spectroscopic system described for the Au MaPPS characterization in the previous section. Moreover, reactants and products concentration changes were monitored online with a mass spectrometer (Pfeiffer, OmniStar GSD 320O, MS) connected to the outlet line from the reaction cell.

The ME-UV–Vis procedure consisted of modulating O_2 concentration during ethanol oxidation reaction at 240 °C. The partial pressure of O_2 was switched periodically between two feeds of 0 kPa (He/EtOH/O_2 = 79.2/0.8/0 cm^3/min) and 1.5 kPa (He/EtOH/O_2/Ar = 67.4/0.8/1.2/10.7 cm^3/min) via a LabVIEW 2018 VI program routine. Liquid ethanol (at ambient temperature) was fed with a high-pressure syringe pump (New Era Pump Systems, NE-8000X2) and gastight syringes (Hamilton) to keep a constant ethanol partial pressure of 1 kPa. It was introduced to the gas lines via an ultra-Torr fitting (Swagelok, SS-4-UT-1–2) and a high temperature septum (Restek). In a typical run, ethanol was injected at a flow rate of 126 μL/h and with He/Ar balance to 101 kPa. In the MES experiments, a fundamental modulation frequency of 0.011 Hz (1 period/90 s) and 20 periods were employed. UV–Vis spectra were also collected simultaneously at a scan rate of ~ 1 spectrum per second. This rapid spectra acquisition is needed so that the time to collect one spectrum was approximately equal to the average gas residence time in the cell. Moreover, the ~1 spectrum per second scan rate also complies with the Nyquist-Shannon spectra sampling criterion for a modulation frequency of ~0.01 Hz [13].

2.5.2. ME-UV–Vis spectroscopic data analysis procedure via phase sensitive detection

The modulation excitation spectroscopy methodology for in situ characterization is based on a periodic perturbation to the reaction system (in this case, a concentration perturbation), which allows Fourier analysis of the data. At these conditions, the phase sensitive detection (PSD) procedure can be applied to eliminate signals arising from species that do not respond (i.e., spectators) or that respond at frequencies slower than the perturbation frequency. After PSD, the resulting spectra have enhanced signal/noise ratio. The PSD applied to modulated UV–Vis spectra follows general steps previously reported and which are described next [13].

A. UV–Vis spectra are collected rapidly and continuously (equally spaced in time) to capture surface changes as the periodic gas

concentrations occur. This set of spectra is called to be in the time domain.

B. Spectra are processed by an in-house Python code following the general algorithm:

a. Read spectra in the time domain.

b. Process time domain spectra using the Fourier transform (FT) equation:

$$F(\omega) = \frac{1}{2\pi}\int_{-\infty}^{\infty} f(t)e^{-i\omega t}dt \quad (2)$$

This equation is applied, but in its discrete Fourier transform (DFT) form to the spectral data sets. More conveniently, this is done in Python with the function "fft" via the fast Fourier transform (FFT) algorithm, which converts time domain data into the frequency domain. Application of the function fftshift further sorts the obtained frequencies from minimum to maximum values. The resulting data will contain spectral response vs frequency in what is called the frequency domain [13].

c. Filter frequencies (in the frequency domain) by selecting a frequency (e.g., usually the fundamental frequency of feed modulation or a higher harmonic, if desired) or a frequency range of interest.

d. Process frequency domain data from step c using the inverse Fourier transform (FT) equation:

$$f(t) = \int_{-\infty}^{\infty} F(\omega)e^{i\omega t}d\omega \quad (3)$$

As in the case of the FT (step b above), this equation is applied, but in its inverse discrete Fourier transform (IDFT) form to the spectral data sets. This is done within Python with the function "ifft", which will convert the "filtered" frequency domain data back into the time domain. The resulting data are an average of all the periods taken and can be plotted as spectral response vs time plot in what is usually called the "phase domain" because the time range is only for a single period (T). Thus, if the data is plotted in time units, it refers to the time but with respect to that of a single period. In short, this "phase domain" (from 0-T seconds, 0–360° or 0-2π radians) will contain averaged and filtered data with high sensitivity of species that respond to the modulation. The data filtering procedure can be performed on a single frequency or frequency range. If the filtered frequency is the fundamental one, then the data obtained in the "phase domain" corresponds to the sinusoidal contribution to the input modulation waveform. This will always be the case regardless of the waveform shape of the gas or surface species. The species showing in the phase domain are more likely to be intermediate species in the reaction provided that an adequate modulation frequency is employed (e.g., usually within an order of magnitude of the turnover frequency).

This FT-Filter-IFT process is what constitutes the phase sensitive detection (PSD) in MES. As developed in our group and described above, it is quite powerful. It is completely blind to the waveform of the responding system species, which is not necessarily the same waveform of the input perturbation as usually assumed. A schematic representation of the ME-PSD procedure applied to spectra processing is shown in Fig. 2.

Two additional aspects need further comments in the application of ME-UV–Vis: the need to remove possible support contributions and the extent to which the small reported absorbances are meaningful. In the present work, there is the possibility that the reaction can occur on the bare support, leading to TiO_2 reduction. In such a case, the support contribution will need to be excluded, for example, by difference spectra in the frequency domain. This is typically done with data from identical runs at reaction conditions for catalyst and support. A comparison of ME-UV–Vis spectra of ethanol oxidation during O_2 modulation on Au/TiO_2 and TiO_2 support (**Figure S1**) shows the absence of noticeable support reduction in the d-d region at the fundamental frequency. Because of this, absorbance values on Au/TiO_2 are not expected to be significantly affected by support contributions. Please refer to the last section in the Supporting Information (**Section S7**) with an additional tutorial on how to understand UV–Vis modulation excitation spectroscopy experiments and results. This tutorial includes detailed explanations and examples on how to read and interpret time domain, frequency domain, and phase domain plots. Moreover, a section was added to discuss the issue of background (e.g., support) contributions to in situ/operando spectra for steady-state time domain and MES phase domain data. A mathematical description and examples are also presented for performing MES difference spectra in the frequency domain including phase alignment, scaling, and offsetting.

There is also the question of when changes in absorbance values in MES are meaningful. As previously discussed [12,13], MES absorbance values will be significant if they are shown to respond to perturbations beyond an acceptable value. For example, **Figure S2** shows the frequency domain plots for O_2-ME-UV–Vis on TiO_2 corresponding to a wavelength of 900 nm (d-d transition region). Its absorbance intensity at the fundamental frequency (an indicator of response to the perturbation) is comparable to the baseline noise level. This indicates that this absorbance is not meaningful. In the case of O_2-ME-UV–Vis on Au/TiO_2 (**Figure S3**), the corresponding absorbance intensity is meaningful as it is significantly larger than the baseline noise level. These results validate the use of the d-d transition region in Au/TiO_2 as a descriptor of charge transfer in ME-UV–Vis and the CT-SKAn methodology.

2.6. *Charge transfer spectrokinetic analysis (CT-SKAn) Methodology: Ethanol oxidation on Au/TiO_2*

In the analysis of catalytic reactions via classical kinetics, mechanisms are commonly evaluated from the goodness of fit of derived Langmuir-Hinshelwood rate expressions to the experimental data. It is also well-known that a mechanism cannot be proved or disproved based on the validity of these rate expressions as different mechanisms can

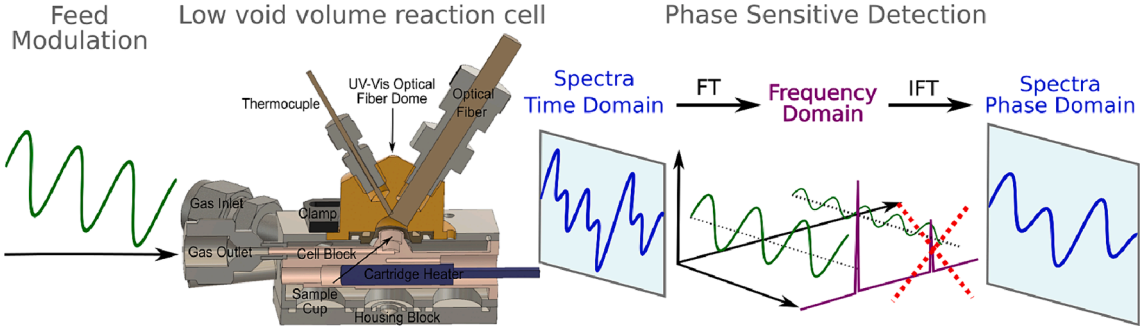

Fig. 2. Schematics for the concentration modulation excitation diffuse reflectance UV–Visible spectroscopy (ME-PSD-UV–Vis) methodology via phase sensitive detection.
Adapted from Ref. [36]

lead to kinetically undistinguishable rate expressions [37]. To differentiate these mechanisms, additional in situ spectroscopic or theoretical evidence must also be used. UV–Vis spectroscopy has been previously combined with kinetic models; however, the main objectives in these past reports were to extract active site (e.g., transition metal oxides) density [5,38] and reduction kinetics [7]. Herrmann employed simple kinetic models for reactive species discrimination with in situ conductivity (not spectroscopic) measurements [39], but details on this method were lacking. In the present work, we evaluate kinetic models of reactive surface species with classical kinetics including charge transfer characterization via in situ/operando UV–Vis spectroscopy. This methodology primarily relies on: 1) classical kinetics to derive reaction rate expressions that relate reaction rate, charge transfer, and partial pressures of reactant/product species; 2) in situ UV–Vis spectroscopy to determine charge transfer changes at reaction conditions; and 3) DFT calculations to provide an estimate of the relative charge transfer change of relevant surface species. Another key aspect of the CT-SKAn methodology is that it can be used for most catalytic mechanisms even in the presence of internal mass transfer limitations. This is because the observed reaction rate order dependence of reacting species in most elementary steps is the same as the intrinsic reaction rate order (see **Section S2** in the Supporting Information for derivation). It should also be noted that we used steady-state spectroscopic experiments rather than MES ones for kinetic model discrimination. This choice was made for simplicity because the MS and UV–Vis data in the MES experiments would need to be synchronized. A synchronization procedure would consist of modelling gas mixing in the reaction cell, transfer lines, and MS chamber such that in situ cell gas concentrations could be back calculated from downstream MS data [13,35,36]. Next, we will describe the application of the CT-SKAn (charge transfer spectrokinetic analysis) methodology to ethanol oxidation on Au/TiO_2 to evaluate the most likely reactive surface oxygen species.

2.6.1. CT-SKAn experimental set up

The present CT-SKAn methodology includes operando measurements (i.e., reactant and product partial pressures and UV–Vis spectroscopy) at different reaction conditions during ethanol oxidation. The in situ reaction cell used for the steady state measurements and UV–Vis spectrometer were the same as those described previously in **Section 2.4.1**. Once the catalyst was loaded, it was also pretreated in an identical manner, in a flow of 10 %O_2/Ar at 400 °C (10 °C/min) for 1 h. Then, the temperature was set to 240 °C at a fixed ethanol partial pressure of 1 kPa and oxygen partial pressures between 0.8 and 1.5 kPa (at increases of ~ 0.2 kPa). For all these reaction conditions, the concentrations of ethanol and oxygen were tracked with an online mass spectrometer. More details on the experimental methodology and MS data analysis are provided in **Sections S4** and **S5** in the Supporting Information.

2.6.2. CT-SKAn methodology description

The CT-SKAn methodology is based on the UV–Vis spectrokinetic analysis (from d-d transitions in the 900–1000 nm region) of various charge transfer (CT) kinetic models. A key requirement in this methodology is the need to consider electron transfer in the elementary steps. In the ethanol oxidation example, charge transfer was included in the H adsorption (from ethanol dehydrogenation) and oxygen activation steps. This is justified since electron transfer to TiO_2 was reported when H_2 adsorbs on Au/TiO_2 [40,41]. Moreover, DFT calculations have demonstrated that O_2 accepts electronic charge upon activation at the Au/TiO_2 perimeter [42]. It is also worth noting that if the predominant species in charge transfer steps are also species in kinetically relevant steps, then the relative charge transfer in the catalytic cycle should also be limited by the rate determining step. When these conditions are met, the CT spectroscopic measurements at different reaction conditions should reflect the relative change of the CT captured in the kinetic model. If the bare TiO_2, away from the Au/TiO_2 interface, undergoes significant charge transfer at reaction conditions, then the above description implies the need to subtract bare support contributions. This would be the case because two possible reaction zones are considered: 1) a primary zone in the vicinity of Au/TiO_2 interface [43,44] and 2) an extended reaction zone on the bare support far away from the Au/TiO_2 interface. Our main interest is in the primary reaction zone, where it is surmised that charge transfer via the support activates O_2. Electron transfer occurs during ethanol dehydrogenation on Au which transfers to the Au/TiO_2 interface where the support is partially reduced. If any reaction occurs in the extended reaction zone, the bare TiO_2 support contribution to charge transfer in the Au/TiO_2 catalyst is accounted for by a difference spectra procedure (see Supporting Information, **Sections S4** and **S7**, for more details). In what follows, we explain the CT-SKAn experimental measurements and calculations for the ethanol oxidation case.

A. CT-kinetic models are developed for each intermediate species of interest (in this work, different active surface oxygen species) according to the Langmuir-Hinshelwood formalism. Therefore, reaction rate expressions in terms of the oxygen partial pressure and relative charge transfer were derived for the following elementary steps and assumptions: 1) oxygen and ethanol adsorption were considered to be quasi-equilibrated steps; 2) the concentration of vacant sites was assumed to be constant in the range of the used experimental conditions; 3) the step involving the reaction between the adsorbed ethoxy and the intermediate oxygen species was defined as rate-determining; 4) the quasi-steady state assumption was applied to the surface oxygen species of interest. A detailed derivation for one of the species considered in the analysis (adsorbed atomic oxygen, O^{n-}■) is presented next, where "*" and "■" correspond to Au and Au-support interface sites, respectively (see **Section S3** in the Supporting Information for other derivations).

a. Set of elementary steps considered for acetaldehyde formation:

$$CH_3CH_2OH + * + \blacksquare \rightleftharpoons CH_3CH_2O* + H\blacksquare \quad (1)$$

$$O_2 + \blacksquare \rightleftharpoons O_2\blacksquare \quad (2)$$

$$H\blacksquare \rightleftharpoons H^{n+}\blacksquare + ne^- \quad (3a)$$

$$O_2\blacksquare + 2ne^- + \blacksquare \rightarrow 2O^{n-}\blacksquare \quad (3b)$$

$$CH_3CH_2O* + O^{n-}\blacksquare \rightleftharpoons CH_3CHO* + HO\blacksquare + ne^- \quad (4)$$

$$H^{n+}\blacksquare + O^{n-}\blacksquare \rightleftharpoons HO\blacksquare + \blacksquare \quad (5)$$

$$H\blacksquare + HO\blacksquare \rightleftharpoons H_2O\blacksquare + \blacksquare \quad (6)$$

$$CH_3CHO* \rightleftharpoons CH_3CHO + * \quad (7)$$

$$H_2O\blacksquare \rightleftharpoons H_2O + \blacksquare \quad (8)$$

b. Reaction rate expression for a fast and irreversible oxygen activation, (i.e., $r_{+3b} \gg r_{-3b}$):

$$r_{3b} = k_{3b}[O_2\blacksquare][e^-]^{2n}[\blacksquare]$$

c. Quasi-equilibrium assumption for O_2 adsorption:

$$r_2 = k_{+2}[O_2][\blacksquare] - k_{-2}[O_2\blacksquare], \text{ since } r_2/k_{+2} \approx 0$$

$$[O_2\blacksquare] = K_2[O_2][\blacksquare]$$

Then,

$$r_{3b} = k'_{3b}P_{O_2}[e^-]^{2n}$$

Where:

$$k'_{3b} = \frac{k_{3b}K_2[\blacksquare]^2}{RT}$$

d. Reaction rate expression for the rate determining step:

$$r_4 = k_4[O^{n-}\blacksquare][CH_3CH_2O^*] = r(RDS)$$

e. Pseudo steady-state assumption for $O^{n-}\blacksquare$:

$$\frac{d[O^{n-}\blacksquare]}{dt} = 2r_{3b} - r_4$$

$$\frac{d[O^{n-}\blacksquare]}{dt} = 2k'_{3b}P_{O_2}[e^-]^{2n} - k_4[O^{n-}\blacksquare][CH_3CH_2O^*] \cong 0$$

$$[e^-]^{2n} = \frac{k_4[O^{n-}\blacksquare][CH_3CH_2O^*]}{2k'_{3b}P_{O_2}}$$

$$[e^-] = \left(\frac{r}{2k'_{3b}P_{O_2}}\right)^{\frac{1}{2n}}$$

Thus, a kinetic model can be derived that relates CT ([e-] from UV–Vis), reaction rate, and O_2 partial pressure (from MS), and net charge transfer (from DFT). Other derivations are presented in the Supplementary Information.

B. UV–Vis spectra and outlet species concentrations are collected simultaneously in the in situ set up under steady state conditions (i.e., in operando mode), as described above.
C. The net charge transfer (n) for each surface oxygen species is determined from DFT calculations on a Au_5/Ti(101) model surface. This is done by quantifying the net charge change on Au and the adsorbed species in going from reactants to products in the rate determining step.
D. The collected experimental data (i.e., reaction rates, average O_2 partial pressure, and absorbance in the d-d transition region - a proxy for charge transfer) are fitted with the reaction rate models (as done in classical reaction kinetics). Then, the surface oxygen species whose model provides the best fit is the most likely kinetically relevant surface species.

2.7. DFT computational methods

Gradient-corrected spin-polarized periodic DFT calculations with the DMol^3 code in Materials Studio 2017 (Dassault Systèmes BIOVIA Corp.) were performed for determining geometries and energies of dissociatively adsorbed ethanol ($CH_3CH_2O^* + H\blacksquare$) and molecularly adsorbed acetaldehyde (CH_3CHO^*) on Au/TiO_2. The reacting ethanol was calculated in the presence of one of the following four possible adsorbed oxidizing species: atomic oxygen ($O\blacksquare$), hydroxyl ($HO\blacksquare$), molecular oxygen ($O_2\blacksquare$) or hydroperoxyl ($HOO\blacksquare$). The produced acetaldehyde was calculated in the presence of the corresponding four reduced species (resulting from the original oxidizing species plus an added H atom from ethanol): hydroxyl ($HO\blacksquare$), water ($H_2O\blacksquare$), hydroperoxyl ($HOO\blacksquare$) or hydrogen peroxide ($H_2O_2\blacksquare$). The energy differences between the corresponding acetaldehyde and ethanol structures yielded the reaction energies for ethanol oxidation to acetaldehyde by each of the four possible oxidizing species. In addition, geometries and energies of molecular and atomic oxygen adsorbed directly on Au and at the Au-TiO_2 interface were calculated and compared. Moreover, partial atomic charges for all structures were calculated with the Hirshfeld method.

Au nanoparticles supported on TiO_2 are typically modeled with small Au clusters. Recent examples by different groups and applications include: 1) oxygen dissociation on Au_5 [45], 2) hydrogen spillover on Au/TiO_2 (Au_1-Au_{13} used as models) [46], and 3) role of dispersion forces for Au_4 on TiO_2 [47]. Here, Au/TiO_2 was modeled as a Au_5 cluster supported on an infinite TiO_2(1 0 1) surface (Fig. 3). The use of this small Au cluster to model a Au nanoparticle is justifiable because we are interested in relative charge changes and general trends, not in absolute values. More importantly, the Au_5 model used in the current study is a calibrated model used in multiple previous studies. For example, the same Au_5 cluster was used for studying the vibrational frequencies of hydroxyls and the reaction of ethanol oxidation on Au/ZSM-5 [27], for the spectroscopic identification of oxygen structures on Au supported on SiO_2 [27,48] and for the kinetic study of water formation on Au supported on SiO_2, S-1 and TS-1 [49]. The infinite TiO_2(1 0 1) surface was constructed using a periodic unit cell with two layers. Each layer had an upper sublayer with 4×2 surface Ti atoms and a lower sublayer with the same number of atoms for a total of $8 \times 2 \times 2 = 32$ Ti atoms in both layers. Overall, the TiO_2 periodic unit cell had 96 atoms (32 Ti atoms and 64O atoms). The unit cell was generated from the corresponding bulk TiO_2 crystal with the optimized lattice constants of $a = b = 0.3820$ nm (within 0.6 % of the 0.3796 nm experimental value) and $c = 0.9616$ nm (within 1.8 % of the 0.9444 nm experimental value). A vacuum spacing of 4 nm was used for the constructed TiO_2(1 0 1) surface in the c direction. All atoms were optimized, simulating surface relaxation after adsorption. Similarly constructed periodic surfaces were previously used for studying adsorption and reactions on other catalytic surfaces [50–57]. For keeping the number of electrons even in all structures, a H atom bonded to a surface O atom of TiO_2, producing a surface hydroxyl, was added to the structures with an odd number of electrons. For simplicity, this additional H atom is not shown in Fig. 9. All other H atoms are shown, including the H atom produced by breaking the O–H bond in ethanol on dissociative adsorption.

The calculations used the double numerical with polarization (DNP) basis set and the generalized gradient-corrected Perdew – Wang (GGA PW91) functional. Tightly bound core electrons of Ti and Au were represented with semicore pseudopotentials. Reciprocal-space integration over the Brillouin zone was performed using the Monkhorst-Pack grid of $1 \times 1 \times 1$. A value of 0.08 for both charge and spin density mixing with direct inversion in the iterative subspace (DIIS) and orbital occupancy with thermal smearing of 0.002 Ha were used. The orbital cutoff distance of 0.52 nm was set for all atoms. All energies were calculated at 0 K

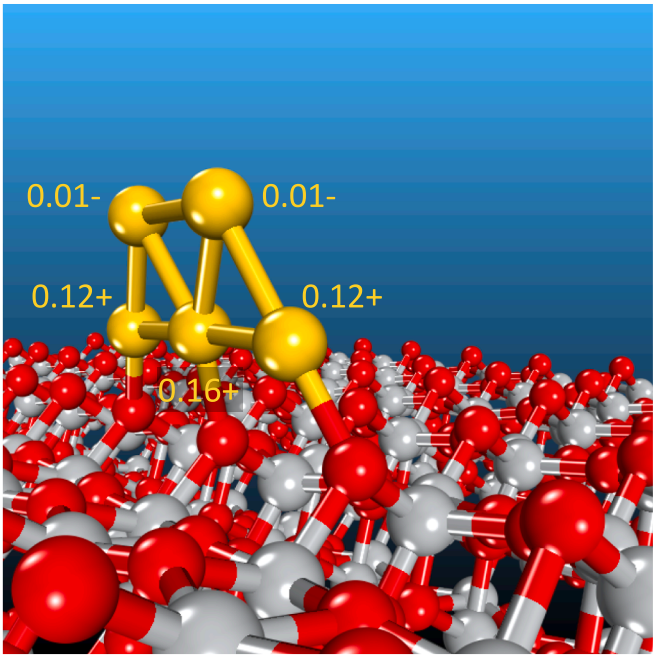

Fig. 3. Au/TiO_2 computational model: Au_5 cluster on an infinite TiO_2(1 0 1) surface. The numbers show the calculated Hirshfeld partial charges for the Au atoms.

without zero-point energy corrections. The same computational settings were previously used for studying hydrodeoxygenation of acetic acid on Pt and Ni [58], which is essentially the reverse reaction of ethanol oxidation. Similar computational settings were previously used for studying adsorption and reactions of other molecules on other catalytic surfaces [59–62].

Frequency calculations were performed using a partial Hessian matrix for adsorbed oxygen structures. The vibrational frequencies are reported as calculated, without any adjustments. The same methodology was previously used for calculating the vibrational frequencies of oxygen structures adsorbed on unsupported Au [48] and Ag [63].

3. Results and discussion

3.1. Au MaPPS

The location of catalyst adsorption sites was assessed via Au MaPPS experiments (**Section 2.4**). Au MaPPS studies have been reported on Au/TiO_2 at 125 °C for the analysis of O_2 and H_2 adsorption sites [14]. However, due to the high relevance of this methodology for ethanol oxidation mechanism, a summary will be presented of the experimental findings at 125 and 240 °C. Fig. 4 presents the gold plasmon peak position in Au/TiO_2 during cyclic and alternating O_2 and H_2 exposure at 240 °C. These results show that the Au plasmon peak shifted to higher wavelengths (red shift, lower energy) under O_2 exposure due to CT from Au to O_2. The relatively large Au MaPPS change (from ~ 548 to ~ 558 nm) was consistent with a high Au dispersion on the TiO_2 support [14]. This CT from Au to O_2 has also been evidenced by in situ XANES during the partial oxidation of propane on Au/TiO_2 [64,65].

Fig. 5 shows the Au MaPPS results for H_2/O_2 adsorption on Au/TiO_2 (Au particle size ~ 3 nm) at 240 °C alongside previously reported results at 125 °C [14]. The Au MaPPS analysis indicated that at ethanol reaction temperature the O_2 species adsorbed preferentially at the metal-support perimeter interface. The DFT results that compare oxygen adsorption on Au and at the Au-TiO_2 interface in Fig. 6 provide an explanation for this result. The molecular oxygen adsorbed at the Au-TiO_2 interface with a calculated ν (O═O) of 881 cm^{-1} (Fig. 6**c**) is predicted to be more stable by 88 kJ/mol compared to the molecular oxygen adsorbed directly on Au with a calculated ν(O═O) of 1024 cm^{-1} (Fig. 6**a**). Similarly, the atomic oxygen adsorbed at the Au-TiO_2 interface with a calculated ν(Au—O) of 390 cm^{-1} (Fig. 6**d**) is predicted to be more stable by 211 kJ/mol compared to the atomic oxygen adsorbed directly on Au with calculated ν_s(AuOAu) of 467 cm^{-1} and ν_{as}(AuOAu) of 413 cm^{-1} (Fig. 6**b**). The preferential adsorption of oxygen on Au-support perimeter sites is also in agreement with previous DFT studies. For example, low activation barriers were found for O_2 adsorption when H_2 is present

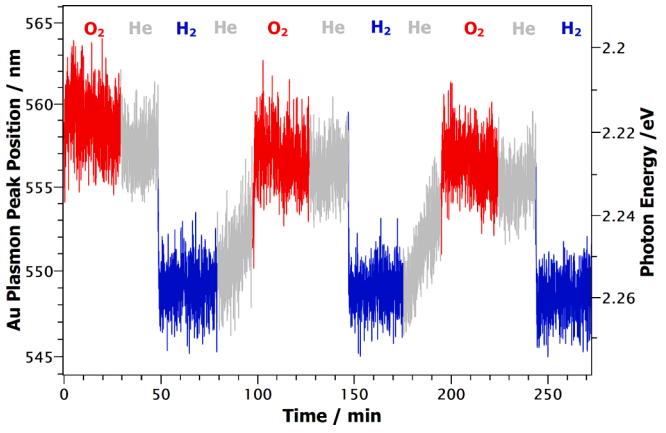

Fig. 4. Au MaPPS on Au/TiO_2 as determined from in situ UV–Vis spectroscopy during catalyst exposure to cyclic and alternating O_2 and H_2 at 240 °C. A relative charge transfer ΔN/N = 0.031 was calculated (Equation 1).

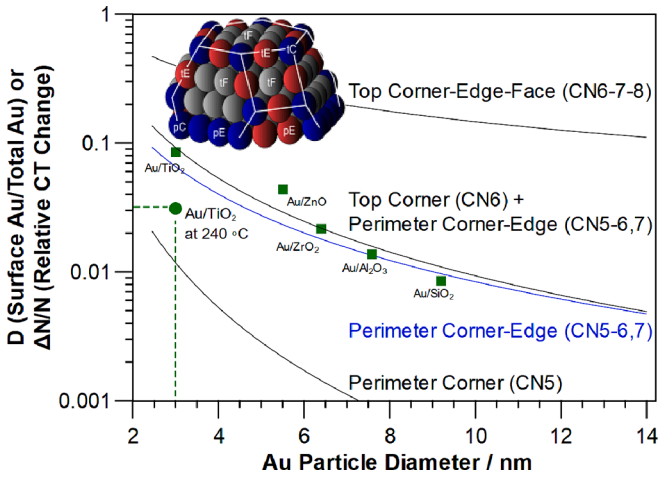

Fig. 5. Gold particle diameter vs dispersion (D) and ΔN/N on gold catalysts. Results from O_2/H_2 Au MaPPS at 125 °C (■) are presented for comparison. The result for Au/TiO_2 at 240 °C is shown as a solid circle (●). D is defined as the fraction of surface gold atoms in a nanoparticle. ΔN/N is the fraction of charge transfer as determined from Au plasmon peak shifts in flowing O_2 and H_2 (Equation 1). A Au nanoparticle with truncated octahedron geometry was used for the calculations (inset figure: p = perimeter, t = top, C: corner, E: edge, and F: face atoms with different coordination, CN5, CN6, etc).
reproduced from Ref. [14]

as a coadsorbate [66]. In the case of CO oxidation, it has also been postulated that O_2 adsorption takes place at the Au/TiO_2 perimeter interface [43,44]. Moreover, the ΔN/N calculated for Au/TiO_2 at 240 °C was lower than that reported by Srinivasan et al. [14] on Au/TiO_2 at 125 °C. This indicates a decrease in adsorbed species, which is consistent with a relatively smaller adsorption equilibrium constant at the higher temperature of 240 °C. The results of Fig. 5 also suggest that at higher temperatures, lower coordinated sites (e.g., perimeter corner sites) become more kinetically relevant. Similar findings were also reported by Ribeiro and coworkers who proposed that Au corner sites were the most active sites for the water–gas shift reaction at 120 °C on Au/Al_2O_3 and Au/TiO_2 catalysts [67].

3.2. ME-UV–Vis on Au/TiO_2 during ethanol oxidation

ME-UV–Vis was performed during ethanol oxidation at 240 °C at a constant ethanol concentration (1 kPa) and by modulating the O_2 partial pressure (1/90 Hz, ~0–1.5 kPa). This MES experiment allowed a rapid survey of the charge transfer (CT) processes taking place in the catalytic system. Fig. 7 presents the ME-UV–Vis time domain spectra during ethanol oxidation on Au/TiO_2 for the lowest and highest concentrations of O_2. For comparison, ME-UV–Vis for other metal oxide supported gold catalysts are presented in **Figure S4**. Here, changes in absorbance are noticeable in the d-d transition region but are hard to correlate with the electron transfer on the gold plasmon region. Nonetheless, all the information confined in this spectral region can be amplified and better described upon application of the PSD methodology and transformed into the phase domain (Fig. 8).

Figure S5 shows the time domain data for CT changes in ME-UV–Vis during ethanol oxidation on Au/TiO_2 at a wavelength of 900 nm over 16 periods. The corresponding MS results for reactants and products species are shown in **Figure S6**. These results show qualitatively that charge transfer is sensitive to the oxygen concentration and ethanol conversion. The in situ ME-UV–Vis and MS time domain data were processed via Fourier transform (FT), which resulted in average phase domain spectra and O_2 partial pressures (**Figure S7**). The FT analysis provided signals free of the contribution of spectator species. Moreover, the results confirmed a decrease in absorbance with an increase in O_2 partial pressure because of CT from the Au-TiO_2 interface to surface O_2 species.

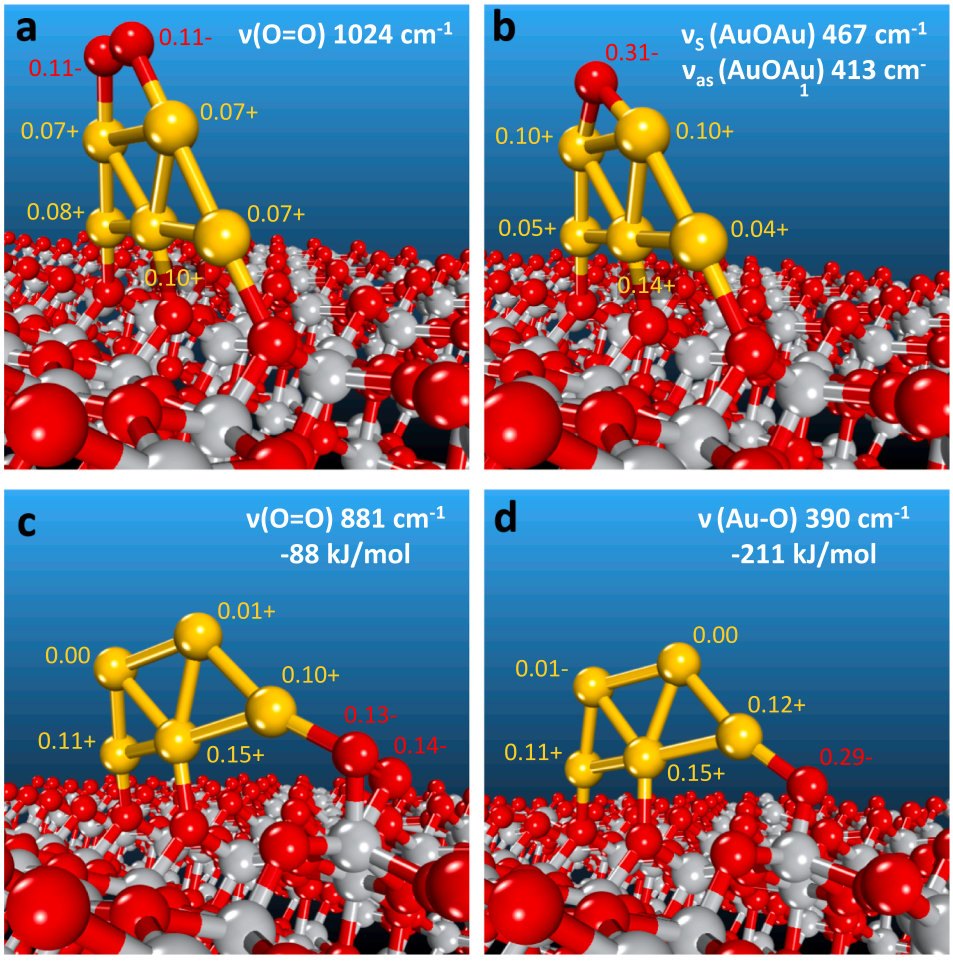

Fig. 6. DFT calculations for oxygen adsorption on Au and at the Au-TiO_2 interface. The top row shows oxygen adsorbed on Au: (**a**) molecular oxygen, (**b**) atomic oxygen. The bottom row shows oxygen adsorbed at the Au-TiO_2 interface: (**c**) molecular oxygen, (**d**) atomic oxygen. The numbers show the calculated vibrational frequencies for the surface oxygen species (cm^{-1}), energy differences between the adsorption at the Au-TiO_2 interface and on Au (kJ/mol) as well as Hirshfeld partial charges for the Au and O atoms.

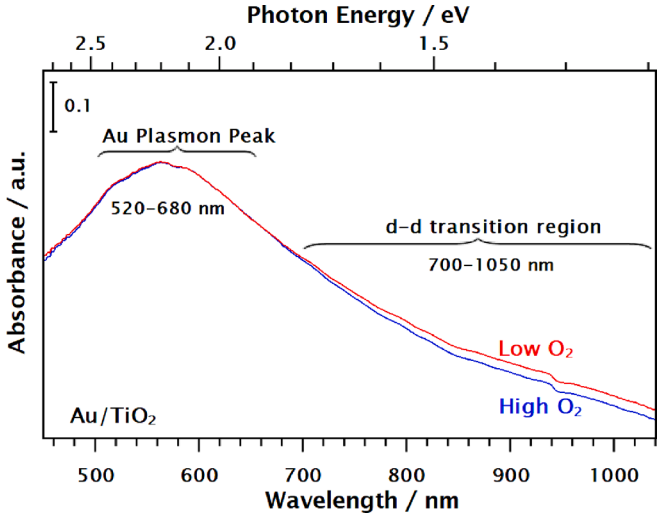

Fig. 7. In situ time domain ME-UV–vis spectra for Au/TiO_2 during O_2 modulation under ethanol oxidation at 240 °C. Conditions: 1/90 Hz, EtOH 1 kPa, with O_2 switches between 0 and 1.5 kPa.

Fig. 8 shows the phase domain trace plot spectra for ME-UV–Vis experiments during O_2 modulation (1/90 Hz, 240 °C, EtOH 1 kPa, O_2 modulation between 0 and 1.5 kPa). The band in the d-d transition region (800–1000 nm) is assigned to CT events [5,29] to/from the support in the vicinity of the Au-support interface. The relatively higher change in the intensity of this band for several gold catalysts (**Figure S8**) appears to correlate with their catalytic activity (not shown). Moreover, the opposite behavior for the CT near the gold plasmon feature (~600 nm) and d-d transition region (~900 nm) confirms the dynamics of CT between Au and the Au-TiO_2 interface [68]. This CT trend for Au/TiO_2 is also in agreement with the results for ME-UV–Vis on other gold-catalysts (**Figure S8**). The observed CT processes likely lead to the formation of active surface oxygen species as the spectra displays a more sensitive response to O_2 modulation than to ethanol modulation (**Figures S9 and S10**).

As shown in the d-d transition region of the contour plot in Fig. 9, a low concentration of O_2 tracked with high absorbance (red), evidencing CT to the support. Conversely, a high O_2 concentration led to low absorbance results (blue), indicating CT to active surface oxygen species near the Au-TiO_2 interface. These results are in line with the observed sharp drops in absorbance intensity in the time domain as O_2 was introduced to the system (**Figure S5**). Such drop suggests a mechanism involving the formation of intermediate surface oxygen species via rapid CT from the catalyst to adsorbed O_2.

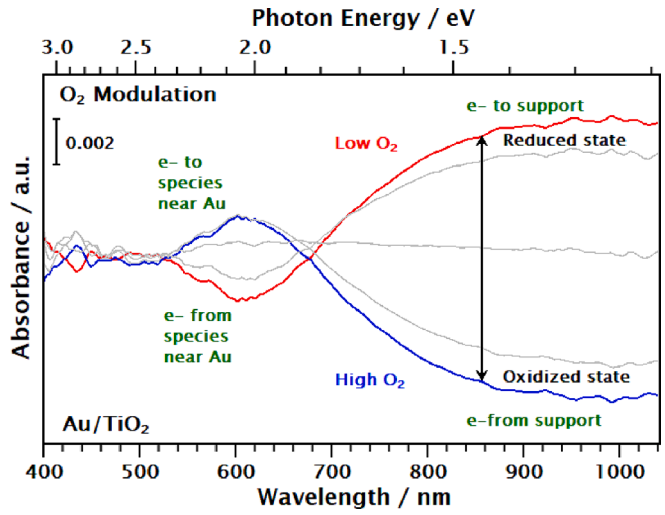

Fig. 8. Phase domain trace plot of ME-PSD-UV–Vis-NIR during ethanol oxidation during O_2 modulation on Au/TiO_2 with PSD at the fundamental frequency. Reaction conditions: Modulation from He + EtOH (1 kPa) → He + EtOH (1 kPa) + O_2 (1.5 kPa), 240 °C, input modulation frequency of 1/90 Hz. The blue (lowest) line corresponds to high O_2 (39 s in a 90 s period = phase angle of 156°) and the red (highest) line corresponds to low O_2 (84 s in a 90 s period, phase angle of 336°). (For interpretation of the references to color in this figure legend, the reader is referred to the web version of this article.)

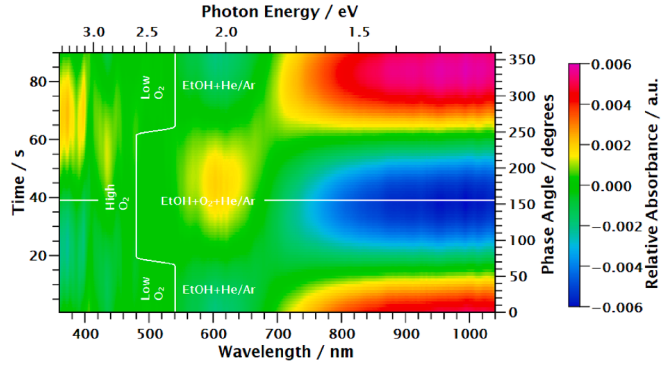

Fig. 9. Phase domain contour plot of ME-UV–Vis spectra during ethanol oxidation and O_2 modulation on Au/TiO_2 with PSD at the fundamental frequency. Reaction conditions: Modulation from He + EtOH (1 kPa) → He + EtOH (1 kPa) + O_2 (1.5 kPa), 240 °C, input modulation frequency of 1/90 Hz.

3.3. CT-SKAn on Au/TiO_2 during ethanol oxidation

There is not a clear consensus on the nature of the adsorbed oxygen species involved in the mechanism of ethanol oxidation on gold-based catalysts. However, atomic oxygen and activated molecular oxygen, among others, have been generally postulated as intermediates in the reaction [69]. For alcohol oxidation towards aldehydes and acetates, DFT calculations have shown that ethanol dissociates into ethoxy species which are oxidized by active oxygen species [70,71]. Ethanol dissociative adsorption has also been evidenced on metallic Au(1 1 1) and Au^+ in O-Au(1 1 1) [72], CeO_x-Au(1 1 1) ($Ce^{4+}/Ce^{3+}/Au^+$) [72], and TiO_2/Au(1 1 1) [73]. More importantly, DFT studies have shown that the metal-support interface enhances charge transfer from gold to O_2 to form active oxidant species during CO oxidation on Au/TiO_2 [74].

3.3.1. CT-SKAn: CT kinetic models

To study the nature of different adsorbed oxygen species such as atomic O [75,76], hydroxyl [77], or hydroperoxyl species [43,78], a charge transfer spectrokinetic analysis (CT-SKAn) was applied. The CT-SKAn methodology relates CT measurements (in the d-d transition region, ~900 nm), O_2 partial pressures (0.8–1.5 kPa), and various types of surface oxygen species including O_2^{n-}, HOO, HO, and O^{n-} through kinetic models. The operando UV–Vis measurements allowed the determination of reaction rates as a function of O_2 partial pressures. Table 1 presents the mechanisms employed to derive the CT rate expressions using the Langmuir-Hinshelwood formalism. The assumptions include: 1) the reaction predominantly occurs at the vicinity of the metal-support interface where both ethanol and O_2 adsorb in equilibrated steps; 2) activated oxygen species are quasi steady state species; 3) activated oxygen species react with ethoxy species in rate controlling steps; and 4) the density of unoccupied sites remains fairly constant at the low conversions evaluated (<15 %). The above assumptions are in concordance with the generally accepted mechanism for alcohol oxidation to aldehydes on Au catalysts. Key reported steps include [70,71]: 1) the dissociation of O–H in ethanol to give surface ethoxy species and H atoms on the metal surface and 2) β-H cleavage in the surface ethoxy intermediate resulting in acetaldehyde.

In the proposed mechanism, ethanol adsorbs on gold as supported by previously reported DFT calculations [72]. Additionally, the adsorption of oxygen species is considered to take place at the metal-support interface as evidenced via in situ Au MaPPS spectroscopic measurements. The kinetic relevance of incorporating a metal-support interface site in the mechanism of this and many other oxidation reactions has also been supported by both theoretical calculations and catalytic activity measurements [79,80]. For example, DFT calculations performed for methanol oxidation on Au/TiO_2 showed that the interface between Au and TiO_2 was essential for the activation of molecular oxygen via charge transfer [33]. Additionally, in the case of CO oxidation, a widely studied reaction on gold catalysts, DFT calculations and kinetic experiments [75] support the need for dual-site mechanisms comprising metal and metal-support interface active sites [43,44,81]. Low coordinated Au sites (predominant in small particle sizes) are expected to favor ethanol dissociation leading to H atom formation and CT to the support [40,41]. However, oxygen adsorption site requirements appear to be restricted to near interface sites for O_2 activation [33,43,82]. Hence, two active sites are needed to capture the kinetic mechanism for ethanol partial oxidation towards acetaldehyde on Au/TiO_2.

As for the rate limiting step in the mechanism, the dehydrogenation of O–H in ethanol and βC-H cleavage of surface ethoxy have been linked to kinetically controlling steps [23,83]. We performed the oxidation of ethanol (1 kPa ethanol, 1.5 kPa O_2, 240 °C) on Au/TiO_2 with C_2H_5OH, C_2D_5OD, and C_2H_5OD. It was found that only the KIE for C_2D_5OD was significant ($k_{C_2H_5OH}/k_{C_2D_5OD} \approx 1.7$ vs $k_{C_2H_5OH}/k_{C_2H_5OD} \approx 1.0$) confirming that the β-H cleavage in the surface ethoxy species was the rate determining step in the production of acetaldehyde. These results are in agreement with previous findings for acetaldehyde production on Au/$MgCuCr_2O_4$ and Au(1 1 1) surfaces [84,85]. Therefore, the βC-H cleavage of surface ethoxy was employed to understand spectrokinetically the nature of surface oxygen species using the CT-SKAn methodology described in **Section 2.6.2**.

The kinetic models shown in Table 1 (Column 3) are derived from the elementary steps described previously for different surface oxygen species. These steps are: (1, 3a) ethanol dissociative adsorption on gold with charge transfer to TiO_2 near the Au-support interface; (2, 3b) oxygen adsorption and activation at the interface via charge transfer; and (4) ethoxy partial oxidation with the activated oxygen species to form acetaldehyde in a rate determining step. In the rate expressions n is taken as the net charge transferred to the support in step 3a during ethanol dissociative adsorption. This charge also transfers from the support via the Au-support interface to the adsorbed oxygen species, so the overall net charge transfer in the catalytic cycle is zero. Here, we employed a range of O_2/ethanol ratios to provide a measurable CT response as surveyed in Fig. 8. With this experimental data the kinetic models in Table 1 for the different surface oxygen species can be evaluated. This is possible since charge transfer (ne^-) from UV–Vis d-

Table 1
Charge transfer kinetic models for different surface oxygen species (O_2^{n-}■, HOO■, HO■, O^{n-}■) during ethanol oxidation on Au/TiO_2. These models are evaluated in the CT-SKAn methodology.

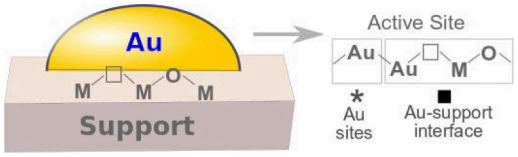

Oxygen Species	O_2 Activation and Reaction Steps	CT Model	Net DFT CT (n)
	Adsorption Steps		
	1: $CH_3CH_2OH + * + ■ \rightleftharpoons CH_3CH_2O* + H■$		
	2: $O_2 + ■ \rightleftharpoons O_2■$		
	3a: $H■ \rightleftharpoons H^{n+}■ + ne^-$		
O_2^{n-}■	3b: $O_2■ + ne^- \rightarrow O_2^{n-}■$ 4: $CH_3CH_2O* + O_2^{n-}■ \rightsquigarrow Products$	$[e^-] = (k'_{3b})^{-\frac{1}{n}} \left(\frac{r}{P_{O_2}}\right)^{\frac{1}{n}}$	0.34
HOO■	3b: $O_2■ + H^{n+}■ + ne^- \rightarrow HOO■ + ■$ 4: $CH_3CH_2O* + HOO■ \rightsquigarrow Products$	$[e^-] = (k'_{3b})^{-\frac{1}{n+1}} \left(\frac{r}{nP_{O_2}}\right)^{\frac{1}{n+1}}$	0.46
HO■	3b: $O_2■ + H^{n+}■ + ne^- \rightarrow HOO■ + ■$ 3c: $HOO■ + ■ \rightarrow O■ + HO■$ 4: $CH_3CH_2O* + HO■ \rightsquigarrow Products$	$[e^-] = (k'_{3c})^{-\frac{1}{n+1}} \left(\frac{r}{nP_{O_2}}\right)^{\frac{1}{n+1}}$	0.47
O^{n-}■	3b: $O_2■ + 2ne^- + ■ \rightarrow 2O^{n-}■$ 4: $CH_3CH_2O* + O^{n-}■ \rightsquigarrow Products$	$[e^-] = (2k'_{3b})^{-\frac{1}{2n}} \left(\frac{r}{P_{O_2}}\right)^{\frac{1}{2n}}$	0.38

d transition region, reaction rates (r), and O_2 partial pressures (P_{O2}) can be determined experimentally from operando UV–Vis. Reaction rate expressions relating charge transfer (CT) magnitudes, reaction rates, and partial pressures of species have been proposed previously by Herrmann for the identification of active oxygen species in CO oxidation (400–480 °C). However, Herrmann's approach involved the use of a catalyst' electrical conductivity (σ) as a descriptor for charge transfer, catalytic activity, and a Langmuir-Hinshelwood rate expression. His main assumption was the requirement of transfer of "whole" charges (not partial charges as done in our work) to differentiate the various surface oxygen species [39]. In our proposal, Table 1 shows that it is also possible to obtain CT rate expressions and evaluate the likelihood of different surface oxygen species involved in an oxidation reaction. However, our method employs realistic partial net charges transferred in the rate determining step which are determined theoretically. Therefore, our proposed methodology is more robust than assuming oxygen charges of 0, −1, or −2 as previously done by Herrmann [39].

3.3.2. CT-SKAn: DFT calculations

To apply the CT-SKAn methodology described in **Section 2.6.2**, an estimate of the relative charge change in a kinetically relevant step is required. Fig. 10 presents the DFT results for the electronic charge distribution and reaction energies of the different intermediate species on gold and at the Au-support interface. Additional details on the DFT electronic charge distribution results are presented in the Supporting Information (**Tables S5-S12**). These results were used to calculate the net charge transfer (n) for the different surface oxygen species in Table 1. This is done by taking the difference between the net total charge in the products (Fig. 10**e, f, g, and h**) and the reactants (Fig. 10**a, b, c, and d**) side for all the surface species. The amount of charge transferred on Au upon all species adsorption varied between 0.03 and 0.13 electron per surface atom. This range was in excellent agreement with O_2 adsorption on Au/TiO_2 (Au particle size ~ 4 nm) which resulted in estimated charge transfers between 0.05 and 0.13 electron per surface atom [68]. Similar charge transfers of 0.02–0.15 have also been calculated for O_2 adsorbed at the Au-support interface in the absence/presence of a co-adsorbed alcohol on $Au_n/TiO_2(1\,1\,0)$ models. Additionally, the calculated reaction energies for ethoxy oxidation into acetaldehyde are negative (i.e., exothermic reactions) when the hydrocarbon species are on Au and the oxidizing species are at the Au-TiO_2 interface (Fig. 10). The absolute values of the reaction energies decrease (become less thermodynamically favorable) in the following order: O■ > O_2■ > HO■ > HOO■. This order resembles that obtained with previous DFT calculations of reaction enthalpies of ethoxy species on a Au(1 1 1) surface: HO■ > O■ > O_2■ > HOO■ [78]. Although these trends are not a direct indication of kinetic relevance, they demonstrate the coexistence of different surface oxygen species. This conclusion is consistent with the reported metastability of dioxygen adsorption at the metal-support interface [42], leading to the formation of peroxide and superoxide species [33,86,87]. A similar mechanism suggesting the formation of HOO■

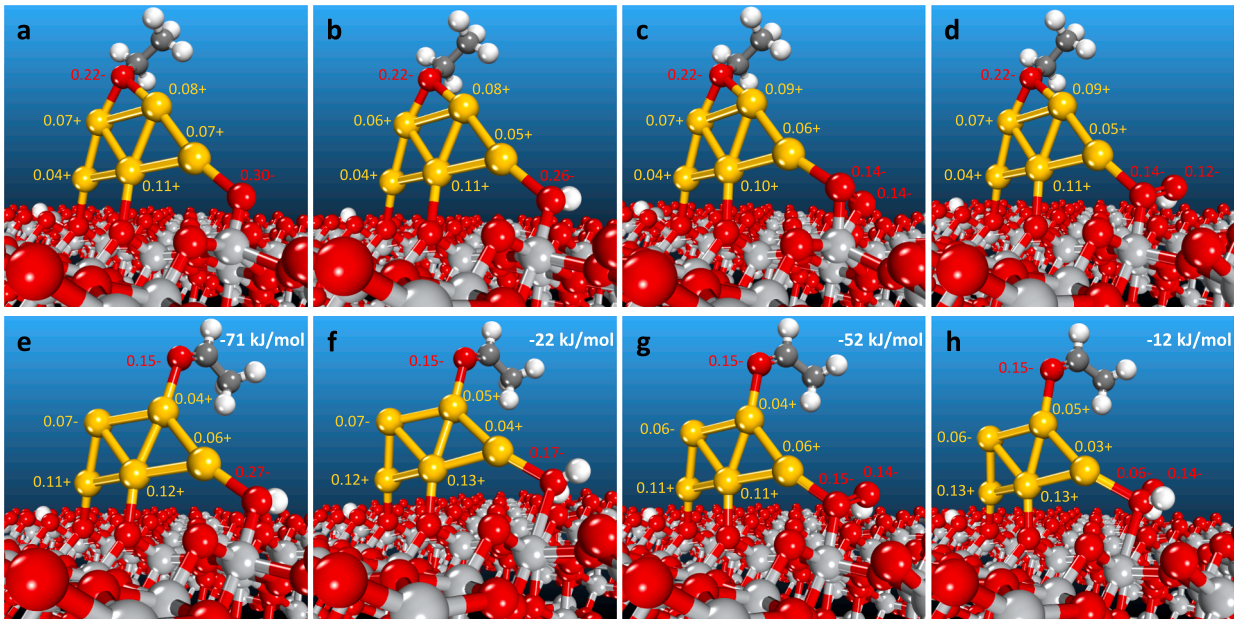

Fig. 10. DFT calculations for ethoxy oxidation into acetaldehyde with various surface oxygen species on Au/TiO_2. The top row shows the reactants (ethoxy on Au with four oxidizing species adsorbed at the Au-TiO_2 interface): (**a**) $CH_3CH_2O^*$ + O ■, (**b**) $CH_3CH_2O^*$ + HO ■, (**c**) $CH_3CH_2O^*$ + O_2 ■, (**d**) $CH_3CH_2O^*$ + HOO ■. The bottom row shows the corresponding products (acetaldehyde on Au with four reduced species adsorbed at the Au-TiO_2 interface): (**e**) CH_3CHO^* + HO ■, (**f**) CH_3CHO^* + H_2O ■, (**g**) CH_3CHO^* + HOO ■, (**h**) CH_3CHO^* + H_2O_2 ■. The numbers next to the acetaldehyde product show the calculated reaction energies (kJ/mol), and the numbers next to the Au and O atoms show the calculated Hirshfeld partial charges.

followed by its readily dissociation into O■ and HO■ at relatively low energy barriers (~0.24 eV) has been proposed for the CO oxidation on gold catalysts [87]. In such mechanisms, the thermodynamic favorability of HOO■ was explained based on the weaker O-O bond in HOO■ compared to that in dioxygen. Thus, HOO■ could react directly with ethanol, or simply participate as a precursor in the formation of other active intermediates (O■ and/or HO■).

3.3.3. *CT-SKAn: UV–Vis and MS data fitting to CT-Kinetic models*

In the previous **Sections 3.3.1 and 3.3.2**, we derived a series of kinetic models (Table 1) that relate: (1) spectroscopic (i.e., absorbance as a descriptor for charge transfer) and (2) reaction rate (i.e., conversion rate, O_2 partial pressure) measurements. The models also contain a pseudo stoichiometric net charge transfer (from DFT) for different surface active oxygen species present in the kinetically relevant step. The obtained rate expressions from the proposed mechanisms are convenient as they show a direct proportionality between charge transfer [e-] and a $(r/P_{O2})^x$ rate term. This relationship facilitates the evaluation of possible reactive oxygen species in the catalytic mechanism by a simple visual inspection of the goodness of fit of the rate model to the experimental data. The survey screening of absorbance from ME-UV–Vis-NIR experiments indicated that the spectral response was more sensitive to a variation in oxygen (**Figures 8, S5, S6, and S7**) than to ethanol (**Figures S9 and S10**) partial pressures. Moreover, the spectral intensity in the d-d region varied inversely proportional with oxygen partial pressure as a result of electron transfer from TiO_2 to adsorbed oxygen via the gold-support interface (Fig. 8). This is also in agreement with previous observations on redox type chemistries (e.g., propane oxidative dehydrogenation on VOx catalysts [88]). Therefore, for the evaluation of surface oxygen species via the kinetic models in Table 1, UV–Vis spectral information and species concentrations (via MS) were collected under operando conditions. More specifically, ethanol oxidation was performed at steady state at different oxygen partial pressures (0.8–1.5 kPa) and constant ethanol concentration (1 kPa). The resulting absorbance response, as shown in **Figures S7 and S11**, decreased at higher O_2 partial pressures. This confirmed the depletion of charge in the vicinity of the gold-support interface as CT events took place to activate surface oxygen intermediates.

To fit the experimental data to the CT kinetic models, first, the absorbance data (corrected for support contributions) in the d-d transition region was taken as an uncalibrated but linearly proportional descriptor for CT. This is a reasonable approximation in the small range of oxygen partial pressures tested, which allows to follow the relative correlations of the CT [e^-] models. Moreover, MS signals for ethanol and oxygen were converted to partial pressures through gas calibrations and used to determine conversion and reaction rate. Details on the experiments and calculations are given in **Sections S4** and **S5** of the Supporting Information. With all this information, Fig. 11 was prepared so the plotted experimental data would lead to linear trends for each of the kinetic models. For example, for each surface oxygen species in Table 1, the *y* and *x* axes corresponded to: [e-] vs $(r/P_{O2})^{1/n}$ for O_2^{n-}, [e-] vs $(r/(nP_{O2}))^{1/(n+1)}$ for HOO and HO, and [e-] vs $(r/P_{O2})^{1/2n}$ for O^{n-} species.

Two main results can be noted for the CT models of the adsorbed oxygen species shown in Fig. 11**:** 1) the poor fit of the spectrokinetic model for O_2^{n-} species (Fig. 11**a**) and 2) the much higher and similar correlation for the HOO, HO, and O^{n-} charge transfer models (Fig. 11**b, 11c, and 11d**). These correlations were further confirmed by the F-statistic test of the different model variances as detailed in **Section S6** and summarized in **Tables S13 and S14** in the Supporting Information. Overall, these results allow to: 1) rule out adsorbed molecular oxygen (O_2^{n-}) as an active surface oxygen species in the rate determining step; and 2) to provide strong combined experimental activity and spectroscopic evidence for HOO, HO, and O^{n-} species as kinetically relevant surface species. The observation that dioxygen is not an active surface species for oxidation of ethoxy species is consistent with adsorbed molecular oxygen's lack of stability at temperatures higher than ambient conditions. This is based on O_2's low calculated adsorption energies [44,69,74,89] and metastability at the gold-support perimeter interface [42].

The kinetic relevance of HOO, HO, and O^{n-} species implied from the CT-SKAn is also in agreement with prior in situ spectroscopic, kinetic, and DFT calculations. For example, HOO species have been shown to be

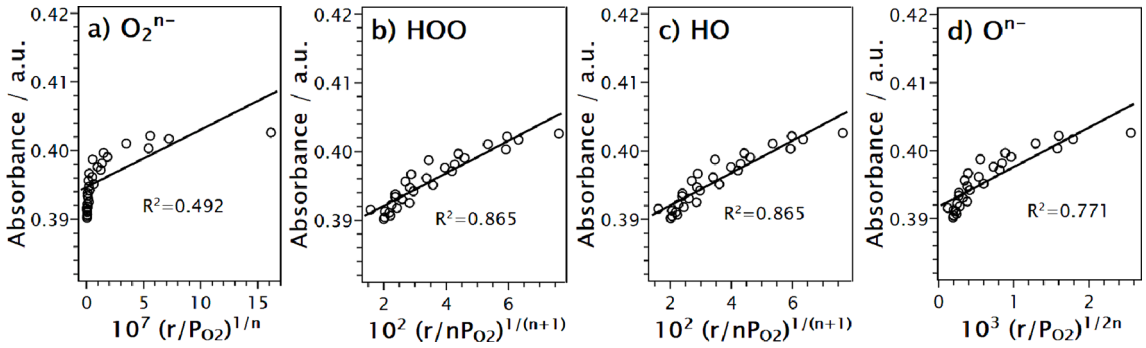

Fig. 11. Correlation results for charge transfer models shown in Table 1 for different surface oxygen species involved in ethanol oxidation on Au/TiO_2: a) O_2^{n-}, b) HOO, c) HO, and d) O^{n-}. The *x* axis corresponds to the $(r/P_{O2})^x$ term in the kinetic model, which varies depending on the oxygen species. The *y* axis corresponds to the Au/TiO_2 absorbance at 900 nm and at reaction conditions corrected for bare TiO_2 support contributions. The parameter *n* is the net charge transferred to the support in the rate limiting step as calculated from DFT (last column in Table 1).

true reaction intermediates during propylene epoxidation with O_2 and H_2 on $Au/Ti\text{-}SiO_2$ [9] based on in situ XANES and reactor activity measurements. HO species have also been proposed to be kinetically relevant surface species in ethanol and CO oxidation on Au/TiO_2 [78] and Au/C [90], respectively. Chandler and co-workers also showed via DFT studies the relative kinetic relevance of HOO, HO, and O species for CO oxidation over Au/TiO_2 [43]. This study highlighted the relative stability of these species (HOO → O + HO) and their energy barriers for CO oxidation (HOO < HO < O), but all with different but experimentally reasonable activation energies (0-10–0.65 eV). Lastly, Murzin and co-workers recently proposed the kinetic relevance of HOO, HO, and O in ethanol oxidation on Au/Al_2O_3 at 150–250 °C based on DFT calculations where ethanol adsorbs dissociatively on Au(1 1 1) and concomitantly with O_2 activation to form HOO species. These latter species can undergo decomposition to HO and O, from which atomic O was presumed to be the primary intermediate species carrying out the β-dehydrogenation of the surface ethoxy species.

Overall, the CT-SKAn methodology confirms the coexistence of different kinetically relevant surface oxygen species: HOO, HO, and O^{n-} for ethanol oxidation on Au/TiO_2. This appears to be a more common occurrence in oxidation reactions than originally realized. For example, in ethylene epoxidation on silver catalysts the presence of several reactive surface oxygen species have been postulated from in situ Raman [91] and DFT calculations [92]. In the present work, based on a combination of DFT studies and kinetic experiments and prior literature, a plausible mechanism for ethanol oxidation on Au/TiO_2 involving HOO, HO, and O^{n-} can be proposed. Here, oxygen activation is assisted by surface hydrogen resulting from ethanol dissociative adsorption. This leads to surface HOO formation which can dissociate into atomic oxygen and HO [93]. All these oxygen species could participate in kinetically relevant steps. However, additional detailed DFT and microkinetic studies, which are beyond the scope of the present spectrokinetic work, would be required to clarify their exact involvement in series and/or competing parallel elementary steps.

4. Conclusions

A general spectrokinetic methodology was developed to assess the nature of kinetically relevant surface oxygen species during ethanol oxidation with molecular oxygen on gold catalysts. The method was named CT-SKAn, charge transfer spectrokinetic analysis. It combines operando UV–Vis measurements with the Langmuir-Hinshelwood kinetic formalism accounting for the net change of surface species charges in a kinetically relevant step. This methodology provided strong evidence for the participation of surface HOO, HO, and O species in ethanol oxidation elementary steps, while allowing to rule out surface O_2 as a reactive intermediate. DFT calculations suggested that oxygen species would preferentially adsorb at the $Au\text{-}TiO_2$ interface rather than on Au. Moreover, DFT calculations were also performed to determine surface species charges during ethoxy oxidation into acetaldehyde with O_2, HOO, HO, and O on Au/TiO_2. In situ Au maximum plasmon peak shifts (Au MAPPS) also evidenced that oxygen species preferentially adsorb at the Au-support interface. Additionally, modulation excitation-phase sensitive detection-UV–Vis spectroscopy (ME-PSD-UV–Vis) provided information about the charge transfer dynamic behavior between surface oxygen species and Au/TiO_2. The charge transfer spectrokinetic results were consistent with a mechanism where oxygen is activated at the Au-support interface as HOO, HO, and O. These reactive surface oxygen species participate in kinetically relevant steps to β-dehydrogenate surface ethoxy to form acetaldehyde in a rate limiting step. The developed CT-SKAn methodology, which combines an analysis of charge transfer via operando UV–Vis spectroscopy with Langmuir-Hinshelwood kinetic models and DFT calculations, is not limited to ethanol oxidation over Au/TiO_2. It should be of general application for determining the nature of reactive surface species in heterogeneously catalyzed reactions.

CRediT authorship contribution statement

Alejandra Torres-Velasco: Writing – review & editing, Writing – original draft, Methodology, Investigation, Formal analysis, Conceptualization. **Bhagyesha S. Patil:** Investigation, Formal analysis. **Hongda Zhu:** Visualization, Software, Formal analysis. **Yue Qi:** Visualization, Investigation, Formal analysis. **Simon G. Podkolzin:** Writing – review & editing, Supervision, Methodology, Investigation, Formal analysis. **Juan J. Bravo-Suárez:** Writing – review & editing, Supervision, Resources, Project administration, Methodology, Funding acquisition, Conceptualization.

Declaration of competing interest

The authors declare that they have no known competing financial interests or personal relationships that could have appeared to influence the work reported in this paper.

Data availability

Data will be made available on request.

Acknowledgments

A.T.-V., B.P., and J.J.B.-S. acknowledge the financial support by the National Science Foundation under grant No CBET-1847655. S.G.P. acknowledge a collaborative research Science Ambassador license with Dassault Systèmes BIOVIA Corporation for performing DFT calculations with the Materials Studio software.

Appendix A. Supplementary material

Supplementary data to this article can be found online at https://doi.org/10.1016/j.jcat.2024.115508.

References

[1] T. Gott, S.T. Oyama, A general method for determining the role of spectroscopically observed species in reaction mechanisms: Analysis of coverage transients (ACT), J. Catal. 263 (2009) 359–371.
[2] F.C. Meunier, The power of quantitative kinetic studies of adsorbate reactivity by operando FTIR spectroscopy carried out at chemical potential steady-state, Catal. Today 155 (2010) 164–171.
[3] C.M. Kalamaras, S. Americanou, A.M. Efstathiou, "Redox" vs "associative formate with –OH group regeneration" WGS reaction mechanism on Pt/CeO2: Effect of platinum particle size, J. Catal. 279 (2011) 287–300.
[4] V.A. Matyshak, O.V. Krylov, In-situ IR spectroscopy of intermediates in heterogeneous oxidative catalysis, Catal. Today 25 (1995) 1–87.
[5] M.D. Argyle, K. Chen, C. Resini, C. Krebs, A.T. Bell, E. Iglesia, In situ UV-visible assessment of extent of reduction during oxidation reactions on oxide catalysts, Chem. Commun. (2003) 2082–2083.
[6] M.D. Argyle, K.D. Chen, C. Resini, C. Krebs, A.T. Bell, E. Iglesia, Extent of reduction of vanadium oxides during catalytic oxidation of alkanes measured by in-situ UV-visible spectroscopy, J. Phys. Chem. B 108 (2004) 2345–2353.
[7] A. Bensalem, B.M. Weckhuysen, R.A. Schoonheydt, In situ diffuse reflectance spectroscopy of supported chromium oxide catalysts: Kinetics of the reduction process with carbon monoxide, J. Phys. Chem. B 101 (1997) 2824–2829.
[8] O. Ovsitser, M. Cherian, A. Brückner, E.V. Kondratenko, Dynamics of redox behavior of nano-sized vox species over Ti–Si-MCM-41 from time-resolved in situ UV/Vis analysis, J. Catal. 265 (2009) 8–18.
[9] J.J. Bravo-Suarez, K.K. Bando, J.I. Lu, M. Haruta, T. Fujitani, S.T. Oyama, Transient technique for identification of true reaction intermediates: Hydroperoxide species in propylene epoxidation on gold/titanosilicate catalysts by X-ray absorption fine structure spectroscopy, J. Phys. Chem. C 112 (2008) 1115–1123.
[10] E.E. Ortelli, A. Wokaun, Use of periodic variations of reactant concentrations in time resolved FTIR studies of heterogeneously catalysed reactions, Vib. Spectrosc. 19 (1999) 451–459.
[11] R. Kopelent, J.A. van Bokhoven, J. Szlachetko, J. Edebeli, C. Paun, M. Nachtegaal, O.V. Safonova, Catalytically active and spectator Ce^{3+} in ceria-supported metal catalysts, Angew. Chem., Int. Ed. 54 (2015) 8728–8731.
[12] P.D. Srinivasan, K. Khivantsev, J.M.M. Tengco, H. Zhu, J.J. Bravo-Suárez, Enhanced ethanol dehydration on γ-Al_2O_3 supported cobalt catalyst, J. Catal. 373 (2019) 276–296.
[13] P.D. Srinivasan, B.S. Patil, H. Zhu, J.J. Bravo-Suárez, Application of modulation excitation-phase sensitive detection-DRIFTS for in situ/operando characterization of heterogeneous catalysts, React. Chem. Eng. 4 (2019) 862–883.
[14] P.D. Srinivasan, H. Zhu, J.J. Bravo-Suárez, In situ UV–vis plasmon resonance spectroscopic assessment of oxygen and hydrogen adsorption location on supported gold catalysts, Mol. Catal. 507 (2021) 111572.
[15] E.D. Hernandez, F.C. Jentoft, Spectroscopic signatures reveal cyclopentenyl cation contributions in methanol-to-olefins catalysis, ACS Catal. 10 (2020) 5764–5782.
[16] T. Takei, N. Iguchi, M. Haruta, Synthesis of acetoaldehyde, acetic acid, and others by the dehydrogenation and oxidation of ethanol, Catal. Surv Asia 15 (2011) 80–88.
[17] T. Takei, N. Iguchi, M. Haruta, Support effect in the gas phase oxidation of ethanol over nanoparticulate gold catalysts, New J. Chem. 35 (2011).
[18] P. Liu, E.J. Hensen, Highly efficient and robust Au/$MgCuCr_2O_4$ catalyst for gas-phase oxidation of ethanol to acetaldehyde, J. Am. Chem. Soc. 135 (2013) 14032–14035.
[19] C.H. Christensen, B. Jørgensen, J. Rass-Hansen, K. Egeblad, R. Madsen, S. K. Klitgaard, S.M. Hansen, M.R. Hansen, H.C. Andersen, A. Riisager, Formation of acetic acid by aqueous-phase oxidation of ethanol with air in the presence of a heterogeneous gold catalyst, Angew. Chem., Int. Ed. 45 (2006) 4648–4651.
[20] B. Jørgensen, S. Egholm Christiansen, M.L. Dahl Thomsen, C.H. Christensen, Aerobic oxidation of aqueous ethanol using heterogeneous gold catalysts: Efficient routes to acetic acid and ethyl acetate, J. Catal. 251 (2007) 332–337.
[21] S.M. Tembe, G. Patrick, M.S. Scurrell, Acetic acid production by selective oxidation of ethanol using Au catalysts supported on various metal oxide, Gold Bull. 42 (2009) 321–327.
[22] K.-Q. Sun, S.-W. Luo, N. Xu, B.-Q. Xu, Gold nano-size effect in Au/SiO_2 for selective ethanol oxidation in aqueous solution, Catal. Lett. 124 (2008) 238–242.
[23] L.V. Mattos, F.B. Noronha, Partial oxidation of ethanol on supported Pt catalysts, J. Power Sources 145 (2005) 10–15.
[24] B. Jørgensen, S.B. Kristensen, A.J. Kunov-Kruse, R. Fehrmann, C.H. Christensen, A. Riisager, Gas-phase oxidation of aqueous ethanol by nanoparticle vanadia/anatase catalysts, Top. Catal. 52 (2009) 253–257.
[25] V.I. Sobolev, K.Y. Koltunov, Movnbte mixed oxides as efficient catalyst for selective oxidation of ethanol to acetic acid, ChemCatChem 3 (2011) 1143–1145.
[26] T. Ishida, R. Takamura, T. Takei, T. Akita, M. Haruta, Support effects of metal oxides on gold-catalyzed one-pot n-alkylation of amine with alcohol, Appl. Catal., A (2012), 413–414, pp. 261–266.
[27] Y.T. Zheng, Y. Qi, Z.Y. Tang, J.Z. Tan, B.E. Koel, S.G. Podkolzin, Spectroscopic observation and structure-insensitivity of hydroxyls on gold, Chem. Commun. 58 (2022) 4036–4039.
[28] A. Waheed, X.W. Wang, N. Maeda, D.M. Meier, T. Ishida, T. Murayama, M. Haruta, A. Baiker, Influence of the support in aqueous phase oxidation of ethanol on gold/metal oxide catalysts studied by ATR-IR spectroscopy under working conditions, Catal. Commun. 148 (2021).
[29] J. Cornejo-Romero, A. Solis-Garcia, S.M. Vega-Diaz, J.C. Fierro-Gonzalez, Reverse hydrogen spillover during ethanol dehydrogenation on TiO_2-supported gold catalysts, Mol. Catal. 433 (2017) 391–402.
[30] T.H. Tan, J. Scott, Y.H. Ng, R.A. Taylor, K.-F. Aguey-Zinsou, R. Amal, C-C cleavage by Au/TiO_2 during ethanol oxidation: Understanding bandgap photoexcitation and plasmonically mediated charge transfer via quantitative in situ DRIFTS, ACS Catal. 6 (2016) 8021–8029.
[31] E.O. Gonzalez-Yañez, G.A. Fuentes, M.E. Hernández-Terán, J.C. Fierro-Gonzalez, Influence of supported gold particles on the surface reactions of ethanol on TiO_2, Appl. Catal., A (2013), 464–465, pp. 374–383.
[32] C.-R. Chang, X.-F. Yang, B. Long, J. Li, A water-promoted mechanism of alcohol oxidation on a Au(111) surface: Understanding the catalytic behavior of bulk gold, ACS Catal. 3 (2013) 1693–1699.
[33] M. Farnesi Camellone, D. Marx, Nature and role of activated molecular oxygen species at the gold/titania interface in the selective oxidation of alcohols, J. Phys. Chem. C 118 (2014) 20989–21000.
[34] N.M. Wilson, D.W. Flaherty, Mechanism for the direct synthesis of H_2O_2 on pd clusters: Heterolytic reaction pathways at the liquid–solid interface, J. Am. Chem. Soc. 138 (2016) 574–586.
[35] P.D. Srinivasan, S.R. Nitz, K.J. Stephens, E. Atchison, J.J. Bravo-Suárez, Modified Harrick reaction cell for in situ/operando fiber optics diffuse reflectance UV–visible spectroscopic characterization of catalysts, Appl. Catal., A 561 (2018) 7–18.
[36] B.S. Patil, P.D. Srinivasan, E. Atchison, H. Zhu, J.J. Bravo-Suárez, Design, modelling, and application of a low void-volume in situ diffuse reflectance spectroscopic reaction cell for transient catalytic studies, React. Chem. Eng. 4 (2019) 667–678.
[37] G. Djéga-Mariadassou, M. Boudart, Classical kinetics of catalytic reactions, J. Catal. 216 (2003) 89–97.
[38] M.D. Argyle, K. Chen, C. Resini, C. Krebs, A.T. Bell, E. Iglesia, Extent of reduction of vanadium oxides during catalytic oxidation of alkanes measured by in-situ UV−Visible spectroscopy, J. Phys. Chem. B 108 (2004) 2345–2353.
[39] J.M. Herrmann, The electronic factor and related redox processes in oxidation catalysis, Catal. Today 112 (2006) 73–77.
[40] D.A. Panayotov, S.P. Burrows, J.T. Yates, J.R. Morris, Mechanistic studies of hydrogen dissociation and spillover on Au/TiO_2: IR spectroscopy of coadsorbed CO and h-donated electrons, J. Phys. Chem. C 115 (2011) 22400–22408.
[41] D.A. Panayotov, J.T. Yates, Spectroscopic detection of hydrogen atom spillover from Au nanoparticles supported on TiO_2: Use of conduction band electrons, J. Phys. Chem. C 111 (2007) 2959–2964.
[42] H. Koga, K. Tada, M. Okumura, Density functional theory study of active oxygen at the perimeter of Au/TiO_2 catalysts, J. Phys. Chem. C 119 (2015) 25907–25916.
[43] J. Saavedra, H.A. Doan, C.J. Pursell, L.C. Grabow, B.D. Chandler, The critical role of water at the gold-titania interface in catalytic CO oxidation, Science 345 (2014) 1599–1602.
[44] I.X. Green, W. Tang, M. Neurock, J.T. Yates, Spectroscopic observation of dual catalytic sites during oxidation of CO on a Au/TiO_2 catalyst, Science 333 (2011) 736–739.
[45] Y. Gao, X.C. Zeng, Water-promoted O_2 dissociation on small-sized anionic gold clusters, ACS Catal. 2 (2012) 2614–2621.
[46] W. Wan, X. Nie, M.J. Janik, C. Song, X. Guo, Adsorption, dissociation, and spillover of hydrogen over Au/TiO_2 catalysts: The effects of cluster size and metal–support interaction from DFT, J. Phys. Chem. C 122 (2018) 17895–17916.
[47] A.R. Puigdollers, P. Schlexer, G. Pacchioni, Gold and silver clusters on TiO_2 and ZrO_2 (101) surfaces: Role of dispersion forces, J. Phys. Chem. C 119 (2015) 15381–15389.
[48] K. Liu, T. Chen, S. He, J.P. Robbins, S.G. Podkolzin, F. Tian, Observation and identification of an atomic oxygen structure on catalytic gold nanoparticles, Angew. Chem., Int. Ed. 56 (2017) 12952–12957.
[49] D.G. Barton, S.G. Podkolzin, Kinetic study of a direct water synthesis over silica-supported gold nanoparticles, J. Phys. Chem. B 109 (2005) 2262–2274.
[50] Y. Zheng, Y. Qi, Z. Tang, F. Hanke, S.G. Podkolzin, Kinetics and reaction mechanisms of acetic acid hydrodeoxygenation over Pt and Pt–Mo catalysts, ACS Sustain. Chem. Eng. 10 (2022) 5212–5224.
[51] Y. Zheng, Z. Tang, S.G. Podkolzin, Catalytic platinum nanoparticles decorated with subnanometer molybdenum clusters for biomass processing, Chemistry 26 (2020) 5174–5179.
[52] M.S. Hofman, E.V. Scoullos, J.P. Robbins, L. Ezeonu, D.V. Potapenko, X. Yang, S. G. Podkolzin, B.E. Koel, Acetic acid adsorption and reactions on Ni(110), Langmuir 36 (2020) 8705–8715.
[53] E.V. Scoullos, M.S. Hofman, Y. Zheng, D.V. Potapenko, Z. Tang, S.G. Podkolzin, B. E. Koel, Guaiacol adsorption and decomposition on platinum, J. Phys. Chem. C 122 (2018) 29180–29189.
[54] T. Chen, E. Kertalli, T.A. Nijhuis, S.G. Podkolzin, Effects of hydrogen and propylene presence on decomposition of hydrogen peroxide over palladium catalysts, J. Catal. 341 (2016) 72–81.
[55] T. Chen, A. Pal, J. Gao, Y. Han, H. Chen, S. Sukhishvili, H. Du, S.G. Podkolzin, Identification of vertical and horizontal configurations for BPE adsorption on silver surfaces, J. Phys. Chem. C 119 (2015) 24475–24488.
[56] J. Gao, H. Zhao, X. Yang, B.E. Koel, S.G. Podkolzin, Controlling acetylene adsorption and reactions on Pt–Sn catalytic surfaces, ACS Catal. 3 (2013) 1149–1153.

[57] J. Gao, H. Zhao, X. Yang, B.E. Koel, S.G. Podkolzin, Geometric requirements for hydrocarbon catalytic sites on platinum surfaces, Angew. Chem., Int. Ed. 53 (2014) 3641–3644.

[58] L. Ezeonu, Z. Tang, Y. Qi, F. Huo, Y. Zheng, B.E. Koel, S.G. Podkolzin, Adsorption, surface reactions and hydrodeoxygenation of acetic acid on platinum and nickel catalysts, J. Catal. 418 (2023) 190–202.

[59] J. Gao, Y. Zheng, G.B. Fitzgerald, J. de Joannis, Y. Tang, I.E. Wachs, S. G. Podkolzin, Structure of Mo_2C_x and Mo_4C_x molybdenum carbide nanoparticles and their anchoring sites on ZSM-5 zeolites, J. Phys. Chem. C 118 (2014) 4670–4679.

[60] J. Gao, Y. Zheng, Y. Tang, J.-M. Jehng, R. Grybos, J. Handzlik, I.E. Wachs, S. G. Podkolzin, Spectroscopic and computational study of Cr oxide structures and their anchoring sites on ZSM-5 zeolites, ACS Catal. 5 (2015) 3078–3092.

[61] Y. Zheng, Y. Tang, J.R. Gallagher, J. Gao, J.T. Miller, I.E. Wachs, S.G. Podkolzin, Molybdenum oxide, oxycarbide, and carbide: Controlling the dynamic composition, size, and catalytic activity of zeolite-supported nanostructures, J. Phys. Chem. C 123 (2019) 22281–22292.

[62] J. Gao, Y.T. Zheng, J.M. Jehng, Y.D. Tang, I.E. Wachs, S.G. Podkolzin, Identification of molybdenum oxide nanostructures on zeolites for natural gas conversion, Science 348 (2015) 686–690.

[63] Z. Tang, T. Chen, K. Liu, H. Du, S.G. Podkolzin, Atomic, molecular and hybrid oxygen structures on silver, Langmuir 37 (2021) 11603–11610.

[64] J.J. Bravo-Suárez, K.K. Bando, T. Fujitani, S.T. Oyama, Mechanistic study of propane selective oxidation with H_2 and O_2 on Au/TS-1, J. Catal. 257 (2008) 32–42.

[65] J.J. Bravo-Suárez, K.K. Bando, J.Q. Lu, T. Fujitani, S.T. Oyama, Oxidation of propane to propylene oxide on gold catalysts, J. Catal. 255 (2008) 114–126.

[66] L. Barrio, P. Liu, J.A. Rodriguez, J.M. Campos-Martin, J.L.G. Fierro, Effects of hydrogen on the reactivity of O_2 toward gold nanoparticles and surfaces, J. Phys. Chem. C 111 (2007) 19001–19008.

[67] M. Shekhar, J. Wang, W.-S. Lee, W.D. Williams, S.M. Kim, E.A. Stach, J.T. Miller, W.N. Delgass, F.H. Ribeiro, Size and support effects for the water–gas shift catalysis over gold nanoparticles supported on model Al_2O_3 and TiO_2, J. Am. Chem. Soc. 134 (2012) 4700–4708.

[68] Y. Borensztein, L. Delannoy, A. Djedidi, R.G. Barrera, C. Louis, Monitoring of the plasmon resonance of gold nanoparticles in Au/TiO_2 catalyst under oxidative and reducing atmospheres, J. Phys. Chem. C 114 (2010) 9008–9021.

[69] J. Gong, C.B. Mullins, Surface science investigations of oxidative chemistry on gold, Acc. Chem. Res. 42 (2009) 1063–1073.

[70] M. Boronat, A. Corma, F. Illas, J. Radilla, T. Ródenas, M.J. Sabater, Mechanism of selective alcohol oxidation to aldehydes on gold catalysts: Influence of surface roughness on reactivity, J. Catal. 278 (2011) 50–58.

[71] Q. Meng, Y. Shen, J. Xu, J. Gong, Mechanistic insights into selective oxidation of ethanol on Au(111): A DFT study, Chin. J. Catal. 33 (2012) 407–415.

[72] S.D. Senanayake, K. Mudiyanselage, A. Bruix, S. Agnoli, J. Hrbek, D. Stacchiola, J. A. Rodriguez, The unique properties of the oxide-metal interface: Reaction of ethanol on an inverse model CeO_x–Au(111) catalyst, J. Phys. Chem. C 118 (2014) 25057–25064.

[73] D.T. Boyle, J.A. Wilke, R.M. Palomino, V.H. Lam, D.A. Schlosser, W.J. Andahazy, C.Z. Stopak, D.J. Stacchiola, J.A. Rodriguez, A.E. Baber, Elucidation of active sites for the reaction of ethanol on TiO_2/Au(111), J. Phys. Chem. C 121 (2017) 7794–7802.

[74] Z.P. Liu, X.Q. Gong, J. Kohanoff, C. Sanchez, P. Hu, Catalytic role of metal oxides in gold-based catalysts: A first principles study of CO oxidation on TiO_2 supported Au, Phys. Rev. Lett. 91 (2003) 266102.

[75] D. Widmann, R.J. Behm, Activation of molecular oxygen and the nature of the active oxygen species for CO oxidation on oxide supported Au catalysts, Acc. Chem. Res. 47 (2014) 740–749.

[76] D. Widmann, R.J. Behm, Active oxygen on a Au/TiO_2 catalyst: Formation, stability, and CO oxidation activity, Angew. Chem., Int. Ed. 50 (2011) 10241–10245.

[77] M.S. Ide, R.J. Davis, The important role of hydroxyl on oxidation catalysis by gold nanoparticles, Acc. Chem. Res. 47 (2014) 825–833.

[78] B.N. Zope, D.D. Hibbitts, M. Neurock, R.J. Davis, Reactivity of the gold/water interface during selective oxidation catalysis, Science 330 (2010) 74–78.

[79] T. Takei, T. Akita, I. Nakamura, T. Fujitani, M. Okumura, K. Okazaki, J. Huang, T. Ishida, M. Haruta, Heterogeneous catalysis by gold, Adv. Catal. 55 (2012) 1–126.

[80] M. Haruta, Size- and support-dependency in the catalysis of gold, Catal. Today 36 (1997) 153–166.

[81] S. Laursen, S. Linic, Geometric and electronic characteristics of active sites on TiO_2-supported Au nano-catalysts: Insights from first principles, Phys. Chem. Chem. Phys. 11 (2009) 11006–11012.

[82] J. Saavedra, C.J. Pursell, B.D. Chandler, CO oxidation kinetics over Au/TiO_2 and Au/Al_2O_3 catalysts: Evidence for a common water-assisted mechanism, J. Am. Chem. Soc. 140 (2018) 3712–3723.

[83] X. Li, E. Iglesia, Selective catalytic oxidation of ethanol to acetic acid on dispersed Mo-V-Nb mixed oxides, Chemistry 13 (2007) 9324–9330.

[84] W. Song, P. Liu, E.J.M. Hensen, A mechanism of gas-phase alcohol oxidation at the interface of Au nanoparticles and a $MgCuCr_2O_4$ spinel support, Catal, Sci. Technol. 4 (2014) 2997–3003.

[85] B. Xu, J. Haubrich, T.A. Baker, E. Kaxiras, C.M. Friend, Theoretical study of O-assisted selective coupling of methanol on Au(111), J. Phys. Chem. C 115 (2011) 3703–3708.

[86] N. Siemer, A. Lüken, M. Zalibera, J. Frenzel, D. Muñoz-Santiburcio, A. Savitsky, W. Lubitz, M. Muhler, D. Marx, J. Strunk, Atomic-scale explanation of O_2 activation at the Au–TiO_2 interface, J. Am. Chem. Soc. 140 (2018) 18082–18092.

[87] C.-R. Chang, Z.-Q. Huang, J. Li, Hydrogenation of molecular oxygen to hydroperoxyl: An alternative pathway for O_2 activation on nanogold catalysts, Nano Res. 8 (2015) 3737–3748.

[88] M.D. Argyle, K. Chen, A.T. Bell, E. Iglesia, Effect of catalyst structure on oxidative dehydrogenation of ethane and propane on alumina-supported vanadia, J. Catal. 208 (2002) 139–149.

[89] I.N. Remediakis, N. Lopez, J.K. Norskov, CO oxidation on rutile-supported Au nanoparticles, Angew. Chem., Int. Ed. 44 (2005) 1824–1826.

[90] A. Wieckowski, M. Neurock, Contrast and synergy between electrocatalysis and heterogeneous catalysis, Adv. Phys. Chem. 2011 (2011) 907129.

[91] H.A. Alzahrani, J.J. Bravo-Suárez, In situ Raman spectroscopy study of silver particle size effects on unpromoted Ag/α-Al_2O_3 during ethylene epoxidation with molecular oxygen, J. Catal. 418 (2023) 225–236.

[92] J.X. Liu, S.W. Lu, S.B. Ann, S. Linic, Mechanisms of ethylene epoxidation over silver from machine learning-accelerated first-principles modeling and microkinetic simulations, ACS Catal. 13 (2023) 8955–8962.

[93] E. Behravesh, M.M. Melander, J. Wärnå, T. Salmi, K. Honkala, D.Y. Murzin, Oxidative dehydrogenation of ethanol on gold: Combination of kinetic experiments and computation approach to unravel the reaction mechanism, J. Catal. 394 (2021) 193–205.

Supporting Information for:

A General Method for Studying Reactive Surface Species, CT-SKAn: Charge-Transfer Spectrokinetic Analysis

Alejandra Torres-Velasco,[1,2] Bhagyesha Patil, [1,2] Hongda Zhu,[1] Yue Qi,[3] Simon G. Podkolzin,[3] Juan J. Bravo-Suárez[*1,2]

1. Center for Environmentally Beneficial Catalysis, The University of Kansas, Lawrence, KS, 66047, USA.
2. Chemical & Petroleum Engineering Department, The University of Kansas, Lawrence, KS, 66045, USA.
3. Department of Chemical Engineering and Materials Science, Stevens Institute of Technology, Hoboken, NJ, 07030, USA.

* E-mail: jjbravo@ku.edu

S1. Catalyst Preparation.

In addition to the commercial Au/TiO_2 and Au/ZnO samples, two additional gold catalysts were prepared with a nominal metal loading of ~1 wt.%. The surface area of the metal oxide supports used was ~10-70m^2/g. $Au/SrTiO_3$ and Au/SiO_2 were prepared by the deposition-precipitation (DP) method using NaOH and ammonia as titrants, respectively. Au/SiO_2 was prepared by adding 3 g of support to 60 cm^3 of water under constant stirring (150 rpm, MS-H-Pro Plus hotplate-stirrer, Scilogex). 2.5 wt% of NH_4OH was added dropwise until reaching a pH of 9.5. Afterwards, 24.2 cm^3 of 0.0063M of $HAuCl_4.3H_2O$ was added dropwise simultaneously with the titrant while maintaining the pH of the slurry at ~10. The solution was then stirred continuously for 1 h (350 rpm) followed by filtration in a funnel/vacuum flask system using filter paper (Whatman, 8 μm, WHA1540150), washing with abundant water and drying in vacuum for 12 h at room temperature in an oven (Thermo Scientific, 3608-1CE). $Au/SrTiO_3$ was prepared by first adding dropwise 1 N NaOH to 150 cm^3 of 1.026 mM of $HAuCl_4.3H_2O$ until pH ~6. The support (3 g) was then added under stirring (450 rpm), and the pH increased to ~9.3. The slurry was stirred (500 rpm) and heated at 70 ˚C for 1 h. The solution was cooled down at room temperature for 30 min, after which it was filtered, washed, and dried as described above. Both catalysts were calcined under static air at 400 ˚C for 4 h (temperature ramp of 4 ˚C/min) in a muffle furnace (Thermolyne 48000, Barnstead International). Similarly, commercial Au/TiO_2 and Au/ZnO (Au loading ~1 wt.%) were also calcined at 400 ˚C (temperature ramp of 4 ˚C/min) for 4 h. After loading samples in the reaction cell, all the catalysts were pretreated in 10% O_2/Ar at 400 ˚C (temperature ramp of 10 ˚C/min) for 1 h.

S2. Internal Mass Transfer Limitation Analysis for the Reaction: When Internal Diffusion is Slow [1]

Considering the irreversible reaction:

$$A \rightarrow \mathrm{B}$$

For an nth-order reaction we know that:

$$r = \eta k C_{As}^{n}$$

By applying definition of the Thiele modulus for an *n*th-order reaction,

$$\Phi = \sqrt{\frac{n+1}{2}\frac{k C_{As}^{n-1} a^2}{D_A}}$$

When internal diffusion is slow,

$$\eta = \frac{1}{\Phi}$$

Then,

$$r_1 = k_{ob} C_{As}^{(n+1)/2}$$

$$k_{ob} = \frac{1}{a}\sqrt{\frac{2}{n+1} D_A \sqrt{k}}$$

$$n_{ob} = \frac{(n+1)}{2}$$

Thus, for an intrinsic reaction rate order of n=1:

$$n_{ob} = 1 = n$$

Now, considering the reaction:

$$A + B \rightarrow \text{Products}$$

Where,

$$r_1 = \eta k C_{As}^{n} C_{Bs}^{m}$$

Then one can similarly show that,

$$r = k'_{ob} C_{As}^{(n+1)/2} C_{Bs}^{(m+1)/2}$$

And for an intrinsic reaction rate order of n=1 and m=1,

$$r = k'_{ob} C_{As} C_{Bs}$$

Then,

$$n_{ob} = 1 = n \text{ and } m_{ob} = 1 = m$$

Thus, since elementary steps in most mechanisms are first order with respect to the reacting species, as in our case, the kinetic results in **Table 1** are valid even in the presence of internal mass transfer limitations. This is the case because the observed reaction rate orders are the same as the intrinsic reaction rate orders.

S3. CT-Kinetic Model Derivations for the Intermediate Oxygen Species Considered in the Proposed Mechanism Towards Acetaldehyde.

A. $O^{n-}\blacksquare$

a. Set of elementary steps for acetaldehyde formation

$$CH_3CH_2OH + * + \blacksquare \rightleftharpoons CH_3CH_2O* + H\blacksquare \quad (1)$$

$$O_2 + \blacksquare \rightleftharpoons O_2\blacksquare \quad (2)$$

$$H\blacksquare \rightleftharpoons H^{n+}\blacksquare + ne^- \quad (3a)$$

$$O_2\blacksquare + 2ne^- + \blacksquare \rightarrow 2O^{n-}\blacksquare \quad (3b)$$

$$CH_3CH_2O* + O^{n-}\blacksquare \nrightarrow CH_3CHO* + HO\blacksquare + ne^- \quad (4)$$

$$H^{n+}\blacksquare + O^{n-}\blacksquare \rightleftharpoons HO\blacksquare + \blacksquare \quad (5)$$

$$H\blacksquare + HO\blacksquare \rightleftharpoons H_2O\blacksquare + \blacksquare \quad (6)$$

$$CH_3CHO* \rightleftharpoons CH_3CHO + * \quad (7)$$

$$H_2O\blacksquare \rightleftharpoons H_2O + \blacksquare \quad (8)$$

b. Reaction rate expression for a fast and irreversible oxygen activation ($r_{+3b} \gg r_{-3b}$)

$r_{3b} = k_{3b}[O_2\blacksquare][\mathrm{e}^-]^{2n}[\blacksquare]$

c. Equilibrium condition to find a concentration dependence for the adsorbed species and expanding into r_3:

$r_2 = k_{+2}[O_2][\blacksquare] - k_{-2}[O_2\ \blacksquare]$, since $r_2/k_{+2} \approx 0$
$[O_2\ \blacksquare] = K_2[O_2][\blacksquare]$

Then,

$r_{3b} = k_{3b}[O_2\blacksquare][\mathrm{e}^-]^{2n}[\blacksquare]$
$r_{3b} = k_{3b}K_2[O_2][\blacksquare]^2[\mathrm{e}^-]^{2n}$
$[O_2] = \dfrac{P_{O_2}}{RT}$

$r_{3b} = k'_{3b}P_{O_2}[\mathrm{e}^-]^{2n}$

Where:
$k'_{3b} = \dfrac{k_{3b}K_2[\blacksquare]^2}{RT}$

d. Reaction rate expression for the RDS:

$$r_4 = k_4[O^{n-}\blacksquare][CH_3CH_2O\ *] = r \quad (RDS)$$

e. QSSA for $O^{n-}\blacksquare$:

$$\frac{d[O^{n-}\blacksquare]}{dt} = 2r_{3b} - r_4$$

$\dfrac{d[O^{n-}\blacksquare]}{dt} = 2k'_3P_{O_2}[\mathrm{e}^-]^{2n} - k_4[\mathrm{O}^{n-}\blacksquare][CH_3CH_2O\ *] \cong 0$
$2k'_{3b}P_{O_2}[\mathrm{e}^-]^{2n} = k_4[\mathrm{O}^{n-}\blacksquare][CH_3CH_2O\ *]$
$[\mathrm{e}^-]^{2n} = \dfrac{k_4[\mathrm{O}^{n-}\blacksquare][CH_3CH_2O\ *]}{2k'_{3b}P_{O_2}}$

Since $r_4 = r\ (RDS)$

$[\mathrm{e}^-]^{2n} = \dfrac{r}{2k'_{3b}P_{O_2}}$
Thus,

$$[e^-] = \sqrt{\left(\frac{r}{2k'_{3b}P_{O_2}}\right)^{\frac{1}{n}}}$$

B. $HO■$

a. Set of elementary steps for acetaldehyde formation

$$CH_3CH_2OH + * + ■ \rightleftharpoons CH_3CH_2O* + H■ \quad (1)$$

$$O_2 + ■ \rightleftharpoons O_2■ \quad (2)$$

$$H■ \rightleftharpoons H^{n+}■ + ne^- \quad (3a)$$

$$O_2■ + H^{n+}■ + ne^- \rightleftharpoons HOO■ + ■ \quad (3b)$$

$$HOO■ + ■ \rightarrow O■ + HO■ \quad (3c)$$

$$CH_3CH_2O* + HO■ \rightleftarrows CH_3CHO* + H_2O■ \quad (4)$$

$$H^{n+}■ + O^{n-}■ \rightleftharpoons HO■ + ■ \quad (5)$$

$$H■ + HO■ \rightleftharpoons H_2O■ + ■ \quad (6)$$

$$CH_3CHO* \rightleftharpoons CH_3CHO + * \quad (7)$$

$$H_2O■ \rightleftharpoons H_2O + ■ \quad (8)$$

b. Reaction rate expression for a fast and irreversible oxygen activation ($r_{+3c} \gg r_{-3c}$)

$$r_{3c} = k_{3c}[HOO■][■]$$

c. Equilibrium condition to find a concentration dependence for the adsorbed species:

Step in equilibrium:
$r_2 = k_{+2}[O_2][■] - k_{-2}[O_2■]$; since $r_2/k_{+2} \approx 0$
$[O_2■] = K_2[O_2][■]$

Then for a quasi-equilibrated step 3b,

$$r_{3b} = k_{+3b}[O_2■][e^-]^n[H^{n+}■] - k_{-3b}[HOO■][■]$$

Assuming that the concentration of protons $[H^{n+}\blacksquare]$ is equal to the concentration of $n[\mathrm{e}^-]$ transferred from the principle of electroneutrality.

Then,

$$[HOO\blacksquare\,] = \frac{K_{3b}[O_2\blacksquare]n[\mathrm{e}^-]^{n+1}}{[\blacksquare]}$$

For an irreversible step 3c:

$$r_{3c} = k_{3c}[HOO\blacksquare][\blacksquare]$$
$$r_{3c} = \frac{k_{3c}K_{3b}[O_2\blacksquare]n[\mathrm{e}^-]^{n+1}[\blacksquare]}{[\blacksquare]}$$
$$r_{3c} = k_{3c}K_{3b}K_2[O_2][\blacksquare]n[\mathrm{e}^-]^{n+1}$$

$$[O_2] = \frac{P_{O_2}}{RT}$$

Where:
$k'_{3c} = \frac{k_{3c}K_{3b}K_2[\blacksquare]}{RT}$
$r_{3c} = k'_{3c}P_{O_2}n[\mathrm{e}^-]^{n+1}$

d. Reaction rate expression for the RDS:

$$r_4 = k_4[HO\blacksquare][CH_3CH_2O*] = r \quad (RDS)$$

e. QSSA for the $OH\blacksquare$:

$$\frac{d[HO\blacksquare]}{dt} = r_{3c} - r_4$$
$$\frac{d[HO\blacksquare]}{dt} = k'_{3c}P_{O_2}n[\mathrm{e}^-]^{n+1} - k_4[HO\blacksquare][CH_3CH_2O*] \cong 0$$

$$k'_{3c}P_{O_2}n[\mathrm{e}^-]^{n+1} = k_4[HO\blacksquare][CH_3CH_2O*]$$

$$[\mathrm{e}^-]^{n+1} = \frac{k_4[HO\blacksquare][CH_3CH_2O*]}{k'_{3c}P_{O_2}n}$$

Since $r_4 = r\ (RDS)$

$$[\mathrm{e}^-] = \left(\frac{r}{nk'_{3c}P_{O_2}}\right)^{\frac{1}{n+1}}$$

C. $HOO\blacksquare$

a. Set of elementary steps for acetaldehyde formation

$$CH_3CH_2OH + * + \blacksquare \rightleftharpoons CH_3CH_2O* + H\blacksquare \quad (1)$$

$$O_2 + \blacksquare \rightleftharpoons O_2\blacksquare \quad (2)$$

$$H\blacksquare \rightleftharpoons H^{n+}\blacksquare + ne^- \quad (3a)$$

$$O_2\blacksquare + H^{n+}\blacksquare + ne^- \rightarrow HOO\blacksquare + \blacksquare \quad (3b)$$

$$CH_3CH_2O* + HOO\blacksquare \rightleftharpoons CH_3CHO* + HOOH\blacksquare \quad (4)$$

$$HOOH\blacksquare + H\blacksquare \rightleftharpoons H_2O\blacksquare + HO\blacksquare \quad (5)$$

$$HOO\blacksquare + \blacksquare \rightleftharpoons O\blacksquare + HO\blacksquare \quad (6)$$

$$H\blacksquare + HO\blacksquare \rightleftharpoons H_2O\blacksquare + \blacksquare \quad (7)$$

$$CH_3CHO* \rightleftharpoons CH_3CHO + * \quad (8)$$

$$H_2O\blacksquare \rightleftharpoons H_2O + \blacksquare \quad (9)$$

b. Reaction rate expression for a fast and irreversible oxygen activation ($r_{+3b} \gg r_{-3b}$)

$r_{3b} = k_{3b}[O_2\blacksquare][\mathrm{e}^-]^n[H^{n+}\blacksquare]$

c. Equilibrium condition to get a concentration dependence for the adsorbed species:

$r_2 = k_{+2}[O_2][\blacksquare] - k_{-2}[O_2\blacksquare] \approx 0$
$[O_2\blacksquare] = K_2[O_2][\blacksquare]$

Then,

$r_{3b} = k_{3b}[O_2\blacksquare][\mathrm{e}^-]^n[H^{n+}\blacksquare]$
Assuming that the concentration of protons $[H^{n+}\blacksquare]$ is equal to the concentration of $n[\mathrm{e}^-]$ transferred from the principle of electroneutrality.

$r_{3b} = k_{3b}[O_2\blacksquare]n[\mathrm{e}^-]^{n+1}$

Then,

$r_{3b} = k_{3b}K_2[O_2][\blacksquare]n[\mathrm{e}^-]^{n+1}$
$[O_2] = \frac{P_{O_2}}{RT}$

Where,
$k'_{3b} = \frac{k_{3b}K_2[\blacksquare]}{RT}$
$r_{3b} = k'_{3b}P_{O_2}n[\mathrm{e}^-]^{n+1}$

d. Reaction rate expression for the RDS:

$$r_4 = k_4[HOO\blacksquare][CH_3CH_2O*] = r \quad (RDS)$$

e. QSSA for the $HOO\blacksquare$

$$\frac{d[HOO\blacksquare]}{dt} = r_{3b} - r_4$$
$$\frac{d[HOO\blacksquare]}{dt} = k'_{3b}P_{O_2}n[\mathrm{e}^-]^{n+1} - k_4[HOO\blacksquare][CH_3CH_2O*] \cong 0$$

$$k'_{3b}P_{O_2}n[\mathrm{e}^-]^{n+1} = k_4[HOO\blacksquare][CH_3CH_2O*]$$

$$[\mathrm{e}^-] = \left(\frac{k_4[HOO\blacksquare][CH_3CH_2O*]}{nk'_{3b}P_{O_2}}\right)^{\frac{1}{n+1}}$$

Since $r_4 = r\ (RDS)$

$$[\mathrm{e}^-] = \left(\frac{r}{nk'_{3b}P_{O_2}}\right)^{\frac{1}{n+1}}$$

D. ${O_2}^{n-}\blacksquare$

a. Set of elementary steps for acetaldehyde formation

$$CH_3CH_2OH + * + \blacksquare \rightleftharpoons CH_3CH_2O* + H\blacksquare \qquad (1)$$

$$O_2 + \blacksquare \rightleftharpoons O_2\blacksquare \quad (2)$$

$$H\blacksquare \rightleftharpoons H^{n+}\blacksquare + ne^- \quad (3a)$$

$$O_2\blacksquare + ne^- \rightarrow {O_2}^{n-}\blacksquare \quad (3b)$$

$$CH_3CH_2O* + {O_2}^{n-}\blacksquare \rightleftharpoons CH_3CHO* + HOO\blacksquare + ne^- \quad (4)$$

$$H^{n+}\blacksquare + {O_2}^{n-}\blacksquare \rightleftharpoons HOO\blacksquare + \blacksquare \quad (5)$$

$$HOO\blacksquare + H\blacksquare \rightleftharpoons HOOH\blacksquare + \blacksquare \quad (6)$$

$$HOOH\blacksquare + H\blacksquare \rightleftharpoons H_2O\blacksquare + HO\blacksquare \quad (7)$$

$$HOO\blacksquare + \blacksquare \rightleftharpoons O\blacksquare + HO\blacksquare \quad (8)$$

$$H\blacksquare + HO\blacksquare \rightleftharpoons H_2O\blacksquare + \blacksquare \quad (9)$$

$$CH_3CHO* \rightleftharpoons CH_3CHO + * \quad (10)$$

$$H_2O\blacksquare \rightleftharpoons H_2O + \blacksquare \quad (11)$$

b. Reaction rate expression for a fast and irreversible oxygen activation ($r_{+3b} \gg r_{-3b}$)

$$r_{3b} = k_{3b}[O_2\blacksquare\ ][\mathrm{e}^-]^n$$

c. Equilibrium condition to find a concentration dependence for the adsorbed species:

Step in equilibrium:
$r_2 = k_{+2}[O_2][\blacksquare] - k_{-2}[O_2\ \blacksquare] \approx 0$
$[O_2\ \blacksquare] = K_2[O_2][\blacksquare]$

From the irreversible step 3b:

$r_{3b} = k_{3b}[O_2\blacksquare\ ][\mathrm{e}^-]^n$
$r_{3b} = k_{3b}K_2[O_2][\blacksquare][\mathrm{e}^-]^n$

Where,

$k'_{3b} = \frac{k_{3b}K_2[\blacksquare]}{RT}$
$r_{3b} = k'_{3b}P_{O_2}[\mathrm{e}^-]^n$

d. Reaction rate expression for the RDS:

$$r_4 = k_4[{O_2}^{n-}\blacksquare][CH_3CH_2O*] = r \quad (RDS)$$

e. QSSA for the ${O_2}^{n-}\blacksquare$:

$\frac{d[{O_2}^{n-}\blacksquare]}{dt} = r_{3b} - r_4$
$\frac{d[{O_2}^{n-}\blacksquare]}{dt} = k'_{3b}P_{O_2}[\mathrm{e}^-]^n \ - k_4[{O_2}^{n-}\blacksquare][CH_3CH_2O*] = 0$

$k'_{3b}P_{O_2}[\mathrm{e}^-]^n \ = k_4[{O_2}^{n-}\blacksquare][CH_3CH_2O*]$

$[\mathrm{e}^-]^n = \frac{k_4[{O_2}^{n-}\blacksquare][CH_3CH_2O*]}{k'_{3b}P_{O_2}}$
Since $r_4 = r\ (RDS)$

$[\mathrm{e}^-] = \left(\frac{r}{k'_{3b}P_{O_2}}\right)^{\frac{1}{n}}$

S4. CT-SKAn Experimental Methodology.

The in situ reaction cell used for the measurements and UV-Vis spectrometer were described in **Section 2.4.1**. Once the catalyst was loaded (25 mg of commercial Au(3nm)/TiO_2), it was also pretreated in an identical manner, in a flow of 10%O_2/Ar at 400 °C (10 °C/min) for 1 h. Then, the temperature was set to 240 °C at a fixed ethanol partial pressure of 1 kPa, and oxygen partial pressures between 0.8 and 1.5 kPa (at increases of ~0.2 kPa). The total volumetric flow rate was 80 cm^3/min. For the experimental condition of 1 kPa of ethanol and 1.5 kPa of oxygen, the gas flow rates of He and 10%O_2/Ar fed were 67.4 cm^3/min and 11.84 cm^3/min, respectively. The liquid flow rate of ethanol injected to the system was 113μL/h. The concentration of ethanol was kept constant (1 kPa, 113 μL/h), while the partial pressure of O_2 was changed every ~2 min by adjusting the flowrates of O_2 and He. For all these reaction conditions, the concentrations of the reactants and products were tracked with a MS. MS calibration curves for ethanol and oxygen were generated separately by feeding known concentrations (partial pressure) of these species to the experimental set up and recording the corresponding signal intensity in the MS. The m/z=32 was assigned to O_2, while m/z=31 was used for ethanol. The use of m/z=31 for ethanol was justified since the contributions from products such as acetaldehyde, acetic acid, and ethyl acetate to this m/z fragment was negligible (See MS **Table S15**) and ethanol conversion was kept low (<15%) for all experimental runs. A sample experiment with MS gas phase analysis is shown in **Table S16**.

The CT-SKAn ethanol oxidation experiment was performed at 240 °C as well as at non-reacting conditions of 110 °C to record initial partial pressures (or concentrations). Absorbance and MS concentration data were simultaneously collected, so that ethanol and oxygen conversion could be determined. An ethanol oxidation experiment was performed in the in situ cell where the outlet gas was also analyzed by an online GC to validate the MS results. The data is presented in **Table S17.** Details on the GC analytical system are provided in the next section. The partial pressure of oxygen was calculated as an average of the inlet and outlet partial pressures. For simplicity, ethanol conversion and conversion rate were calculated based on partial pressure values determined from calibrations as follows:

Conversion:

$$X_i(\%) = \frac{\dot{n}_i^{in} - \dot{n}_i^{out}}{\dot{n}_i^{in}} \times 100 = \frac{P_i^{in}\dot{V}_T/RT - P_i^{out}\dot{V}_T/RT}{P_i^{in}\dot{V}_T/RT} \times 100 = \frac{P_i^{in} - P_i^{out}}{P_i^{in}} \times 100$$

Where $\dot{n}_i^{in}$ and $\dot{n}_i^{out}$ are the inlet and outlet molar flow rates of reactant *i* (EtOH, O_2). $\dot{V}_T$, T, and R are the total flow rate of the feed, reaction temperature, and gas constant. P_i^{out} and P_i^{in} are the partial pressures of the reactant i (EtOH, O_2) at the outlet and inlet of the reactor. They are calculated from MS data at reaction conditions (240 °C) and at non-reacting conditions (110 °C), respectively.

Specific reaction rate:

$$r_i\left(\frac{\mu mol}{mgcat\ s}\right) = \frac{\dot{n}_i^{in}}{w_{cat}(mg)}\frac{X_i(\%)}{100} = \frac{P_i^{in}\dot{V}_T}{RT}\frac{1}{w_{cat}}\frac{X_i(\%)}{100}$$

Where, r_i is ethanol specific conversion rate in μmol/(mg-cat s), P_i^{in} is ethanol inlet partial pressure in kPa, $\dot{V}_T$ is the feed flow rate in L/s, R is 8.314 (L kPa)/(mol K), T is 298 K, and w_{cat} is the weight of catalyst loaded in the cell (~25 mg).

For the in situ UV-Vis measurements in the d-d transition region, it was assumed that absorbance values were directly proportional to charge transfer in the small range of reaction conditions tested. Therefore, they were used in their uncalibrated form in the regression of the models. To eliminate possible contributions from the bare support, identical runs were performed at reaction conditions on TiO_2. After this, a difference spectra procedure was followed where the absorbance of TiO_2 was subtracted from that of Au/TiO_2 at identical reaction conditions. This difference spectra procedure is justified since there are two possible reaction zones. The first one is the primary reaction zone. This zone includes the Au nanoparticles and TiO_2 support in the vicinity of the Au-TiO_2 perimeter. The second one is an extended reaction zone (the bare TiO_2 support far from the Au nanoparticle). Our main interest is in the primary reaction zone, where O_2 is activated and reacts with ethoxide. Electron transfer occurs during ethanol dehydrogenation on Au which transfers to the Au/TiO_2 interface where the support is partially reduced. From the DFT calculations it is surmised that this charge at the Au/TiO_2 interface activates O_2. If any reaction occurs in the extended reaction zone, any TiO_2 support contribution to charge transfer in the Au/TiO_2 catalyst is accounted for in the above difference spectra procedure. This difference spectra procedure is straightforward for steady-state UV-Vis experiments. However, for MES data the difference spectra procedure is not trivial. Please refer to the end of this document (**Section S7**) for an extended and detailed tutorial on UV-Vis modulation excitation spectroscopy including the removal of background contributions.

S5. Fixed-Bed Reactor Experiments.

Ethanol oxidation reaction was performed in a downflow fashion in a continuous vertical fixed bed reactor made of 304 SS (1/2" OD, 0.444" ID, 427mm long, McMaster-Carr, P/N 89895K743). The powdered catalyst sample (particle size in the 38-75μ range) was placed on a coarse quartz wool bed into a quartz tube (8 mm ID 10 mm OD, 430 mm long, Technical GlassProducts). The reactor was heated in a high temperature split tube furnace (EQ-OTF1200X-S-H-110V, MTI Corp.) and the temperature was controlled (GSL-1100X-NT-110-LD, MTI Corp). The catalyst sample (commercial Au(3nm)/TiO_2) was loaded to the reactor and pre-treated under a flow of 10%O_2/Ar (35 cm^3/min) at 400˚C (1 ˚ C/min) for 1 h. Reaction conditions were set by flowing oxygen through the reactor (1.5 kPa) and injecting ethanol (1 kPa) into the system by means of a high-pressure programmable syringe pump. After steady state conditions were reached at 240˚C, the concentration of unreacted reactants and products were measured in an online gas chromatograph (SRI 8610C GC) with a Rt-Q-BOND PLOT column (30mx0.53mm, 20μm, P/N 19742-6850, RESTEK), coupled to a methanizer and a flame ionization detector (FID).

An experiment was run in the fixed bed reactor described above under conditions identical to those for the CT-SKAn methodology in the in situ reaction cell (**Section S2**). Ethanol conversion and

product selectivities based on fixed bed reactor performance test are presented in **Table S17**. They indicated that ethanol conversion was ~8%. This conversion was similar to the ~10% conversion observed in the in situ cell when gas phase was characterized via online MS (**Tables S16** and **S17**) and to ~7% when characterized with an online GC (**Tables S16** and **S18**). As shown in **Tables S17** and **S18,** the main products of ethanol oxidation on Au/TiO_2 were acetaldehyde (87-94%), acetic acid (3-5%), and ethyl acetate (4-6%) in the fixed bed reactor and the in situ cell.

S6. F Test on Model Variances at the 95% Confidence Level.

Hypotheses:

H_0: $The\ model\ variances\ are\ not\ significantly\ different.$

H_1: $The\ model\ variances\ are\ significantly\ different.$

Where,

$$S_r^2 = \frac{\sum_{i=1}^{N}(Abs_i^{Exp} - Abs_i^{Model})^2}{N-1}$$

Here, N is the total number of data points in the experiment (29 in the present work), Abs_i^{Exp} is the experimental measurement and Abs_i^{Model} is the value predicted by the model [2].

Now, in order to compare the variances among the different models:

Hypotheses:

$$H_0: \sigma_k^2 = \sigma_l^2$$

$$H_1: \sigma_k^2 \neq \sigma_l^2$$

Test statistic:

$$F = \frac{S_k^2}{S_l^2}$$

Where S_k^2 and S_l^2 are the variances of model k and l, respectively. A strong deviation of this ratio from 1 indicates a significant difference in the sample variances.

The null (H_0) hypothesis is rejected if:

$$F < F_{1-\frac{\alpha}{2},N_k-1,N_l-1} \ \ or \ \ F > F_{\frac{\alpha}{2},N_k-1,N_l-1}$$

Here, F_{α,N_k-1,N_l-1} is the critical F, α is the significance level, and $N_k - 1$ and $N_l - 1$ are the degrees of freedom of the sample k and l, respectively.

Table S1. Site statistics for the top slice of a truncated octahedron supported on a (111) plane: Top (layers) surface and bulk atoms (excluding interface) calculation formulas. Adapted from Ref. [3].

Description	**Acronym**	**CN**	**Formula (m>2, l = m+1)**
Corner	tS-C	6	tS-C = 12
Edge (hexagonal face-hexagonal face)	tS-EHH	7	tS-EHH = $3(m-2)+6(l-m-1)$
Edge (hexagonal face-square face)	tS-EHS	7	tS-EHS = $12(m-2)$
Square face	tS-SF	8	tS-SF = $3(m-2)^2$
Hexagonal face	tS-HF	9	tS-HF = $-\frac{3}{2}m^2+9ml-\frac{33}{2}m-12l+25$
Bulk	B_t	12	$B_t = -m^3-\frac{1}{3}l^3+\frac{9}{2}m^2l+\frac{3}{2}ml^2-\frac{9}{2}m^2-18ml+\frac{53}{2}m+\frac{28}{3}l-16$
Total top surface atoms	n_{tS}	6-9	n_{tS}=tS-C + tS-EHH + tS-EHS + tS-SF + tS-HF
Total top atoms	n_t		$n_t = n_{tS} + B_t$

Nomenclature:
m = number of atoms in a single edge
l = number of atom layers in a particle
CN = coordination number
d = apparent particle diameter

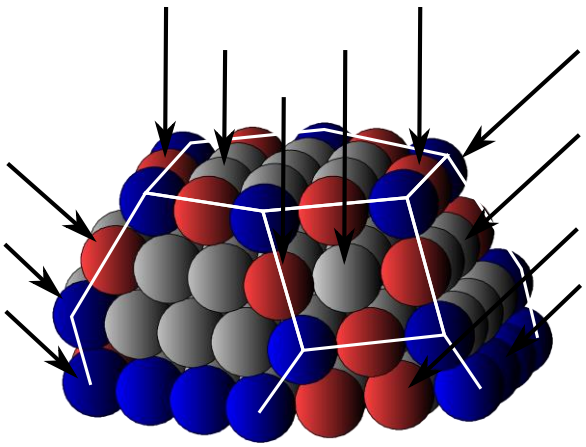

Top slice of a truncated octahedron model for site statistics of gold nanoparticles (m = 3, l = m+1). Acronyms: S: top surface atoms; I: interface atoms; EHS-edge (hexagonal face-square face) atoms; EHH: edge (hexagonal face-hexagonal face) atoms; HF: hexagonal face atoms; SF: square face atoms; EHI: edge (hexagonal face inward sloping); EHO: (hexagonal face outward sloping).

Table S2. Site statistics for the top slice of a truncated octahedron supported on a (111) plane: Interface (bottom layer) surface and bulk atoms calculation formulas. Adapted from Ref. [3].

Description	**Acronym**	**CN**	**Formula (m>2, l = m+1)**
Corner	iS-C	5	iS-C $= 6$
Edge (hexagonal face-outward sloping)	iS-EHO	6	iS-EHO $= 3(m + l - 3)$
Edge (hexagonal face-inward sloping)	iS-EHI	7	iS-EHI $= 3(l - 2)$
Bulk (interface)	B_i	9	$B_i = \frac{9}{2}m^2 - l^2 + 3ml - \frac{33}{2}m - l + 12$
Total surface interface atoms	n_{iS}	5-7	n_{iS} = iS-C + iS-EHO + iS-EHI
Total interface atoms	n_i		$n_i = n_{iS} + B_i$

Nomenclature:
m = number of atoms in a single edge
l = number of atom layers in a particle
CN = coordination number
d = apparent particle diameter

Table S3. Site statistics for the top slice of a truncated octahedron supported on a (111) plane: Apparent diameter and dispersion calculation formulas. Adapted from Ref. [3].

Description	Acronym	CN	Formula (m>2, l = m+1)
Top hexagon average side length	S_t	-	$S_t = (m-1)$
Interface hexagon average side length	S_i	-	$S_i = 1.5(m-1)$
Particle average hexagon side length	S	-	$S = 0.5(S_t + S_i)$
Particle average hexagon diameter (nm)	d_H	-	$d_H = 2S \times 0.2884$ Gold atomic diameter = 0.2884 nm
Particle average apparent diameter (nm)	d	-	$d = d_H + 0.2884$
Total atoms	n_T	-	$n_T = n_t + n_i$
Total surface atoms	n_S	5-9	$n_S = n_{tS} + n_{iS}$
Fraction of total surface atoms (Dispersion)	D_S	5-9	$D_S = n_S/n_T$
Fraction of total top surface atoms	D_{tS}	6-9	$D_{tS} = n_{tS}/n_T$
Fraction of top surface corner atoms	D_{tSC}	6	$D_{tSC} = (tS\text{-}C)/n_T$
Fraction of top surface corner atoms	D_{tSCE}	6	$D_{tSC} = (tS\text{-}C+tS\text{-}EHH+tS\text{-}EHS)/n_T$
Fraction of interface (perimeter) surface atoms	D_i	5-7	$D_i = n_{iS}/n_T$
Fraction of interface surface corner atoms	D_{iSC}	5	$D_{iSC} = (iS\text{-}C)/n_T$
Fraction of interface surface edge atoms	D_{iE}	6-7	$D_{tSC} = (iS\text{-}EHO+iS\text{-}EHI)/n_T$

Nomenclature:
m = number of atoms in a single edge
l = number of atom layers in a particle
CN = coordination number
d = apparent particle diameter

Table S4. Detailed results of site statistics for Au NPs using formulas from **Table S1** to **Table S3**. Reproduced with permission from Ref. [4].

	A	B	C	D	E	F	G	H	I	J	K	L	M	N	O	P	Q	R	S	T	U	V
1	**Site Statistics Top Slice of Truncated Octahedron Supported on a (111) Plane**																					
2																						
3	m	number of atoms in a single edge		m>2		J. Phys. Chem. B 2006, 110, 11, 5286 (Formulas in Supporting Information File)																
4	l=m+1	number of atom layers in a particle				Anna Carlsson, Anna Puig-Molina, and Ton V. W. Janssens																
5						http://pubs.acs.org/doi/suppl/10.1021/jp0569537																	
6				m																		
7		Top Layers Surface and Bulk Atoms	CN	2	3	4	5	6	7	8	9	10	11	12	13	14	15	16	17	18	19	20
8	tS-C	Corner	6	12	12	12	12	12	12	12	12	12	12	12	12	12	12	12	12	12	12	12
9	tS-EHH	Edge HF-HF	7	0	3	6	9	12	15	18	21	24	27	30	33	36	39	42	45	48	51	54
10	tS-EHS	Edge HF-SF	7	0	12	24	36	48	60	72	84	96	108	120	132	144	156	168	180	192	204	216
11	tS-SF	Square Face	8	0	3	12	27	48	75	108	147	192	243	300	363	432	507	588	675	768	867	972
12	tS-HF	Hexagonal Face	9	4	22	55	103	166	244	337	445	568	706	859	1027	1210	1408	1621	1849	2092	2350	2623
13	Bt	Bulk	12	3	30	109	268	535	938	1505	2264	3243	4470	5973	7780	9919	12418	15305	18608	22355	26574	31293
14	ntS	Total Top Surface		16	52	109	187	286	406	547	709	892	1096	1321	1567	1834	2122	2431	2761	3112	3484	3877
15	nt	Total Top		19	82	218	455	821	1344	2052	2973	4135	5566	7294	9347	11753	14540	17736	21369	25467	30058	35170
16		Interface Surface and Bulk Atoms	CN																			
17	iS-C	Corner	5	6	6	6	6	6	6	6	6	6	6	6	6	6	6	6	6	6	6	6
18	iS-EHO	Edge HF-OS	6	0	6	12	18	24	30	36	42	48	54	60	66	72	78	84	90	96	102	108
19	iS-EHI	Edge HF-IS	7	3	6	9	12	15	18	21	24	27	30	33	36	39	42	45	48	51	54	57
20	Bi	Bulk	9	3	19	48	90	145	213	294	388	495	615	748	894	1053	1225	1410	1608	1819	2043	2280
21	niS	Total Interface Surface		9	18	27	36	45	54	63	72	81	90	99	108	117	126	135	144	153	162	171
22	ni	Total Interface		12	37	75	126	190	267	357	460	576	705	847	1002	1170	1351	1545	1752	1972	2205	2451
23		Total Atoms in Particle																				
24	nT	Total Atoms		31	119	293	581	1011	1611	2409	3433	4711	6271	8141	10349	12923	15891	19281	23121	27439	32263	37621
25	nS	Total Surface		25	70	136	223	331	460	610	781	973	1186	1420	1675	1951	2248	2566	2905	3265	3646	4048
26	St	Top Hx Average Side Length		1	2	3	4	5	6	7	8	9	10	11	12	13	14	15	16	17	18	19
27	Si	Interface Hx Aver Side Length		1.5	3	4.5	6	7.5	9	10.5	12	13.5	15	16.5	18	19.5	21	22.5	24	25.5	27	28.5
28	S	Particle Aver Hx Side Length		1.25	2.5	3.75	5	6.25	7.5	8.75	10	11.25	12.5	13.75	15	16.25	17.5	18.75	20	21.25	22.5	23.75
29	dH	Particle Aver Hx Diameter, nm		0.72	1.44	2.16	2.88	3.61	4.33	5.05	5.77	6.49	7.21	7.93	8.65	9.37	10.09	10.82	11.54	12.26	12.98	13.70
30	d	Particle App Diameter, nm		1.01	1.73	2.45	3.17	3.89	4.61	5.34	6.06	6.78	7.50	8.22	8.94	9.66	10.38	11.10	11.82	12.55	13.27	13.99
31		Dispersion	CN																			
32	DS	Fraction Surface Atoms nS/nT	5-9	8.06E-01	5.88E-01	4.64E-01	3.84E-01	3.27E-01	2.86E-01	2.53E-01	2.27E-01	2.07E-01	1.89E-01	1.74E-01	1.62E-01	1.51E-01	1.41E-01	1.33E-01	1.26E-01	1.19E-01	1.13E-01	1.08E-01
33	DtS	Fraction Top Surface Atoms ntS/nT	6-9	5.16E-01	4.37E-01	3.72E-01	3.22E-01	2.83E-01	2.52E-01	2.27E-01	2.07E-01	1.89E-01	1.75E-01	1.62E-01	1.51E-01	1.42E-01	1.34E-01	1.26E-01	1.19E-01	1.13E-01	1.08E-01	1.03E-01
34	DtSC	Fract Top Surf Corner At tS-C/nT	6	3.87E-01	1.01E-01	4.10E-02	2.07E-02	1.19E-02	7.45E-03	4.98E-03	3.50E-03	2.55E-03	1.91E-03	1.47E-03	1.16E-03	9.29E-04	7.55E-04	6.22E-04	5.19E-04	4.37E-04	3.72E-04	3.19E-04
35	DtSCE	Fract Top Surf Corner-Edge At tS-CE/nT	6-7	3.87E-01	2.27E-01	1.43E-01	9.81E-02	7.12E-02	5.40E-02	4.23E-02	3.41E-02	2.80E-02	2.34E-02	1.99E-02	1.71E-02	1.49E-02	1.30E-02	1.15E-02	1.03E-02	9.18E-03	8.28E-03	7.50E-03
36	Di	Fract Interface Surf At niS/nT	5-7	2.90E-01	1.51E-01	9.22E-02	6.20E-02	4.45E-02	3.35E-02	2.62E-02	2.10E-02	1.72E-02	1.44E-02	1.22E-02	1.04E-02	9.05E-03	7.93E-03	7.00E-03	6.23E-03	5.58E-03	5.02E-03	4.55E-03
37	DiSC	Fract Int Surf Corner At iS-C/nT	5	1.94E-01	5.04E-02	2.05E-02	1.03E-02	5.93E-03	3.72E-03	2.49E-03	1.75E-03	1.27E-03	9.57E-04	7.37E-04	5.80E-04	4.64E-04	3.78E-04	3.11E-04	2.60E-04	2.19E-04	1.86E-04	1.59E-04
38	DiE	Fract Int Surf Edge At iS-E/nT	6-7	9.68E-02	1.01E-01	7.17E-02	5.16E-02	3.86E-02	2.98E-02	2.37E-02	1.92E-02	1.59E-02	1.34E-02	1.14E-02	9.86E-03	8.59E-03	7.55E-03	6.69E-03	5.97E-03	5.36E-03	4.84E-03	0.00439

Table S5. DFT Hirschfeld charges calculated for the system in **Figure 10a**.

$CH_3CH_2O^*$ + O■

Element	Atom #	Hirshfeld Charge	Element	Atom #	Hirshfeld Charge	Element	Atom #	Hirshfeld Charge
Ti	1	0.59	O	39	-0.29	O	77	-0.26
Ti	2	0.54	O	40	-0.28	O	78	-0.27
Ti	3	0.59	O	41	-0.28	O	79	-0.26
Ti	4	0.53	O	42	-0.29	O	80	-0.28
Ti	5	0.57	O	43	-0.26	O	81	-0.29
Ti	6	0.58	O	44	-0.28	O	82	-0.29
Ti	7	0.54	O	45	-0.28	O	83	-0.29
Ti	8	0.51	O	46	-0.28	O	84	-0.29
Ti	9	0.53	O	47	-0.26	O	85	-0.29
Ti	10	0.52	O	48	-0.26	O	86	-0.29
Ti	11	0.59	Ti	49	0.59	O	87	-0.28
Ti	12	0.47	Ti	50	0.53	O	88	-0.29
Ti	13	0.53	Ti	51	0.59	O	89	-0.28
Ti	14	0.53	Ti	52	0.53	O	90	-0.28
Ti	15	0.59	Ti	53	0.59	O	91	-0.26
Ti	16	0.58	Ti	54	0.59	O	92	-0.26
O	17	-0.29	Ti	55	0.53	O	93	-0.28
O	18	-0.29	Ti	56	0.52	O	94	-0.28
O	19	-0.29	Ti	57	0.53	O	95	-0.26
O	20	-0.29	Ti	58	0.53	O	96	-0.26
O	21	-0.29	Ti	59	0.55	Au	97	0.08
O	22	-0.29	Ti	60	0.56	Au	98	0.07
O	23	-0.30	Ti	61	0.53	Au	99	0.04
O	24	-0.29	Ti	62	0.53	Au	100	0.11
O	25	-0.26	Ti	63	0.57	Au	101	0.07
O	26	-0.26	Ti	64	0.57	H	102	0.17
O	27	-0.24	O	65	-0.29	O	103	-0.30
O	28	-0.31	O	66	-0.29	C	104	-0.12
O	29	-0.26	O	67	-0.29	C	105	-0.02
O	30	-0.24	O	68	-0.29	O	106	-0.22
O	31	-0.26	O	69	-0.29	H	107	0.04
O	32	-0.28	O	70	-0.29	H	108	0.03
O	33	-0.29	O	71	-0.29	H	109	0.05
O	34	-0.29	O	72	-0.29	H	110	0.03
O	35	-0.29	O	73	-0.26	H	111	0.04
O	36	-0.29	O	74	-0.26	H	112	0.17
O	37	-0.29	O	75	-0.28	**Total**		**0**
O	38	-0.29	O	76	-0.28			

Table S6. DFT Hirschfeld charges calculated for the system in **Figure 10e**.

$CH_3CHO^* + OH$■

Element	Atom #	Hirshfeld Charge	Element	Atom #	Hirshfeld Charge	Element	Atom #	Hirshfeld Charge
Ti	1	0.58	O	40	-0.28	O	79	-0.26
Ti	2	0.53	O	41	-0.28	O	80	-0.29
Ti	3	0.58	O	42	-0.28	O	81	-0.30
Ti	4	0.52	O	43	-0.26	O	82	-0.30
Ti	5	0.57	O	44	-0.28	O	83	-0.30
Ti	6	0.58	O	45	-0.28	O	84	-0.29
Ti	7	0.53	O	46	-0.28	O	85	-0.29
Ti	8	0.51	O	47	-0.26	O	86	-0.29
Ti	9	0.53	O	48	-0.26	O	87	-0.29
Ti	10	0.53	Ti	49	0.58	O	88	-0.29
Ti	11	0.58	Ti	50	0.52	O	89	-0.28
Ti	12	0.50	Ti	51	0.59	O	90	-0.28
Ti	13	0.53	Ti	52	0.52	O	91	-0.26
Ti	14	0.53	Ti	53	0.58	O	92	-0.26
Ti	15	0.58	Ti	54	0.58	O	93	-0.28
Ti	16	0.56	Ti	55	0.52	O	94	-0.28
O	17	-0.29	Ti	56	0.51	O	95	-0.26
O	18	-0.29	Ti	57	0.53	O	96	-0.26
O	19	-0.29	Ti	58	0.53	Au	97	0.04
O	20	-0.29	Ti	59	0.54	Au	98	-0.07
O	21	-0.29	Ti	60	0.55	Au	99	0.11
O	22	-0.29	Ti	61	0.53	Au	100	0.12
O	23	-0.31	Ti	62	0.53	Au	101	0.06
O	24	-0.30	Ti	63	0.56	H	102	0.16
O	25	-0.26	Ti	64	0.56	O	103	-0.27
O	26	-0.26	O	65	-0.29	C	104	-0.10
O	27	-0.24	O	66	-0.30	C	105	0.15
O	28	-0.30	O	67	-0.30	O	106	-0.15
O	29	-0.26	O	68	-0.30	H	107	0.04
O	30	-0.24	O	69	-0.29	H	108	0.08
O	31	-0.26	O	70	-0.30	H	109	0.07
O	32	-0.31	O	71	-0.29	H	110	0.06
O	33	-0.29	O	72	-0.29	H	111	0.16
O	34	-0.30	O	73	-0.26	H	112	0.14
O	35	-0.30	O	74	-0.26	**Total**		**0**
O	36	-0.29	O	75	-0.28			
O	37	-0.29	O	76	-0.28			
O	38	-0.29	O	77	-0.26			
O	39	-0.29	O	78	-0.29			

Table S7. DFT Hirschfeld charges calculated for the system in **Figure 10b**.

$CH_3CH_2O^* + OH$ ■

Element	Atom #	Hirshfeld Charge	Element	Atom #	Hirshfeld Charge	Element	Atom #	Hirshfeld Charge
Ti	1	0.59	O	39	-0.28	O	77	-0.26
Ti	2	0.53	O	40	-0.28	O	78	-0.28
Ti	3	0.59	O	41	-0.28	O	79	-0.26
Ti	4	0.53	O	42	-0.28	O	80	-0.28
Ti	5	0.58	O	43	-0.26	O	81	-0.29
Ti	6	0.58	O	44	-0.28	O	82	-0.29
Ti	7	0.55	O	45	-0.28	O	83	-0.29
Ti	8	0.52	O	46	-0.28	O	84	-0.29
Ti	9	0.53	O	47	-0.26	O	85	-0.29
Ti	10	0.53	O	48	-0.26	O	86	-0.29
Ti	11	0.60	Ti	49	0.59	O	87	-0.29
Ti	12	0.52	Ti	50	0.53	O	88	-0.29
Ti	13	0.53	Ti	51	0.58	O	89	-0.28
Ti	14	0.53	Ti	52	0.53	O	90	-0.28
Ti	15	0.58	Ti	53	0.58	O	91	-0.26
Ti	16	0.58	Ti	54	0.59	O	92	-0.26
O	17	-0.29	Ti	55	0.52	O	93	-0.28
O	18	-0.29	Ti	56	0.52	O	94	-0.28
O	19	-0.29	Ti	57	0.53	O	95	-0.26
O	20	-0.29	Ti	58	0.53	O	96	-0.26
O	21	-0.29	Ti	59	0.54	Au	97	0.08
O	22	-0.29	Ti	60	0.57	Au	98	0.06
O	23	-0.30	Ti	61	0.53	Au	99	0.04
O	24	-0.30	Ti	62	0.53	Au	100	0.11
O	25	-0.26	Ti	63	0.57	Au	101	0.05
O	26	-0.26	Ti	64	0.57	H	102	0.17
O	27	-0.24	O	65	-0.29	O	103	-0.26
O	28	-0.29	O	66	-0.29	C	104	-0.12
O	29	-0.26	O	67	-0.30	C	105	-0.02
O	30	-0.28	O	68	-0.29	O	106	-0.22
O	31	-0.26	O	69	-0.29	H	107	0.04
O	32	-0.28	O	70	-0.29	H	108	0.03
O	33	-0.29	O	71	-0.29	H	109	0.05
O	34	-0.29	O	72	-0.29	H	110	0.03
O	35	-0.30	O	73	-0.26	H	111	0.04
O	36	-0.29	O	74	-0.26	H	112	0.15
O	37	-0.29	O	75	-0.28	**Total**		**0**
O	38	-0.29	O	76	-0.28			

Table S8. DFT Hirschfeld charges calculated for the system in **Figure 10f**.

$CH_3CHO^* + H_2O$■

Element	Atom #	Hirshfeld Charge	Element	Atom #	Hirshfeld Charge	Element	Atom #	Hirshfeld Charge
Ti	1	0.58	O	39	-0.29	O	77	-0.26
Ti	2	0.52	O	40	-0.29	O	78	-0.29
Ti	3	0.59	O	41	-0.28	O	79	-0.26
Ti	4	0.51	O	42	-0.28	O	80	-0.29
Ti	5	0.58	O	43	-0.26	O	81	-0.30
Ti	6	0.58	O	44	-0.26	O	82	-0.30
Ti	7	0.53	O	45	-0.28	O	83	-0.30
Ti	8	0.51	O	46	-0.28	O	84	-0.29
Ti	9	0.53	O	47	-0.26	O	85	-0.29
Ti	10	0.53	O	48	-0.26	O	86	-0.29
Ti	11	0.58	Ti	49	0.58	O	87	-0.29
Ti	12	0.52	Ti	50	0.51	O	88	-0.29
Ti	13	0.53	Ti	51	0.58	O	89	-0.28
Ti	14	0.53	Ti	52	0.52	O	90	-0.28
Ti	15	0.56	Ti	53	0.58	O	91	-0.26
Ti	16	0.56	Ti	54	0.58	O	92	-0.26
O	17	-0.29	Ti	55	0.52	O	93	-0.28
O	18	-0.29	Ti	56	0.51	O	94	-0.28
O	19	-0.31	Ti	57	0.53	O	95	-0.26
O	20	-0.30	Ti	58	0.53	O	96	-0.26
O	21	-0.29	Ti	59	0.53	Au	97	0.05
O	22	-0.29	Ti	60	0.56	Au	98	-0.07
O	23	-0.30	Ti	61	0.53	Au	99	0.12
O	24	-0.30	Ti	62	0.53	Au	100	0.13
O	25	-0.26	Ti	63	0.56	Au	101	0.04
O	26	-0.26	Ti	64	0.56	H	102	0.16
O	27	-0.25	O	65	-0.29	O	103	-0.17
O	28	-0.31	O	66	-0.29	C	104	-0.10
O	29	-0.26	O	67	-0.30	C	105	0.15
O	30	-0.29	O	68	-0.30	O	106	-0.15
O	31	-0.26	O	69	-0.29	H	107	0.04
O	32	-0.30	O	70	-0.29	H	108	0.08
O	33	-0.30	O	71	-0.30	H	109	0.07
O	34	-0.30	O	72	-0.29	H	110	0.06
O	35	-0.30	O	73	-0.26	H	111	0.18
O	36	-0.29	O	74	-0.26	H	112	0.13
O	37	-0.29	O	75	-0.29	**Total**		**0**
O	38	-0.29	O	76	-0.28			

Table S9. DFT Hirschfeld charges calculated for the system in **Figure 10c**.

$CH_3CH_2O^*$ + OO■

Element	Atom #	Hirshfeld Charge	Element	Atom #	Hirshfeld Charge	Element	Atom #	Hirshfeld Charge
Ti	1	0.59	O	40	-0.28	O	79	-0.26
Ti	2	0.54	O	41	-0.28	O	80	-0.28
Ti	3	0.59	O	42	-0.29	O	81	-0.29
Ti	4	0.53	O	43	-0.26	O	82	-0.29
Ti	5	0.56	O	44	-0.28	O	83	-0.29
Ti	6	0.58	O	45	-0.28	O	84	-0.29
Ti	7	0.54	O	46	-0.28	O	85	-0.29
Ti	8	0.50	O	47	-0.26	O	86	-0.29
Ti	9	0.53	O	48	-0.26	O	87	-0.29
Ti	10	0.52	Ti	49	0.58	O	88	-0.29
Ti	11	0.59	Ti	50	0.53	O	89	-0.28
Ti	12	0.47	Ti	51	0.59	O	90	-0.28
Ti	13	0.53	Ti	52	0.53	O	91	-0.26
Ti	14	0.53	Ti	53	0.59	O	92	-0.26
Ti	15	0.59	Ti	54	0.59	O	93	-0.28
Ti	16	0.58	Ti	55	0.52	O	94	-0.28
O	17	-0.29	Ti	56	0.52	O	95	-0.26
O	18	-0.29	Ti	57	0.53	O	96	-0.26
O	19	-0.29	Ti	58	0.53	Au	97	0.09
O	20	-0.29	Ti	59	0.56	Au	98	0.07
O	21	-0.29	Ti	60	0.56	Au	99	0.04
O	22	-0.29	Ti	61	0.53	Au	100	0.10
O	23	-0.30	Ti	62	0.53	Au	101	0.05
O	24	-0.29	Ti	63	0.57	H	102	0.17
O	25	-0.26	Ti	64	0.57	O	103	-0.14
O	26	-0.26	O	65	-0.29	C	104	-0.12
O	27	-0.24	O	66	-0.29	C	105	-0.02
O	28	-0.31	O	67	-0.29	O	106	-0.22
O	29	-0.26	O	68	-0.29	H	107	0.04
O	30	-0.24	O	69	-0.29	H	108	0.03
O	31	-0.26	O	70	-0.29	H	109	0.05
O	32	-0.28	O	71	-0.29	H	110	0.03
O	33	-0.29	O	72	-0.29	H	111	0.04
O	34	-0.29	O	73	-0.26	H	112	0.17
O	35	-0.29	O	74	-0.26	O	113	-0.14
O	36	-0.29	O	75	-0.28	**Total**		**0**
O	37	-0.29	O	76	-0.28			
O	38	-0.29	O	77	-0.26			
O	39	-0.29	O	78	-0.27			

Table S10. DFT Hirschfeld charges calculated for the system in **Figure 10g**.

$CH_3CH_2O^*$ + HOO■

Element	Atom #	Hirshfeld Charge	Element	Atom #	Hirshfeld Charge	Element	Atom #	Hirshfeld Charge
Ti	1	0.59	O	40	-0.28	O	79	-0.26
Ti	2	0.53	O	41	-0.28	O	80	-0.28
Ti	3	0.59	O	42	-0.28	O	81	-0.29
Ti	4	0.53	O	43	-0.26	O	82	-0.29
Ti	5	0.58	O	44	-0.28	O	83	-0.29
Ti	6	0.58	O	45	-0.28	O	84	-0.29
Ti	7	0.55	O	46	-0.28	O	85	-0.29
Ti	8	0.51	O	47	-0.26	O	86	-0.29
Ti	9	0.53	O	48	-0.26	O	87	-0.29
Ti	10	0.53	Ti	49	0.59	O	88	-0.29
Ti	11	0.60	Ti	50	0.53	O	89	-0.28
Ti	12	0.50	Ti	51	0.58	O	90	-0.28
Ti	13	0.53	Ti	52	0.53	O	91	-0.26
Ti	14	0.53	Ti	53	0.58	O	92	-0.26
Ti	15	0.58	Ti	54	0.59	O	93	-0.28
Ti	16	0.58	Ti	55	0.52	O	94	-0.28
O	17	-0.29	Ti	56	0.52	O	95	-0.26
O	18	-0.29	Ti	57	0.53	O	96	-0.26
O	19	-0.29	Ti	58	0.53	Au	97	0.09
O	20	-0.29	Ti	59	0.55	Au	98	0.06
O	21	-0.29	Ti	60	0.57	Au	99	0.04
O	22	-0.29	Ti	61	0.53	Au	100	0.11
O	23	-0.30	Ti	62	0.53	Au	101	0.05
O	24	-0.30	Ti	63	0.57	H	102	0.18
O	25	-0.26	Ti	64	0.57	O	103	-0.14
O	26	-0.26	O	65	-0.29	C	104	-0.12
O	27	-0.24	O	66	-0.29	C	105	-0.02
O	28	-0.29	O	67	-0.30	O	106	-0.22
O	29	-0.26	O	68	-0.29	H	107	0.04
O	30	-0.27	O	69	-0.29	H	108	0.03
O	31	-0.26	O	70	-0.29	H	109	0.05
O	32	-0.27	O	71	-0.29	H	110	0.03
O	33	-0.29	O	72	-0.29	H	111	0.04
O	34	-0.29	O	73	-0.26	H	112	0.13
O	35	-0.30	O	74	-0.26	O	113	-0.12
O	36	-0.29	O	75	-0.28	**Total**		**0**
O	37	-0.29	O	76	-0.28			
O	38	-0.29	O	77	-0.26			
O	39	-0.28	O	78	-0.28			

Table S11. DFT Hirschfeld charges calculated for the system in **Figure 10d**.

$CH_3CHO^* + HOO\blacksquare$

Element	Atom #	Hirshfeld Charge	Element	Atom #	Hirshfeld Charge	Element	Atom #	Hirshfeld Charge
Ti	1	0.58	O	39	-0.29	O	77	-0.26
Ti	2	0.53	O	40	-0.29	O	78	-0.29
Ti	3	0.58	O	41	-0.28	O	79	-0.26
Ti	4	0.52	O	42	-0.28	O	80	-0.29
Ti	5	0.58	O	43	-0.26	O	81	-0.29
Ti	6	0.58	O	44	-0.28	O	82	-0.30
Ti	7	0.53	O	45	-0.28	O	83	-0.29
Ti	8	0.50	O	46	-0.28	O	84	-0.29
Ti	9	0.53	O	47	-0.26	O	85	-0.29
Ti	10	0.53	O	48	-0.26	O	86	-0.29
Ti	11	0.58	Ti	49	0.58	O	87	-0.29
Ti	12	0.49	Ti	50	0.52	O	88	-0.29
Ti	13	0.53	Ti	51	0.59	O	89	-0.28
Ti	14	0.53	Ti	52	0.52	O	90	-0.28
Ti	15	0.58	Ti	53	0.58	O	91	-0.26
Ti	16	0.56	Ti	54	0.58	O	92	-0.26
O	17	-0.29	Ti	55	0.52	O	93	-0.28
O	18	-0.29	Ti	56	0.51	O	94	-0.28
O	19	-0.29	Ti	57	0.53	O	95	-0.26
O	20	-0.29	Ti	58	0.53	O	96	-0.26
O	21	-0.29	Ti	59	0.54	Au	97	0.04
O	22	-0.29	Ti	60	0.55	Au	98	-0.06
O	23	-0.31	Ti	61	0.53	Au	99	0.11
O	24	-0.30	Ti	62	0.53	Au	100	0.11
O	25	-0.26	Ti	63	0.56	Au	101	0.06
O	26	-0.26	Ti	64	0.56	H	102	0.17
O	27	-0.24	O	65	-0.29	O	103	-0.15
O	28	-0.30	O	66	-0.29	C	104	-0.10
O	29	-0.26	O	67	-0.30	C	105	0.15
O	30	-0.24	O	68	-0.30	O	106	-0.15
O	31	-0.26	O	69	-0.29	H	107	0.04
O	32	-0.29	O	70	-0.30	H	108	0.07
O	33	-0.29	O	71	-0.29	H	109	0.07
O	34	-0.29	O	72	-0.29	H	110	0.06
O	35	-0.29	O	73	-0.26	H	111	0.17
O	36	-0.29	O	74	-0.26	O	112	-0.14
O	37	-0.29	O	75	-0.28	H	113	0.12
O	38	-0.29	O	76	-0.28	**Total**		**0**

Table S12. DFT Hirschfeld charges calculated for the system in **Figure 10h**.

$CH_3CHO^* + H_2O_2$ ■

Element	Atom #	Hirshfeld Charge	Element	Atom #	Hirshfeld Charge	Element	Atom #	Hirshfeld Charge
Ti	1	0.58	O	40	-0.29	O	79	-0.26
Ti	2	0.52	O	41	-0.28	O	80	-0.29
Ti	3	0.58	O	42	-0.28	O	81	-0.29
Ti	4	0.51	O	43	-0.26	O	82	-0.30
Ti	5	0.58	O	44	-0.26	O	83	-0.30
Ti	6	0.58	O	45	-0.28	O	84	-0.29
Ti	7	0.53	O	46	-0.28	O	85	-0.29
Ti	8	0.51	O	47	-0.26	O	86	-0.29
Ti	9	0.53	O	48	-0.26	O	87	-0.29
Ti	10	0.53	Ti	49	0.58	O	88	-0.29
Ti	11	0.58	Ti	50	0.52	O	89	-0.28
Ti	12	0.50	Ti	51	0.58	O	90	-0.28
Ti	13	0.53	Ti	52	0.52	O	91	-0.26
Ti	14	0.53	Ti	53	0.58	O	92	-0.26
Ti	15	0.56	Ti	54	0.58	O	93	-0.28
Ti	16	0.56	Ti	55	0.51	O	94	-0.28
O	17	-0.29	Ti	56	0.50	O	95	-0.26
O	18	-0.29	Ti	57	0.53	O	96	-0.26
O	19	-0.31	Ti	58	0.53	Au	97	0.05
O	20	-0.30	Ti	59	0.55	Au	98	-0.06
O	21	-0.29	Ti	60	0.56	Au	99	0.13
O	22	-0.29	Ti	61	0.53	Au	100	0.13
O	23	-0.30	Ti	62	0.53	Au	101	0.03
O	24	-0.30	Ti	63	0.55	H	102	0.16
O	25	-0.26	Ti	64	0.56	O	103	-0.06
O	26	-0.26	O	65	-0.29	C	104	-0.10
O	27	-0.25	O	66	-0.29	C	105	0.15
O	28	-0.31	O	67	-0.30	O	106	-0.15
O	29	-0.26	O	68	-0.30	H	107	0.04
O	30	-0.29	O	69	-0.29	H	108	0.08
O	31	-0.26	O	70	-0.29	H	109	0.07
O	32	-0.29	O	71	-0.30	H	110	0.06
O	33	-0.30	O	72	-0.29	H	111	0.17
O	34	-0.29	O	73	-0.26	O	112	-0.14
O	35	-0.30	O	74	-0.26	H	113	0.11
O	36	-0.29	O	75	-0.29	**Total**		**0**
O	37	-0.29	O	76	-0.28			
O	38	-0.29	O	77	-0.26			
O	39	-0.29	O	78	-0.28			

Table S13. Residual sum of squares and variance for all the oxygen species models in **Figure 11.**

Oxygen Species	R^2	Residual Sum of Squares (RSS)	S_r^2
O_2^{n-} ■	0.492	2.28E-04	8.13E-06
HOO ■	0.865	5.69-05	2.03E-06
HO ■	0.865	5.69-05	2.03E-06
O^{n-} ■	0.771	9.69E-05	3.46E-06

Table S14. F-statistic ($F = S_k^2/S_l^2$) matrix for the test performed to compare the variances among the different models for all the oxygen species in **Figure 11.**

	O_2^{n-} ■ $\boldsymbol{k=1}$	HOO ■ $\boldsymbol{k=2}$	HO ■ $\boldsymbol{k=3}$	O^{n-} ■ $\boldsymbol{k=4}$
O_2^{n-} ■ $\boldsymbol{l=1}$	1	0.25	0.25	0.43
HOO ■ $\boldsymbol{l=2}$	4.00	1	1	1.70
HO ■ $\boldsymbol{l=3}$	4.00	1	1	1.70
O^{n-} ■ $\boldsymbol{l=4}$	2.35	0.59	0.59	1

*For N=29, critical F= 0.47 and F=2.13 (at 95% significance level, α=0.050).

In this case, the null hypothesis (H_0), stating negligible differences between the variances of the model, is rejected when:

$$F < F_{1-\frac{\alpha}{2},N_k-1,N_l-1} = 0.47$$

and

$$F > F_{\frac{\alpha}{2},N_k-1,N_l-1} = 2.13$$

$F_{1-\frac{\alpha}{2},N_k-1,N_l-1}$ and $F_{\frac{\alpha}{2},N_k-1,N_l-1}$ were taken from F test distribution tables at a significance level of $\alpha = 0.050$, for $N_k = N_l = 29$.

The figure below shows schematically the F-statistic comparing the variances for the O_2^{n-} (k=1) and O^{n-} (l=4) models in **Table S14** resulting in an F = 2.35. If this value falls in the green region, the hypothesis is accepted, that there are no statistically significant differences between the models at the 95% confidence level ($\alpha = 0.050$). If the value falls in the light red area, the hypothesis is rejected and the differences between the models are statistically significant. Here, these two models' variances are statistically different. The figure was created with the online calculator at: https://www.statskingdom.com/220VarF2.html. Additional information on this and other tests can be found at: https://www.itl.nist.gov/div898/handbook/eda/section3/eda359.htm

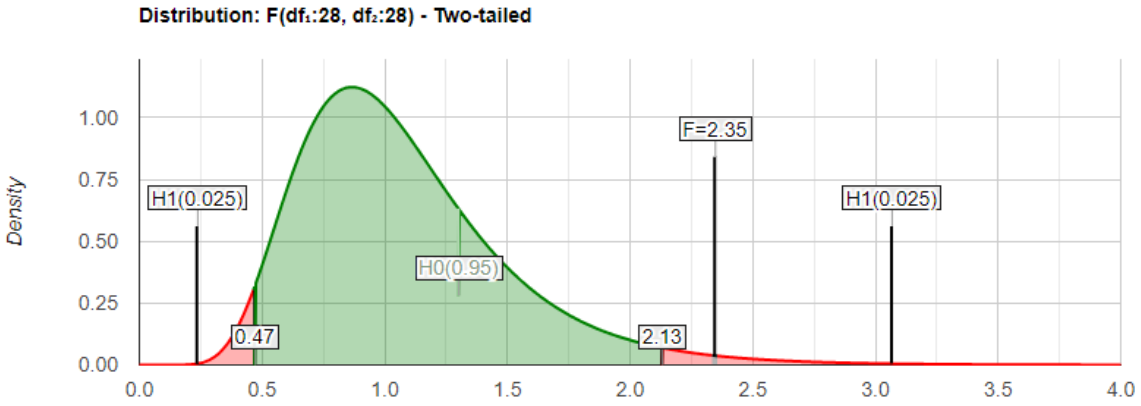

As reported above, the F-statistic calculated when comparing the variance of the model for $O_2{}^{n-}$■ with respect to HOO■, HO■, and O^{n-}■ fell out of the acceptance (green) region (0.47<F-statistic<2.13), indicating that the difference in the variance of the compared models is statistically significant. Hence, the low R^2 determined for model $O_2{}^{n-}$■ accurately represent the poor linear fitting of this model and it is statistically different when compared to rest of the models, which represent the data more accurately.

Conversely, the variances of the HOO■, HO■, and O^{n-}■ models are not statistically different, confirming the high degree of fitting of these models.

Table S15. Summary of relative MS (electron ionization) fragments (m/z) and their relative intensities for relevant species during ethanol oxidation.

		Relative Intensity of m/z																															
m/z	**FW**	**2**	**4**	**12**	**13**	**14**	**15**	**16**	**17**	**18**	**19**	**20**	**21**	**24**	**25**	**26**	**27**	**28**	**29**	**31**	**32**	**39**	**40**	**41**	**42**	**43**	**44**	**45**	**46**	**47**	**60**	**61**	**70**
H_2	2	100																															
He	4		100																														
H_2O	18							1	21	100	1																						
O_2	32							22													100												
Ar	40											15											100										
AcH	44			2	5	12	38	8	1	2	1		1	2	4	8	6	6	100	1			2	8	15	50	83	3					
EtOH	46			1	3	3	8		2	2	5			2	5	10	22	5	30	100				2	6	12	1	52	22	1				
AcOH	60			1	3	6	18							1	1	1	1	6	10	4			2	5	15	100	3	92	2	1	76	3	
EtOAc	88						8										8		14	2		1	1	1	6	100	4	16	2			16	12

Table S16. Ethanol conversion (main experiment and replicate) for in situ UV-Vis experiments in reaction cell for ethanol oxidation on commercial Au/TiO_2 at 1.5 kPa of O_2, 1 kPa of Ethanol, 240 ℃. Gas phase analysis via online mass spectrometry.

P_{O_2}(kPa)	P_{EtOH}(kPa)	Ethanol Conversion (%)
1.5	1	9.7
1.5	1	9.8

Table S17. Ethanol conversion and product selectivity measured in the in sit UV-Vis cell for ethanol oxidation on commercial Au/TiO_2 at 1.5 kPa of O_2, 1 kPa of Ethanol, 240 ℃. Gas phase analysis via online gas chromatography.

P_{O_2}(kPa)	P_{EtOH}(kPa)	Ethanol Conversion (%)	S_{AcH} (%)	S_{AcOH} (%)	S_{EtOAc} (%)	S_{others} (%)
1.5	1	7.0	86.9	5.0	5.6	2.4
1.5	1	7.3	87.5	4.8	4.9	2.7

Table S18. Ethanol conversion and product selectivity for fixed-bed reactor experiments for ethanol oxidation on commercial Au/TiO_2 at 1.5 kPa of O_2, 1 kPa of Ethanol, 240 ℃.

P_{O_2}(kPa)	P_{EtOH}(kPa)	Ethanol Conversion (%)	S_{AcH} (%)	S_{AcOH} (%)	S_{EtOAc} (%)	S_{others} (%)
1.5	1	7.5	93.6	2.9	3.5	0.0
1.5	1	7.6	93.6	3.0	3.5	0.0

Tables S16, S17 and **S18** show the conversion of ethanol in the in situ UV-Vis reaction cell and fixed bed reactor at reaction conditions. The results show that the gas analysis by MS was in agreement with gas analysis by GC and with fixed-bed reactor experiments performed at identical reaction conditions. Please refer to **Section S4** and **S5** for further details on the online GC analysis and the fixed bed reactor experimental procedure. The selectivity results show that the main product is acetaldehyde (>87%). Other partially oxygenated products were found with small selectivities including acetic acid (<5%) and ethyl acetate (<5%), whereas CO_2 was present in negligible amounts. It is worth mentioning that the bare TiO_2 support had negligible conversion at similar reaction conditions.

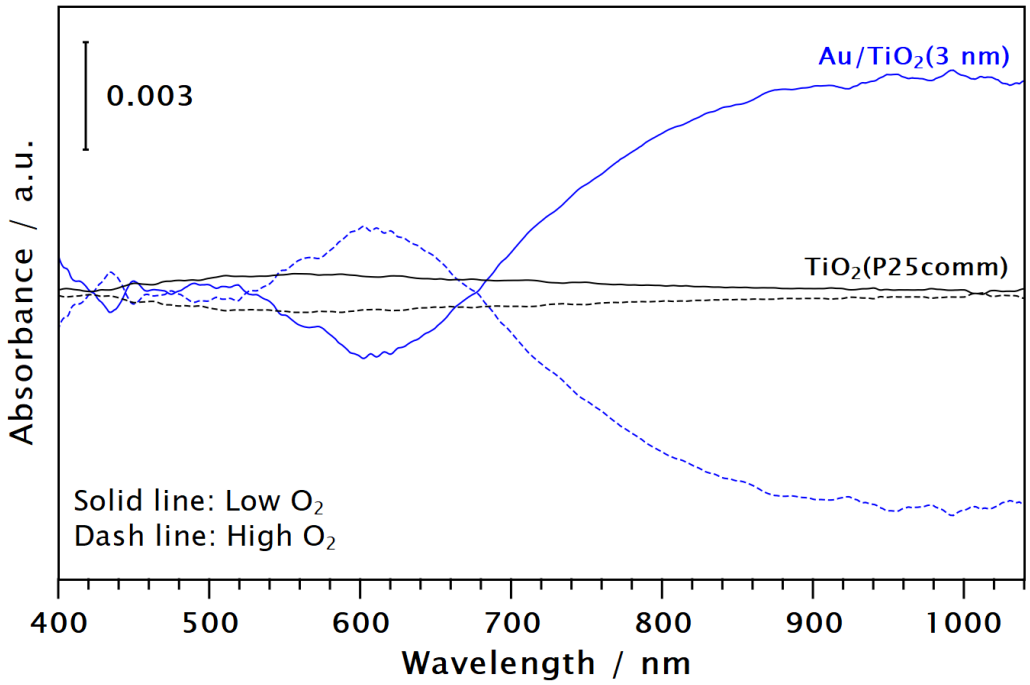

Figure S1. Phase domain trace plot of O_2 ME-PSD-DR-UV-Vis during EtOH oxidation at 240 ºC with PSD at the fundamental frequency. It shows negligible absorbance changes in the d-d transition region for the support (commercial TiO_2 P25) in comparison to the catalyst (Au/TiO_2). The traces at high/low O_2 are shown. Modulation frequency: 1/90 Hz, He + EtOH (1kPa) → He + EtOH(1kPa) + O_2(1.5kPa).

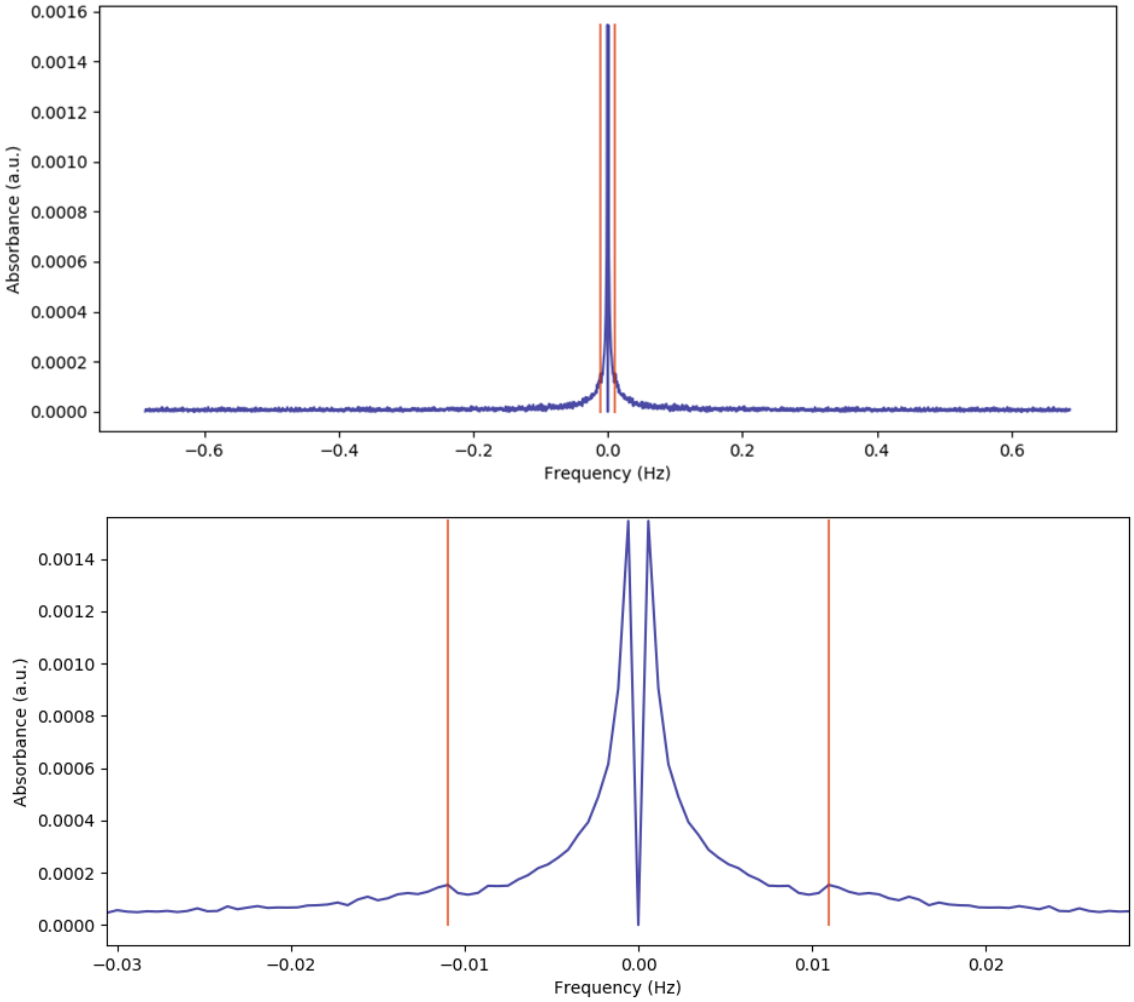

Figure S2. Frequency domain plot for O_2 ME-PSD-DR-UV-Vis experiment during EtOH oxidation at 240 ºC on TiO_2. Top: frequency domain wide range. Bottom: zoomed frequency plot at 900 nm showing the fundamental frequency absorbance intensity (1/90 Hz = 0.0111 Hz) just barely above the baseline noise level. The response at frequency 0 Hz was removed from the graph for easy plotting.

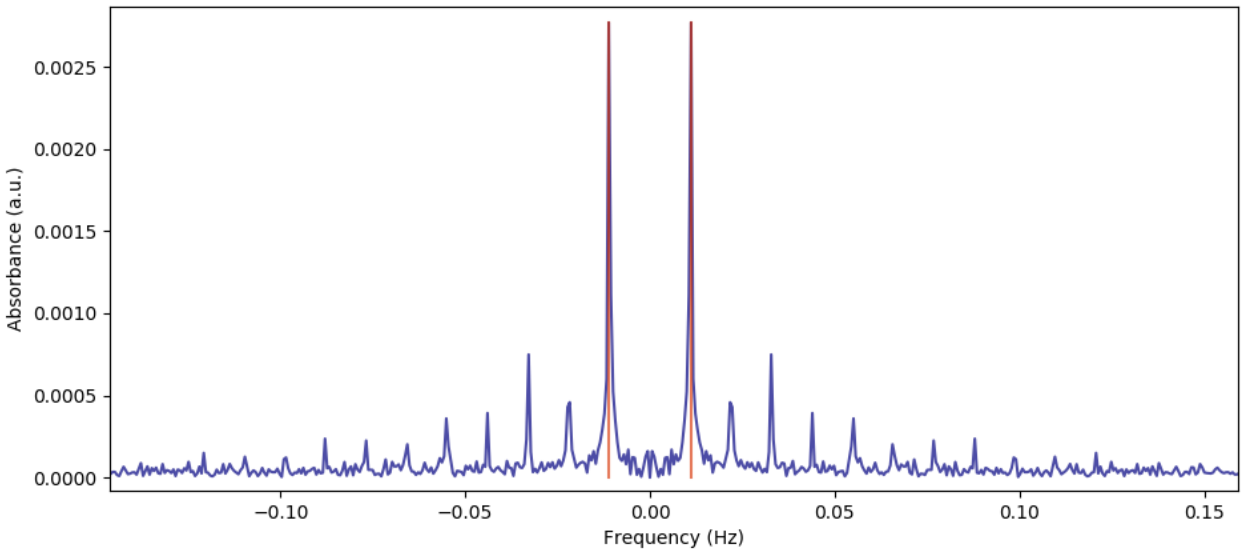

Figure S3. Frequency domain plot at 900 nm for O_2 ME-PSD-DR-UV-Vis experiment during EtOH oxidation at 240 ºC on Au/TiO_2. It shows the fundamental frequency (1/90 Hz = 0.0111 Hz) absorbance intensity well above the baseline noise level. The response at frequency 0 Hz was removed from the graph for easy plotting.

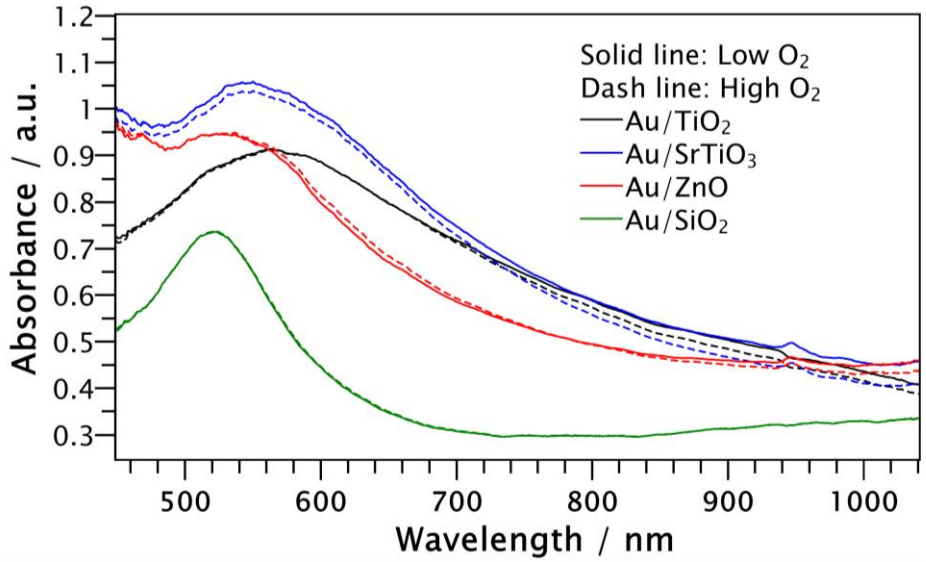

Figure S4. Time domain ME-UV-vis spectra for gold catalysts during O_2 modulation under ethanol oxidation at 398 K (240 °C). Conditions: 1/90 Hz, EtOH 1 kPa, with O_2 switches between 0-1.5 kPa.

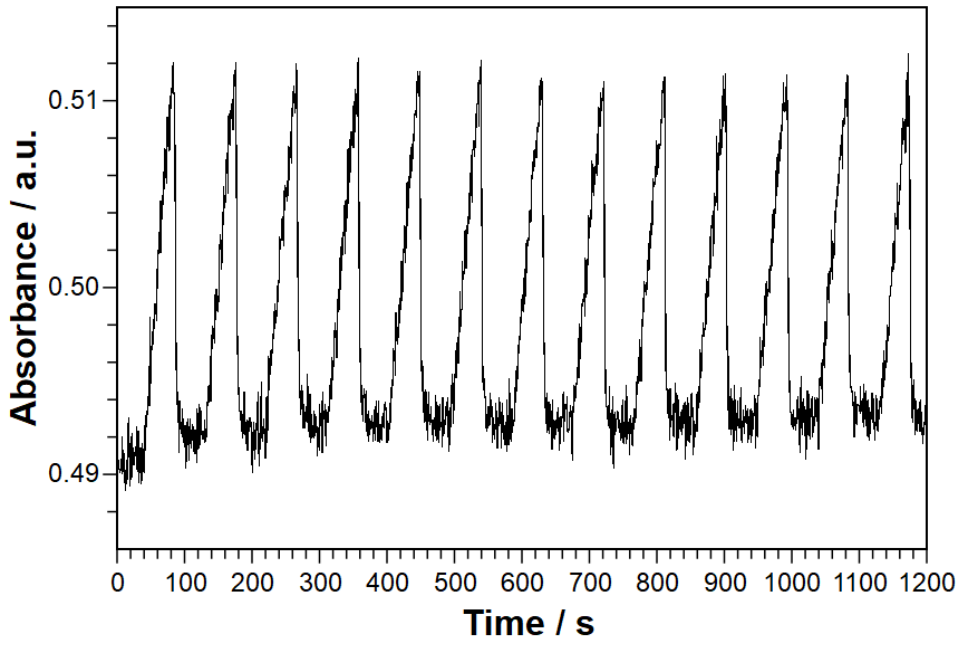

Figure S5. Time domain absorbance response at a wavelength of 900 nm related to charge transfer during O_2 ME-PSD-DR-UV-Vis on Au/TiO_2. Reaction conditions: 240 ºC, modulation frequency of 1/90 Hz, He + EtOH (1kPa) → He + EtOH(1kPa) + O_2(1.5kPa).

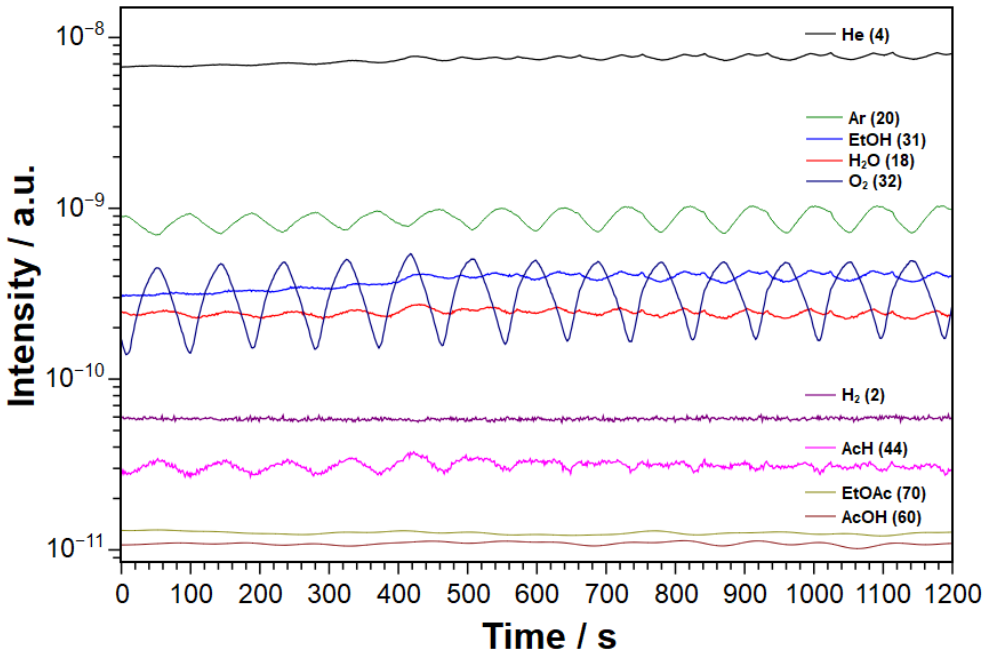

Figure S6. MS response during O_2 modulation in EtOH oxidation on Au(3 nm)/TiO_2. Reaction conditions: 240 ºC, modulation frequency of 1/90 Hz, He + EtOH (1kPa) → He + EtOH(1kPa) + O_2(1.5kPa).

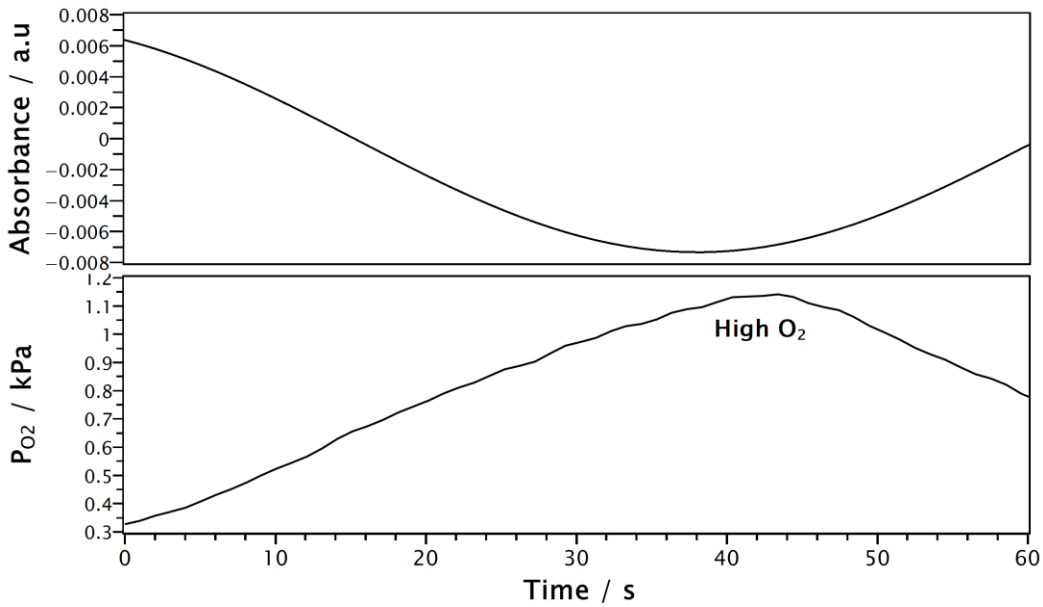

Figure S7. Top: phase domain trace plot for CT absorbance of O_2 ME-PSD-DR-UV-Vis on Au/TiO_2 (at 900 nm). Bottom: phase domain trace plot of O_2 partial pressure from MS. PSD applied at the fundamental frequency of 1/90 Hz.

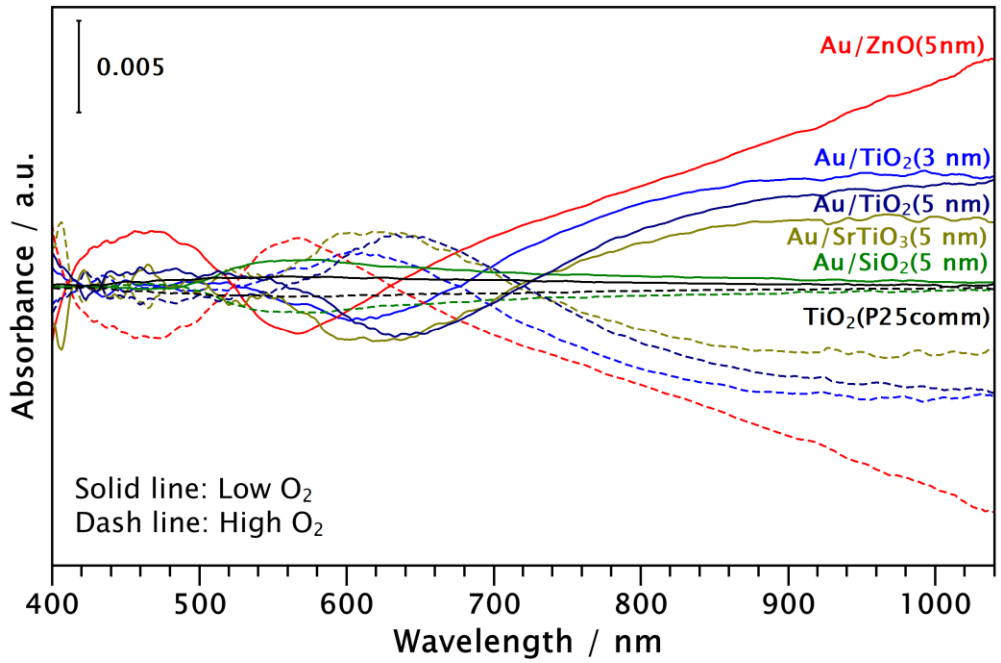

Figure S8. Phase domain trace plot of O_2 ME-PSD-DR-UV-Vis during EtOH oxidation on Au/TiO_2 with PSD at the fundamental frequency. The spectra show charge transfer to/from support in the vicinity of Au at 800-1000 nm. The traces for all catalysts are shown at high/low O_2. Reaction conditions: 240 ºC, modulation frequency of 1/90 Hz, He + EtOH (1kPa) → He + EtOH(1kPa) + O_2(1.5kPa).

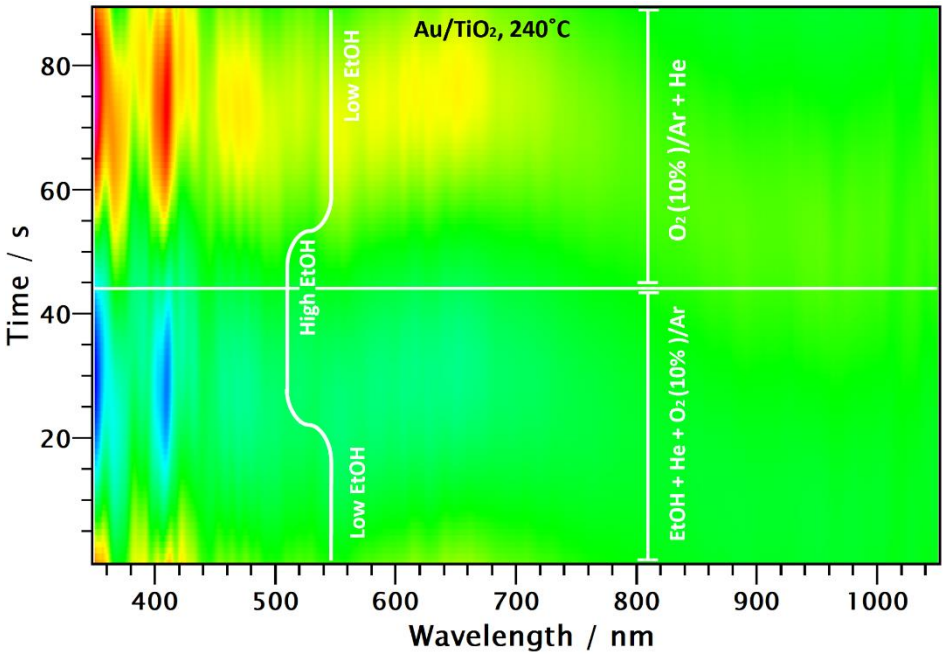

Figure S9. Phase domain contour plot of ME-DR-UV-Vis ethanol modulation during the oxidation of ethanol on Au/TiO_2 with PSD at the fundamental frequency. Conditions: EtOH modulation frequency of 1/90 Hz, O_2 1.5 kPa, 240˚C.

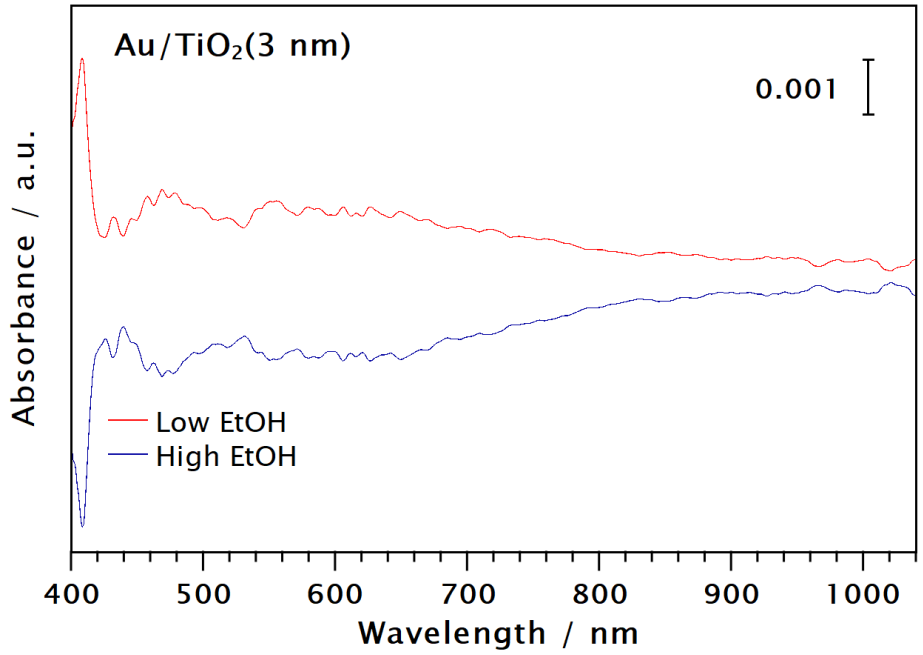

Figure S10. Phase domain trace plot at lowest and highest EtOH concentrations for ME-DR-UV-Vis during ethanol oxidation on Au/TiO_2 with PSD at the fundamental frequency. EtOH modulation frequency of 1/90 Hz, O_2 1.5 kPa, 240˚C.

Figure S11A: Au/TiO_2 steady state runs

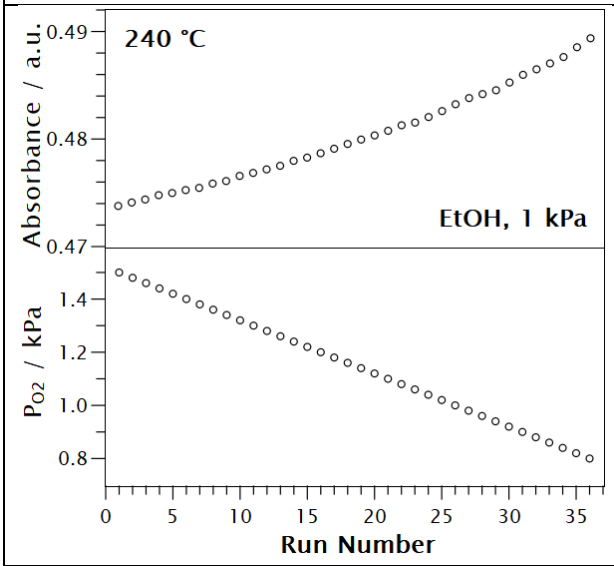

Figure S11B: TiO_2 steady state runs

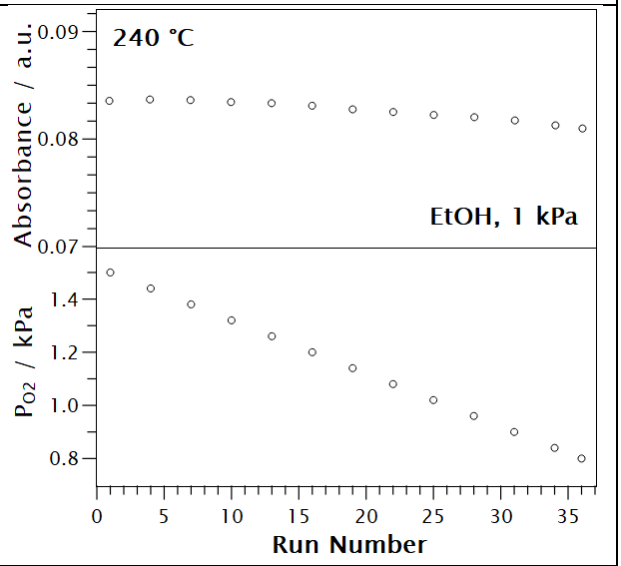

Figure S11. Steady state in situ absorbance (at 900 nm) vs O_2 partial pressures during ethanol oxidation at 523 K (240 °C) on: A) commercial Au/TiO_2 and B) on TiO_2 (P25).

S7. A Primer on UV-Visible Modulation Excitation Spectroscopy.

S7.1. Understanding the Time Domain, Frequency Domain, and Phase Domain Results

S7.1.1. Modulation Experiment (see **Section 2.5.1** in the main text). The in situ system is given in **Figure 1**.

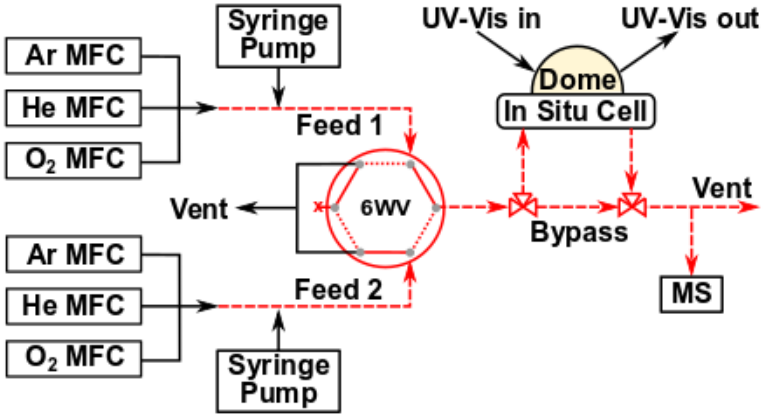

Figure 1. Schematic representation of the in situ/operando ME-UV-Vis spectroscopic system [5].

S7.1.2. Time Domain Results. In a typical experiment for O_2 modulation (see **Section 2.5.1** in the main text) the feed to the in situ cell is switched periodically (the 6WV in **Figure 1** is switched ON and OFF) between Feed 1: containing He + EtOH (1kPa) and Feed 2: containing He + EtOH(1kPa) + O_2(1.5kPa) every 45 seconds. This results in a period of 90 seconds during which O_2 concentrations are varied inside the in situ cell. Typically, over 15 periods are performed in a single experiment.

a. **Data synchronization. Figure S6** shows the changes in O_2 concentrations in an O_2 modulation experiment. Please see References [6] and [7] to note that the concentrations measured in the MS are not synchronized with the spectroscopic data. The reason for this is the mixing in the reaction cell, transport lines, and MS chamber which cause a delay in the time for actual MS data sampling. For kinetic studies from modulation experiments, the concentrations in the cell need to be measured directly in the vicinity of the catalyst (and not by MS, unless its mixing chamber is minimal) or calculated using mixing models [5-7].

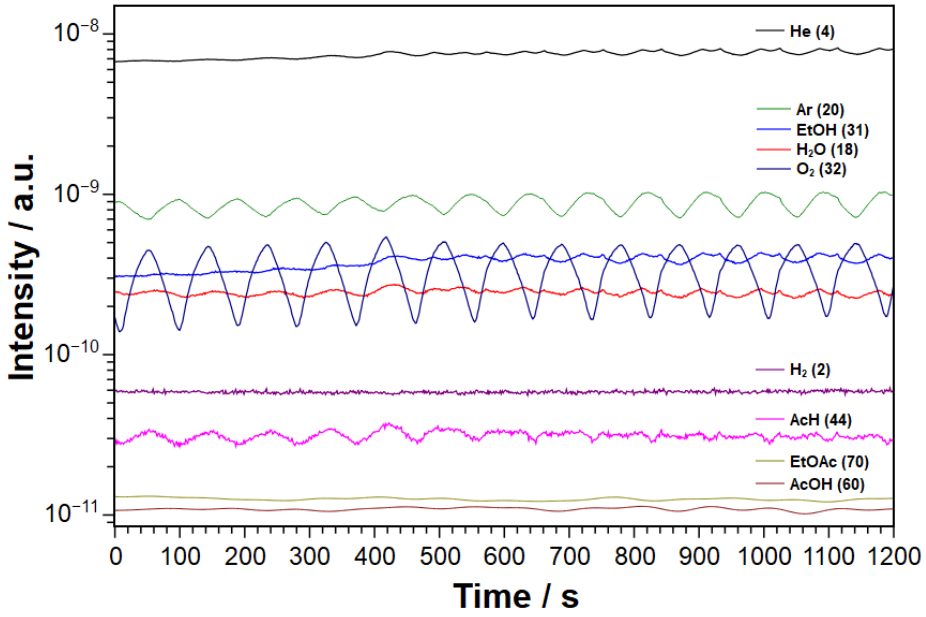

Figure S6. MS response during O_2 modulation in EtOH oxidation on Au(3 nm)/TiO_2. Reaction conditions: 240 ºC, modulation frequency of 1/90 Hz, He + EtOH (1kPa) → He + EtOH(1kPa) + O_2(1.5kPa).

b. **Actual Cell Concentrations**. Also note that the O_2 concentrations at which the catalyst is exposed during modulation (inside the cell) are not necessarily changing exactly between 0 and 1.5 kPa (the two feed concentrations at the 6WV) during modulation. The actual concentrations will depend on the mixing of reactants and residence time in the in situ cell, which are determined by the reactants nature, gas flow rates, and cell dead volume [5-7]. For our current conditions, we calculated O_2 concentrations varying between ~0.3 and 1.4 kPa.

c. **Maximum change in Absorbance During MES**. UV-Vis spectra are collected approximately every second. This results in a total of over ~90 x 15 = 1350 UV-Vis spectra per experiment. The black solid and dashed lines in **Figure S4** correspond to only two spectra for the Au/TiO_2 catalyst. The dash line corresponds to a point where O_2 concentration is the highest in the cell and the solid line corresponds to a point where O_2 concentration is the lowest.

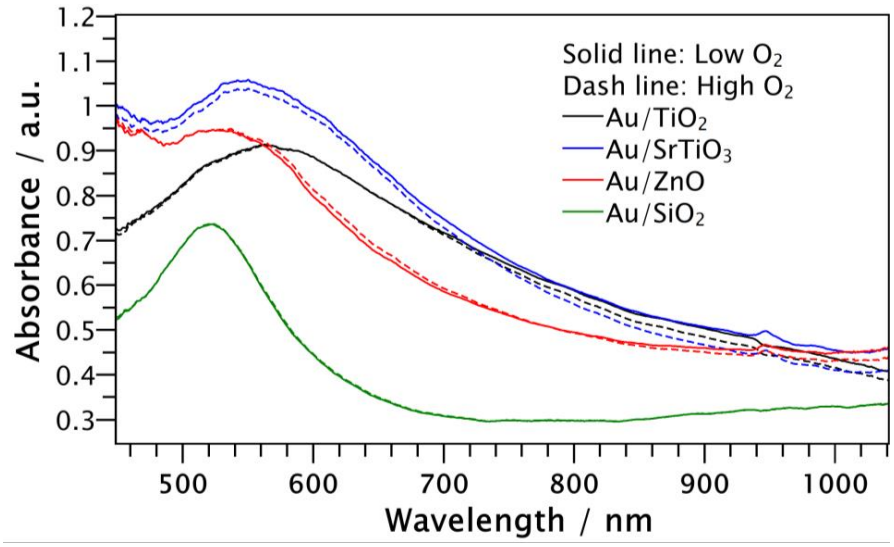

Figure S4. Time domain ME-UV-vis spectra for gold catalysts during O_2 modulation under ethanol oxidation at 398 K (240 °C). Conditions: 1/90 Hz, EtOH 1 kPa, with O_2 switches between 0-1.5 kPa.

d. **Time Domain Modulations.** If we only record the absorbance changes at 900 nm, the spectrum in **Figure S5** is obtained. Note that the absorbance increases at low O_2 concentrations and decreases at high O_2 concentrations. In **Figure S5**, the lowest O_2 concentration corresponds to the highest points, whereas the highest O_2 concentration corresponds to the lowest points.

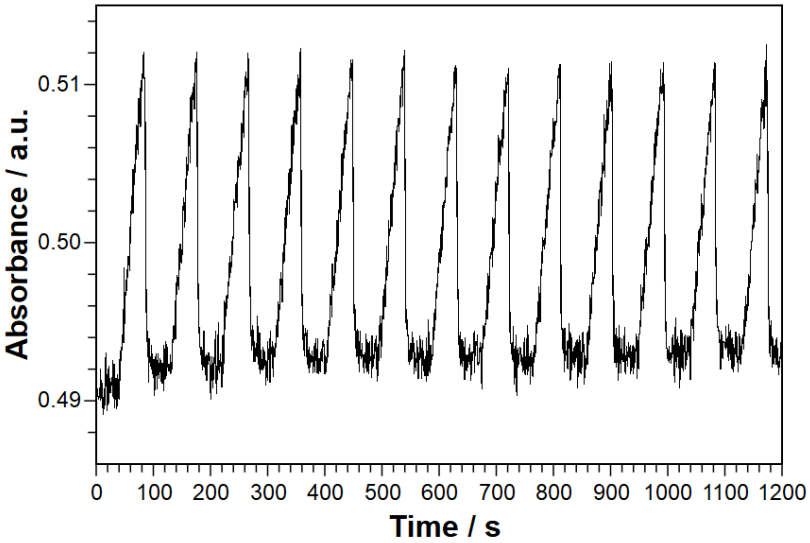

Figure S5. Time domain absorbance response at a wavelength of 900 nm related to charge transfer during O_2 ME-PSD-DR-UV-Vis on Au/TiO_2. Reaction conditions: 240 ^oC, modulation frequency of 1/90 Hz, He + EtOH (1kPa) → He + EtOH(1kPa) + O_2(1.5kPa).

e. **Time domain Absorbance Response to O_2 Modulation at 570 nm**. Not every wavelength in the UV-Vis spectrum behaves as that in **Figure S5**. This will only happen if the signal responds to O_2 modulation. **Figures S12A** and **S12B** show a typical time domain UV-Vis spectra for Au/TiO_2 and TiO_2, respectively, at reaction conditions during O_2 modulation. The time domain absorbance response at 570 nm (plasmon maximum) for Au/TiO_2 and TiO_2 are shown in **Figures 12C** and **12D**, respectively. The results indicate a weak and barely visible periodic response at 570 nm relative to the baseline noise.

S12A: Au/TiO_2 Time Domain Spectra (570 nm Selected)

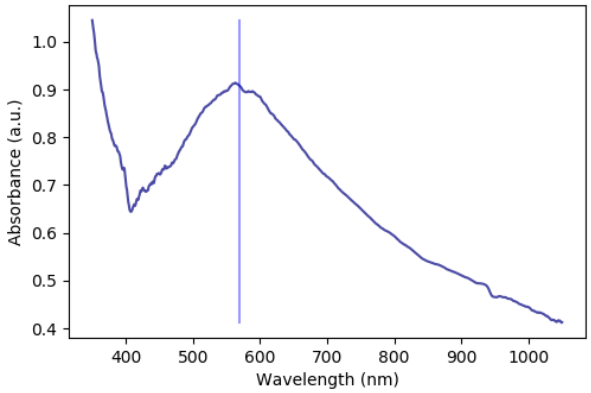

S12B: TiO_2 Time Domain Spectra (570 nm Selected)

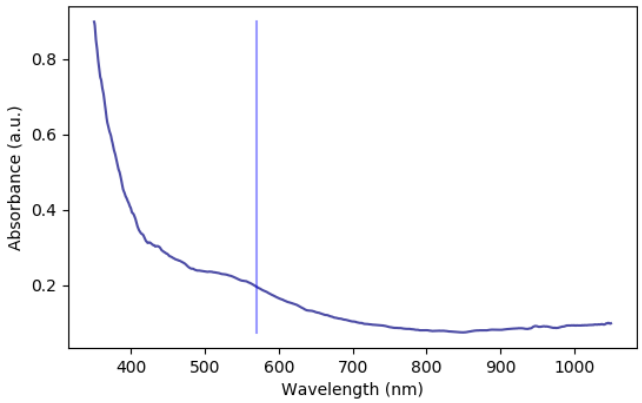

S12C: Au/TiO_2 570 nm Time Domain Response

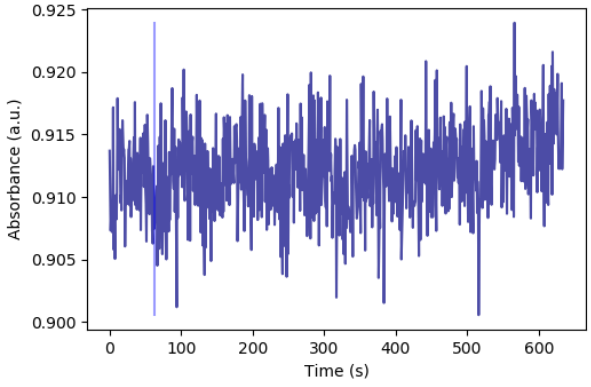

S12D: TiO_2 570 nm Time Domain Response

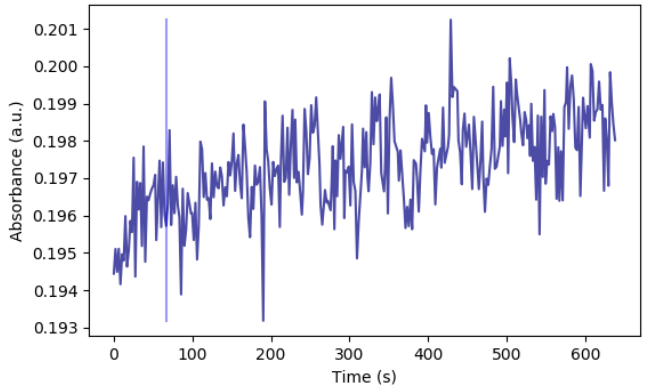

Figure S12. A, B) Typical time domain UV-Vis spectra (~90 s) with wavelength selected at 570 nm during O_2 ME-PSD-DR-UV-Vis on Au/TiO_2 and TiO_2, respectively. C, D) Time domain absorbance response for 570 nm during O_2 ME-PSD-DR-UV-Vis on Au/TiO_2 and TiO_2, respectively. Reaction conditions: 240 ºC, modulation frequency of 1/90 Hz, He + EtOH (1kPa) → He + EtOH(1kPa) + O_2(1.5kPa).

f. **Time Domain Absorbance Response to O_2 Modulation at 900 nm**. **Figures 13A** and **13B** show a typical time domain UV-Vis spectra for Au/TiO_2 and TiO_2, respectively, during O_2 modulation with 900 nm wavelength selected. The corresponding time

domain absorbance response at 900 nm is shown in **Figures S13C** and **S13D** for Au/TiO_2 and TiO_2, respectively. The results show that the time domain absorbance for Au/TiO_2 responds to O_2 modulation over a relatively wide range of absorbances. On the other hand, the absorbance at 900 nm for TiO_2 responds but only weakly. Note that the scales for Au/TiO_2 and TiO_2 absorbances are different. Moreover, the time domain average relative absorbance for TiO_2 (~0.081) is only a small fraction of that for Au/TiO_2 (~15%).

S13A: Au/TiO_2 Time Domain Spectra (900 nm Selected)

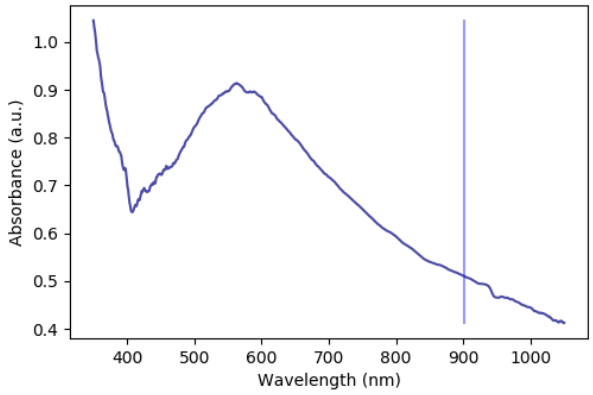

S13B: TiO_2 Time Domain Spectra (900 nm Selected)

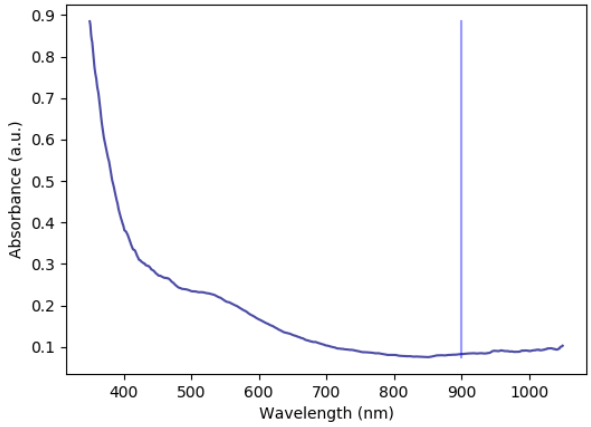

S13C: Au/TiO_2 900 nm Time Domain Response

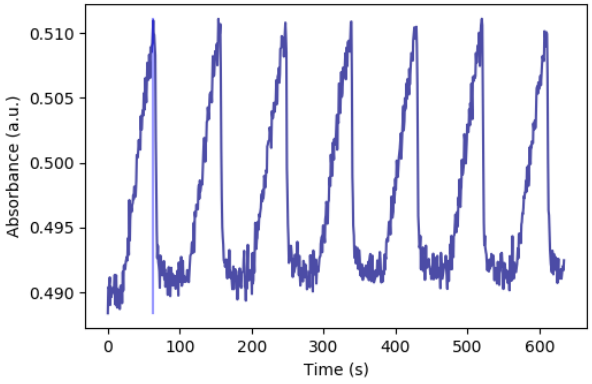

S13D: TiO_2 900 nm Time Domain Response

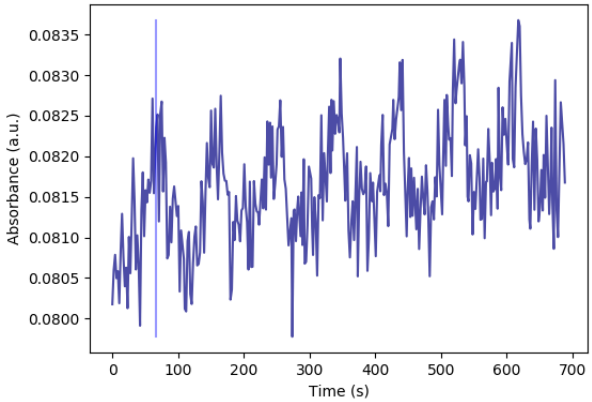

Figure S13. A, B) Typical time domain UV-Vis spectra (~90 s) with Wavelength selected at 900 nm during O_2 ME-PSD-DR-UV-Vis on Au/TiO_2 and TiO_2, respectively. C, D) Time domain absorbance response for 900 nm during O_2 ME-PSD-DR-UV-Vis on Au/TiO_2 and TiO_2, respectively. Reaction conditions: 240 ºC, modulation frequency of 1/90 Hz, He + EtOH (1kPa) → He + EtOH(1kPa) + O_2(1.5kPa).

S7.1.3. Frequency and Phase Domain Results

a. **Phase Domain Contour Plots.** Upon PSD analysis of the time domain data in **Figures S12** and **S13** and frequency filtering (at the fundamental frequency of 1/90 s = 0.0111 Hz),

data is obtained in the phase domain. This is shown in the contour plots in **Figure S14** for Au/TiO_2 and TiO_2, respectively. Note that the y axis in these figures could also be expressed in units of time (based on a period) recalling that the experimental period is 90 seconds (or 360 degrees). The contour plots are handy because they allow to quickly visualize regions with the highest and lowest absorbance response. Moreover, correlations between different wavelengths can also be noted relatively quickly.

S14A: Au/TiO_2 Phase Domain – Contour Plot **S14B**: TiO_2 Phase Domain – Contour Plot

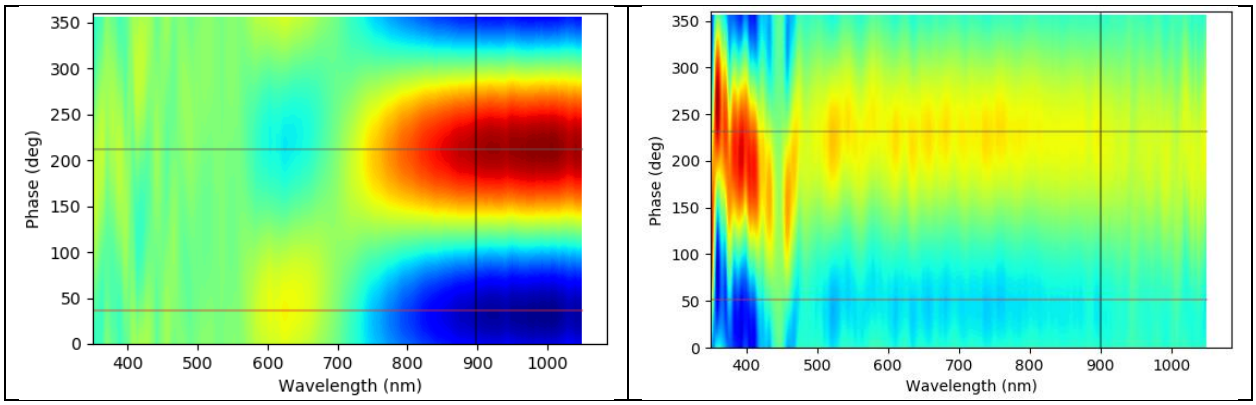

Figure S14. Phase domain contour plots upon application of PSD at the fundamental frequency during O_2 ME-PSD-DR-UV-Vis on A) Au/TiO_2 and B) TiO_2. Analysis performed only on the modulations in **Figure S12** and **S13**. Reaction conditions: 240 ºC, modulation frequency of 1/90 Hz, He + EtOH (1kPa) → He + EtOH(1kPa) + O_2(1.5kPa).

b. **Phase Domain Trace Plots and Frequency Domain Plots.** Phase Domain trace plots can be seen in **Figures S15A, S15B, S16A** and **S16B**. For simplicity, these figures only show the traces for the maximum (lowest O_2) and minimum (highest O_2) absorbance (see horizontal lines in **Figure S14**).

Response at 570 nm. The green vertical lines in **Figures S15A** and **S15B** show the selection of a single wavelength at 570 nm (Au plasmon peak position). The trace plots show that the absorbance changes at 570 nm are minimal. The corresponding frequency domain **Figures S15C** and **S15D** lack a visible fundamental frequency (0.0111 Hz) with a magnitude above the baseline noise. This indicates that the absorbance around the plasmon peak does not respond significantly to O_2 modulation.

S15A: Au/TiO_2 Phase Domain – Trace Plot

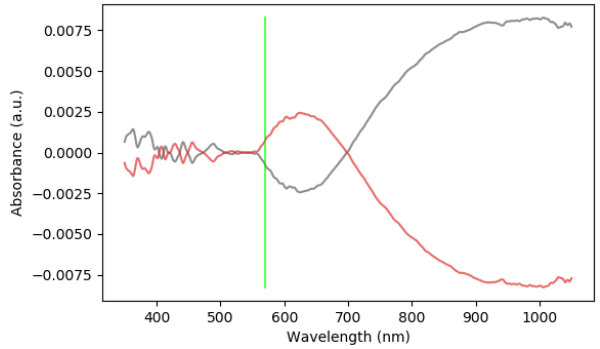

S15B: TiO_2 Phase Domain – Trace Plot

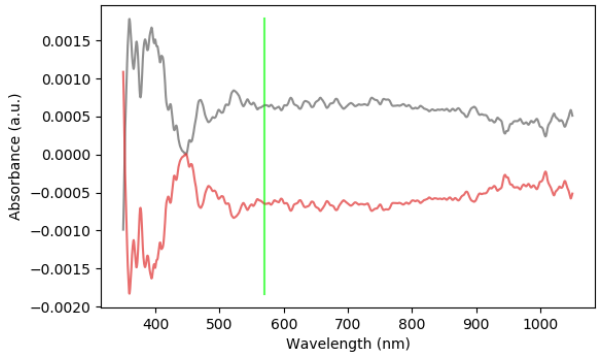

S15C: Au/TiO_2 Frequency Domain @ 570 nm

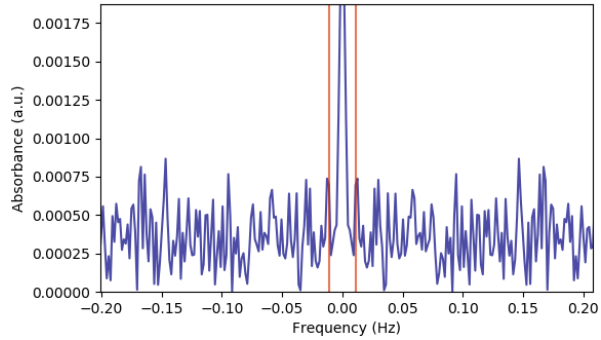

S15D: TiO_2 Frequency Domain @ 570 nm

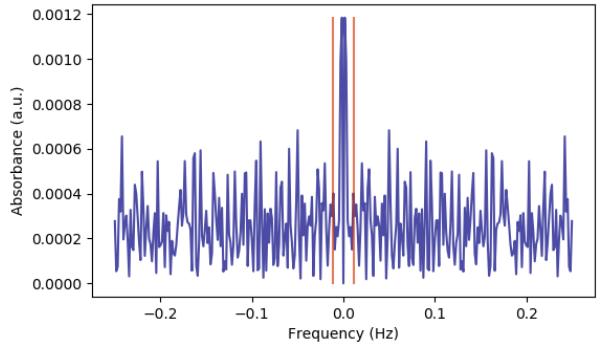

Figure S15. A, B) Phase domain trace plots with PSD at the fundamental frequency during O_2 ME-PSD-DR-UV-Vis on Au/TiO_2 and TiO_2, respectively. For clarity, only the highest and lowest absorbance traces are shown. C, D) Frequency domain plots evaluated at 570 nm for Au/TiO_2 and TiO_2, respectively. The vertical red lines were added to note the position of the fundamental frequency. Analysis performed only on the modulations in **Figures S12** and **S13**. Reaction conditions: 240 °C, modulation frequency of 1/90 Hz, He + EtOH (1kPa) → He + EtOH (1kPa) + O_2 (1.5kPa).

Response at 900 nm. Figures S16A and **S16B** show the phase domain trace plots with the 900 nm wavelength selected for Au/TiO_2 and TiO_2, respectively. It can be noted that the 900 nm d-d transition region for the Au/TiO_2 catalyst responds to O_2 modulation with a high change in absorbance values. The corresponding phase domain absorbance change for the TiO_2 support (~0.0004) is small and it only corresponds to a fraction (<6%) of the phase domain absorbance change for Au/TiO_2. **Figures S16C** and **S16D** show the frequency domain plots evaluated at 900 nm for Au/TiO_2 and TiO_2, respectively. For Au/TiO_2 (**Figure S16C**), the presence of a strong fundamental frequency (0.0111 Hz) and of even and odd harmonics (e.g., 0.0222, 0.0333, 0.0444 Hz, etc) confirm the periodic change of the 900 nm wavelength during O_2 modulation with a sawtooth-like response (see **Figure S13** and Table 1 in Ref. [5]). The corresponding frequency domain for the 900 nm d-d transition region in the TiO_2 support (**Figure S16D**) shows a fundamental frequency whose magnitude is just slightly above the noise level. This indicates that the TiO_2 support absorbance at 900

nm undergoes only a small change upon O_2 modulation at reaction conditions (and fundamental frequency).

S16A: Au/TiO_2 Phase Domain – Trace Plot

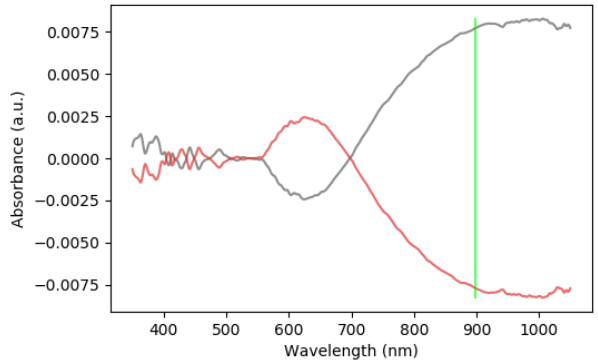

S16B: TiO_2 Phase Domain – Trace Plot

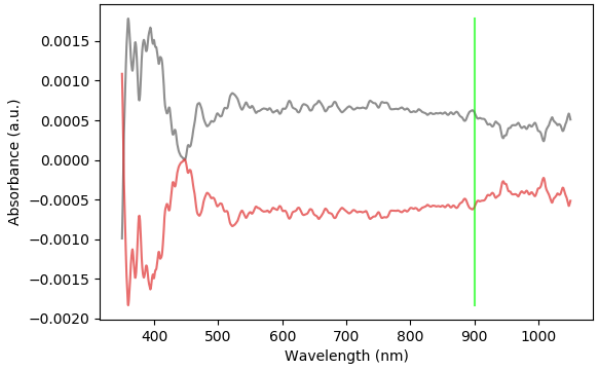

S16C: Au/TiO_2 Frequency Domain @ 900 nm

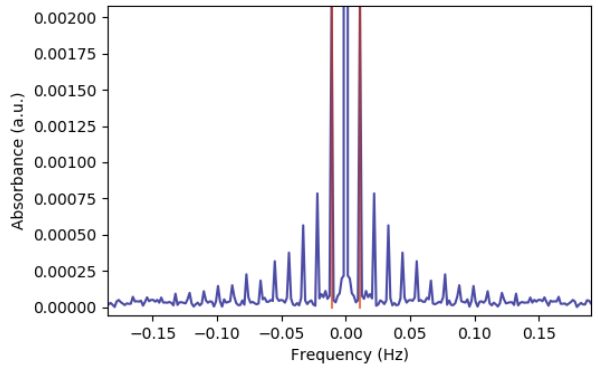

S16D: TiO_2 Frequency Domain @ 900 nm

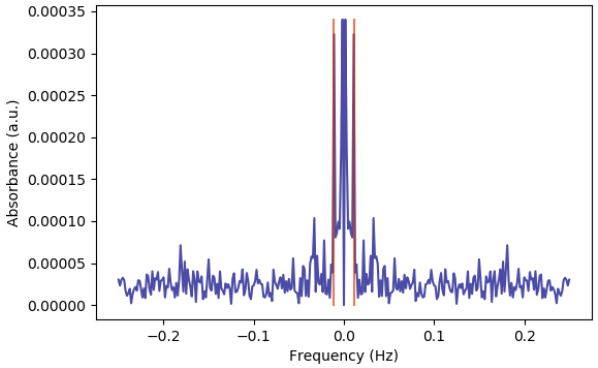

Figure S16. A, B) Phase domain trace plots filtered at the fundamental frequency during O_2 ME-PSD-DR-UV-Vis on Au/TiO_2 and TiO_2, respectively. For clarity, only the highest and lowest absorbance traces are shown. C, D) Frequency domain plots evaluated at 900 nm Au/TiO_2 and TiO_2, respectively. The vertical red lines were added to note the position of the fundamental frequency. Analysis performed only on the modulations in **Figures S12** and **S13**. Reaction conditions: 240 ºC, modulation frequency of 1/90 Hz, He + EtOH (1kPa) → He + EtOH (1kPa) + O_2 (1.5kPa).

S7.2. The Issue of Background Contributions to in Situ/Operando Spectra

In many instances, in situ/operando spectroscopic results for supported catalysts include contributions from both the support and the supported metal (or metal oxide) of interest and/or the gas phase reactants. If required, those contributions can be removed. The conventional and most sensible approach for steady-state data is the use of a difference spectra procedure by employing blank runs with the supports or reference samples exposed to the same reaction conditions. This is most commonly performed in separate experiments. Although an in situ cell could be designed for a dual sample collection chamber such that both the catalyst and support spectra can be collected in the same experiment. An example of such in situ cell is available commercially for DRIFTS measurements (e.g., Thermo Dual Sample Environmental Chamber, Smart Collector, P/N 0031-902).

In the present case for UV-Vis spectra, we performed identical O_2 modulation experiments (in different runs) on Au/TiO_2 and the TiO_2 support to determine possible support contributions to the Au/TiO_2 spectra. More specifically, we were interested in support contributions to the d-d transition absorbance change, a proxy for charge transfer. A summary of the results @ 900 nm wavelength (d-d transition region) was shown in the previous sections and a list of the figures is summarized next:

a. Au/TiO_2 Time Domain ME-UV-Vis sample spectra: **Figures S13A** and **7**
b. TiO_2 Time domain ME-UV-Vis sample spectra: **Figure S13B**
c. Au/TiO_2 Time Domain absorbance modulation: **Figure S13C** and **S5**
d. TiO_2 Time Domain absorbance modulation: **Figure S13D**
e. Au/TiO_2 Phase Domain contour plot: **Figures S14A** and **9**
f. TiO_2 Phase Domain contour plot: **Figure S14B**
g. Au/TiO_2 Phase Domain trace plot (showing maximum and minimum absorbance conditions): **Figure S16A** and **8**
h. TiO_2 Phase Domain trace plot (showing maximum and minimum absorbance conditions): **Figure S16B**
i. Combined Au/TiO_2 and TiO_2 Phase Domain trace plot: **Figure S1**
j. Au/TiO_2 Frequency Domain: **Figures S16C** and **S3**
k. TiO_2 Frequency Domain: **Figures S16D** and **S2**

In the present study, the above procedure of subtracting TiO_2 spectra from those of Au/TiO_2 at reaction conditions is justified since there are two possible regions of interest during reaction. The first one is the primary reaction zone (Au nanoparticle and TiO_2 in the vicinity of Au nanoparticle, i.e., near the Au-TiO_2 perimeter). The second one is an extended reaction zone (the TiO_2 support far beyond the location of the Au nanoparticle). In the present charge transfer study, the main interest is in the primary reaction zone, where O_2 is activated. If any reaction occurs in the extended reaction zone, a TiO_2 support charge transfer contribution would need to be subtracted from that measured in the Au/TiO_2 catalyst.

S7.2.1. Subtracting TiO_2 Background Contributions from the Au/TiO_2 Spectra

a. **Steady-State Time Domain Data Subtraction**. Note that this spectrokinetic study does not use MES absorbance data but rather steady-state spectroscopic experiments for kinetic models' discrimination. This choice was made for simplicity, because the MS (downstream the reaction cell) and UV-Vis (in the reaction cell) data are not synchronized to the time in the reaction cell. To use the present MES data, a "synchronization" procedure would be required. Such procedure consists in modelling the mixing of gases in the reaction cell, transfer lines, and MS inner chamber at all reaction conditions [5-7]. With this model and using the concentrations measured in the MS, the concentrations in the in situ cell could be back calculated.

   We avoided the use of mixing models by running steady-state experiments and holding the concentrations in the cell constant for steady MS measurements. In the present study, we

established different kinetic correlations between charge transfer and reaction conditions including concentrations and reaction rates. Here, absorbance changes in the d-d transition region were used as proxies for charge transfer in the derived kinetic models. MES data showed that the contribution of TiO_2 support to charge transfer changes was minimal:

i. **MES Phase Domain. Figures S1, S16A,** and **S16B** show that the contribution of TiO_2 support to Au/TiO_2 spectra in the d-d transition region is small. For example, if we were to apply a difference spectra procedure in the MES phase domain (at the fundamental frequency), the contribution of TiO_2 support to Au/TiO_2 d-d transition region would be about ~6% or less.

ii. **Time Domain. Figures S13C** and **S13D** show that the baseline absorbance of TiO_2 remains relatively constant during modulation. For a difference spectra procedure in the time domain, TiO_2 support contributes to approximately ~15% the absolute absorbance value of Au/TiO_2 in the d-d transition region.

In short, in the present case, subtracting or not subtracting TiO_2 from Au/TiO_2 absorbances at 900 nm in the time (or phase) domain would lead to similar spectra. More importantly, for the charge transfer kinetic analysis, similar (linear fits) trends are expected from Au/TiO_2 spectral data regardless of a subtraction procedure. When subtracting the TiO_2 baseline from Au/TiO_2 data, in the time domain at steady-state, the y axis representing the difference absorbance of "$Au/TiO_2 - TiO_2$" would simply displace all data equally to an absorbance value slightly smaller than that of the unreferenced Au/TiO_2. **Figure 11** in the main text (and presented below) shows the spectrokinetic analysis using the steady state data difference spectra procedure described above. For comparison, **Figure S17** shows the result for the uncorrected absorbance results on the Au/TiO_2 catalyst.

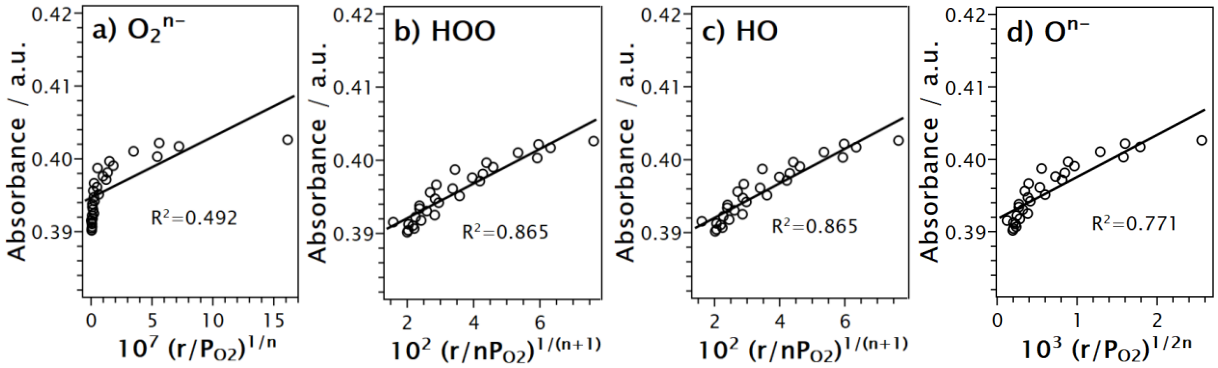

Figure 11. Correlation results for charge transfer models shown in **Table 1** for different oxygen species involved in ethanol oxidation on Au/TiO_2: a) O_2^{n-}, b) HOO, c) HO, and d) O^{n-}. The *x* axis corresponds to the $(r/P_{O2})^x$ term in the kinetic model, which varies depending on the oxygen species. The *y* axis corresponds to the Au/TiO_2 absorbance at 900 nm and at reaction conditions corrected for bare TiO_2 support contributions. The parameter n is the net charge transferred to the support in the rate limiting step as calculated from DFT (last column in **Table 1**).

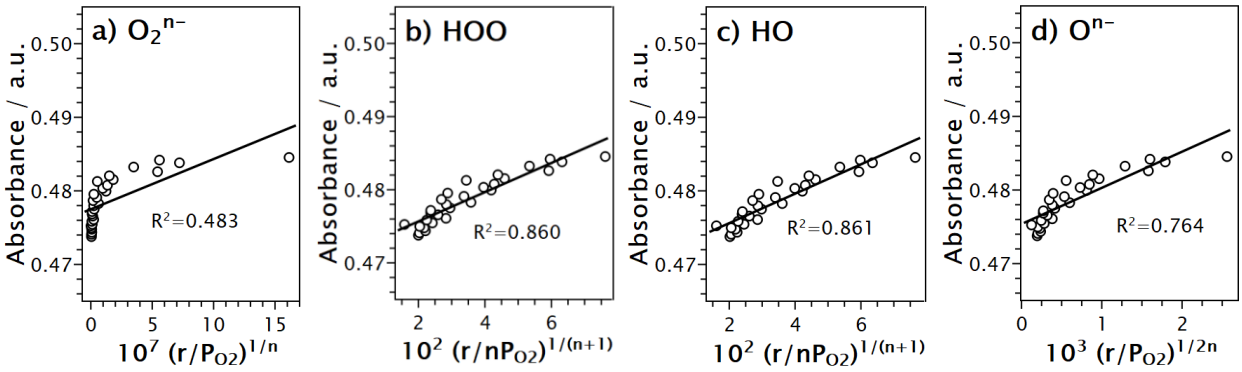

Figure S17. Correlation results for charge transfer models shown in **Table 1** for different oxygen species involved in ethanol oxidation on Au/TiO_2: a) O_2^{n-}, b) HOO, c) HO, and d) O^{n-}. The *x* axis corresponds to the $(r/P_{O2})^x$ term in the kinetic model, which varies depending on the oxygen species. The *y* axis corresponds to the uncorrected Au/TiO_2 absorbance at 900 nm and at reaction conditions. The parameter n is the net charge transferred to the support in the rate limiting step as calculated from DFT (last column in **Table 1**).

b. **Modulation Phase Domain Data Subtraction**. **Figures S1** and **S16B** showed the corresponding phase domain trace spectra for the highest (low O_2) and lowest (high O_2) absorbances for the TiO_2 support. It is clear that the absorbance at 900 nm does not respond significantly to the O_2 concentration modulation (at the fundamental frequency). This is evident in the frequency domain (**Figure S16D**) by the lack of a significantly large fundamental frequency above the baseline noise level. Moreover, for 900 nm the maximum change in absorbance during O_2 modulation (~0.0004) only corresponds to a fraction (~6%) of the maximum absorbance at 900 nm for the Au/TiO_2 results (at the frequency of 1/90 Hz). This indicates that the TiO_2 support contributions to the redox changes in the Au/TiO_2 are small. In other words, when applying the difference spectra procedure described above to MES data it will result in similar Au/TiO_2 spectra in the phase domain.

   There will be situations where the support can have a significant contribution to the charge transfer. In this event, when subtracting spectra of a reference sample from those of the catalyst, one needs to ensure that both experiments (e.g., catalyst and support) are synchronized (i.e., in phase) to avoid the addition of artifacts. This can be difficult to accomplish in the time domain, but it is more manageable in the frequency domain. Next, we provide a general procedure for how to subtract MES spectra of a reference sample in the frequency domain.

S7.2.2. General Difference Spectra Procedure for MES Data

Performing a difference spectra procedure, for example, between data of a catalyst (e.g., experiment 1) and a support (e.g., experiment 2) exposed to identical MES conditions, is often useful to remove potential support contributions. However, this is not trivial since data recording

in different experiments (even at the same experimental conditions) may not be precisely controlled to start at the same phase. This usually creates artifacts as:

$$A_1 \cos \omega t - A_2 \cos(\omega t + \Delta\phi) = A \cos(\omega t - \psi)$$

vs. the phase-corrected:

$$A_1 \cos \omega t - A_2 \cos \omega t = (A_1 - A_2) \cos \omega t.$$

Where

$$A = \sqrt{[A_1 - A_2 \cos \Delta\phi]^2 + [A_2 \sin \Delta\phi]^2}$$
$$\psi = \tan^{-1} [A_2 \sin \Delta\phi]/[A_1 - A_2 \cos \Delta\phi]$$

Let $A_1 - A_2 = \Delta A > 0$. The relative deviation

$$\frac{A_1 - A_2}{A} - 1 \approx -\frac{A_1 A_2}{2(A_1 - A_2)^2} (\Delta\phi)^2 + O[(\Delta\phi)^4]$$

indicates that the artifacts may be negligible when $A_1 \gg A_2$, but otherwise can be misleading even for a small phase difference $\Delta\phi$. For discrete periodic signals, phase correction can be challenging in the time domain since the time lag can be a fraction of the sampling period. Instead, it should be corrected by linearly transforming the subtrahend dataset in the frequency domain. A description of the procedure is given next:

a. **Difference Spectra using a Reference Sample (no scaling, no offsetting).** This is the method that would be preferable for UV-Vis spectra. A simple phase alignment (or synchronization) is done by multiplying a modulus-one complex number in the frequency domain. It is readily available from FFT. For spectroscopic datasets A and B transformed into the frequency domain by FFT on the time axis, $\mathbf{V}_\mathrm{A}$ and $\mathbf{V}_\mathrm{B}$ represent matrices of whole datasets. Here, each of $\mathbf{S}_\mathrm{A}$ and $\mathbf{S}_\mathrm{B}$ represents data within a range of wavelengths (or wavenumbers) that may be used as "internal standards" to synchronize phases of oscillations. A vector of phase differences averaged on the wavelength axis, $\delta = \overline{\Delta\boldsymbol{\phi}}$, can be calculated from the arguments of the complex matrices (where $\arg \mathbf{S}_\mathrm{A}$ represents the element-wise argument of $\mathbf{S}_\mathrm{A}$)

$$\Delta\boldsymbol{\phi} = \arg \mathbf{S}_\mathrm{A} - \arg \mathbf{S}_\mathrm{B}.$$

Then, a phase rotation

$$\exp(\mathrm{i}\delta)$$

can be multiplied to the subtrahend dataset $\mathbf{V}_\mathrm{B}$, to obtain the difference dataset, both in the frequency domain,

$$\mathbf{V}_\mathrm{diff} = \mathbf{V}_\mathrm{A} - \mathrm{diag}(\exp(\mathrm{i}\delta)) \times \mathbf{V}_\mathrm{B}$$

Where the multiplication is aligned to the frequency axis. This dataset can be IFFT'ed back to obtain the difference spectra in either time or phase domain.

b. **Difference Spectra using a Scaled Reference Sample.** A similar method can be applied to cases requiring phase alignment, scaling, and offsetting the subtrahend dataset. This can be performed using a different linear transformation replacing $\mathrm{diag}(\exp(\mathrm{i}\delta)) \times \mathbf{V}_\mathrm{B}$ in (a) by frequency-wise linear transformation $\boldsymbol{v}'_\mathrm{B} = a_\mathrm{s}\boldsymbol{v}_\mathrm{B} + b_\mathrm{s}\mathbf{1}$. Here, $\boldsymbol{v}_\cdot$ is a vector from the matrix $\mathbf{V}_\cdot$ for each frequency. Also, the complex factors a_s and b_s can match $\boldsymbol{v}_\mathrm{B}$ to the scale of $\boldsymbol{v}_\mathrm{A}$ while aligning the phase of $\boldsymbol{v}_\mathrm{B}$ to that of $\boldsymbol{v}_\mathrm{A}$. These factors may be obtained using the least square (LSQ) method as follows:

$$\text{LSQ} \left\| \boldsymbol{v}_{\mathrm{A}} - \boldsymbol{v}'_{\mathrm{B}} \right\| = \left\| \boldsymbol{v}_{\mathrm{A}} - (a_{\mathrm{s}} \boldsymbol{v}_{\mathrm{B}} + b_{\mathrm{s}} \mathbf{1}) \right\|$$

Where vector $\mathbf{1}$ has all unity elements and the same shape as $\boldsymbol{v}_{\mathrm{A}}$ and $\boldsymbol{v}_{\mathrm{B}}$. The solution to this LSQ problem is given by:

$$a_{\mathrm{s}} = \frac{\boldsymbol{v}_{\mathrm{A}}^{\mathbf{H}} \boldsymbol{v}_{\mathrm{B}} - \boldsymbol{v}_{\mathrm{A}}^{\mathbf{H}} \mathbf{1}\mathbf{1}^{\mathbf{H}} \boldsymbol{v}_{\mathrm{B}}}{\boldsymbol{v}_{\mathrm{A}}^{\mathbf{H}} \boldsymbol{v}_{\mathrm{A}} - \boldsymbol{v}_{\mathrm{A}}^{\mathbf{H}} \mathbf{1}\mathbf{1}^{\mathbf{H}} \boldsymbol{v}_{\mathrm{A}}}$$

$$b_{\mathrm{s}} = \frac{\boldsymbol{v}_{\mathrm{A}}^{\mathbf{H}} \boldsymbol{v}_{\mathrm{A}} \mathbf{1}^{\mathbf{H}} \boldsymbol{v}_{\mathrm{B}} - \boldsymbol{v}_{\mathrm{A}}^{\mathbf{H}} \boldsymbol{v}_{\mathrm{B}} \mathbf{1}^{\mathbf{H}} \boldsymbol{v}_{\mathrm{A}}}{\boldsymbol{v}_{\mathrm{A}}^{\mathbf{H}} \boldsymbol{v}_{\mathrm{A}} - \boldsymbol{v}_{\mathrm{A}}^{\mathbf{H}} \mathbf{1}\mathbf{1}^{\mathbf{H}} \boldsymbol{v}_{\mathrm{A}}}$$

Where $\mathbf{A}^{\mathbf{H}}$ is the Hermitian transpose of $\mathbf{A}$.

S7.2.3. Example of Au/TiO_2 – TiO_2 Difference Spectra in The Frequency Domain (no scaling, no offsetting).

The difference spectra between Au/TiO_2 and TiO_2 exposed to the same O_2 MES reaction conditions was performed as described in **Section S7.2.2a**. If we take the time domain data for the Au/TiO_2 (e.g., **Figures S12A**, **S12C**, **S13A**, **S13C**) and TiO_2 (e.g., **Figures S12B**, **S12D**, **S13B**, **S13D**) and perform:

a. Fourier transform to the frequency domain (i.e., via FFT)
b. Phase correction of both data sets
c. Subtraction of phase corrected TiO_2 from Au/TiO_2
d. Back conversion into the time domain (i.e., via IFFT)

Then, we obtain **Figure S18** for the TiO_2 corrected Au/TiO_2 time domain responses for 570 and 900 nm. Note that the new corrected Au/TiO_2 spectra in **Figure S18** is shifted down (vs **Figures S12A**, **S12C**, **S13A**, **S13C**) an amount equivalent to that of the support absorbance (e.g., **Figures S12B**, **S12D**, **S13B**, **S13D**).

S18A: Support Corrected Au/TiO_2 Time Domain Spectra (570 nm Selected)

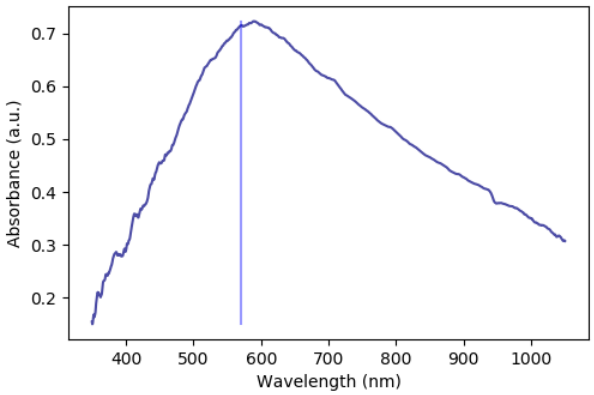

S18B: Support Corrected Au/TiO_2 Time Domain Spectra (900 nm Selected)

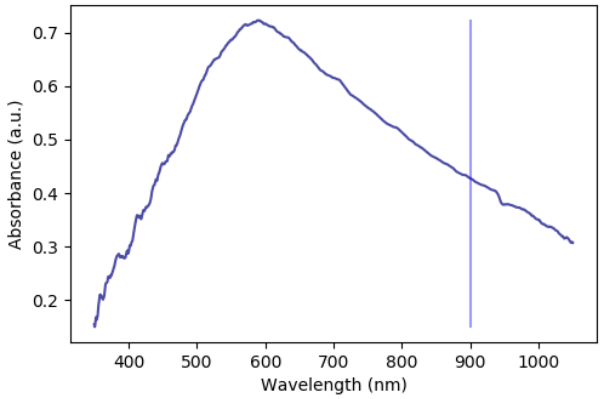

S18C: Support Corrected Au/TiO_2 570 nm Time Domain Response

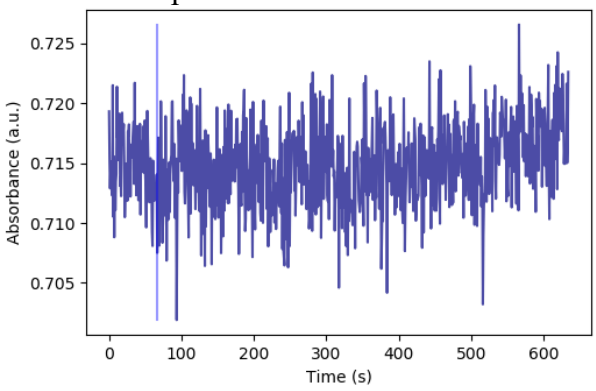

S18D: Support Corrected Au/TiO_2 900 nm Time Domain Response

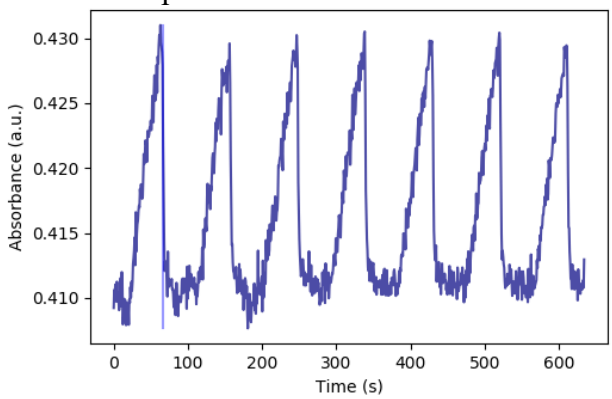

Figure S18. A, B) Support corrected time domain UV-Vis spectra (after ~70 s) with wavelength selected at 570 and 900 nm, respectively, during O_2 ME-PSD-DR-UV-Vis on Au/TiO_2. C, D) Support corrected time domain absorbance response for 570 and 900 nm, respectively, during O_2 ME-PSD-DR-UV-Vis on Au/TiO_2. Reaction conditions: 240 ºC, modulation frequency of 1/90 Hz, He + EtOH (1kPa) → He + EtOH(1kPa) + O_2(1.5kPa).

The support corrected Au/TiO_2 data in the phase domain is presented in **Figure S19**. As expected, the difference spectra trace plot (**Figure S19A** vs **Figure S16A**) shows an identical response in the d-d transition region with respect to that of the unreferenced Au/TiO_2. This is because the support response to modulation was minimal and PD shows only the relative changes with respect to a reference value, the middle point of a modulation period. In other words, the support corrected Au/TiO_2 time domain data at 900 nm (**Figure 18D**) is similar to the corresponding uncorrected data (**Figure S13C**) but simply shifted down an amount equivalent to that by the support response (**Figure S13D**).

S16A: Uncorrected Au/TiO_2 Phase Domain – Trace Plot

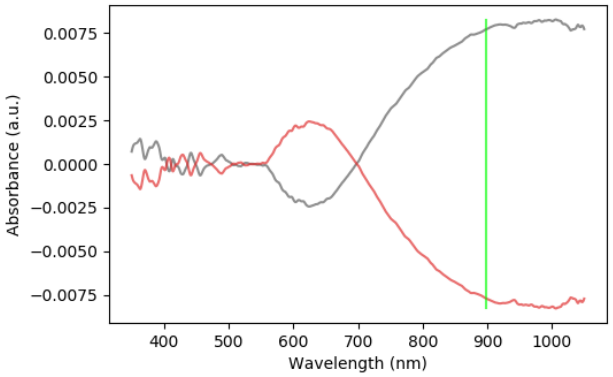

S16C: Uncorrected Au/TiO_2 Frequency Domain @ 900 nm

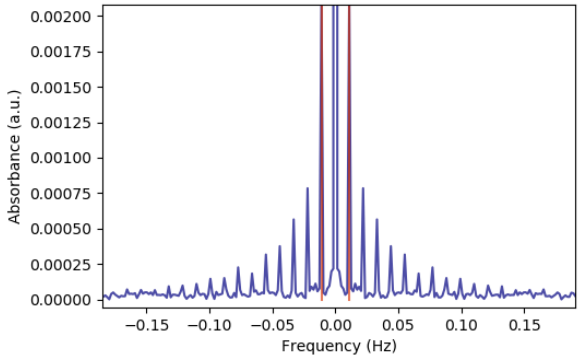

S19A: Support Corrected Au/TiO_2 − TiO_2 Difference Spectra in Phase Domain Trace Plot

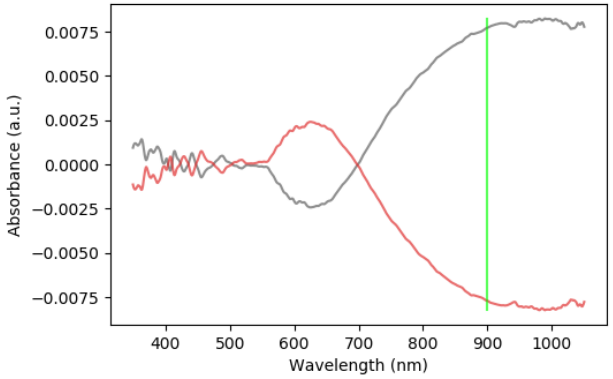

S19B: Support Corrected Au/TiO_2 − TiO_2 Frequency Domain @ 900 nm

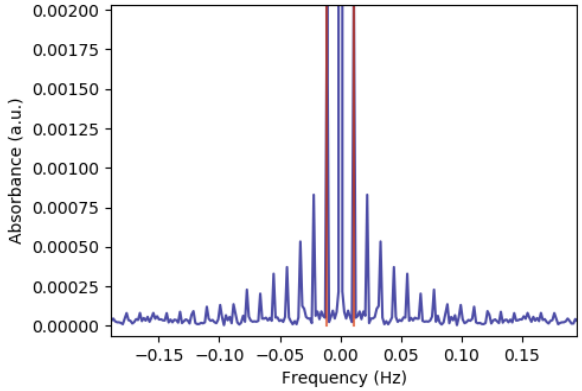

Figure S19. A) Phase domain trace plot filtered at the fundamental frequency during O_2 ME-PSD-DR-UV-Vis on Au/TiO_2 corrected by TiO_2 reference after a difference spectra procedure in the frequency domain. For clarity, only the highest and lowest absorbance traces are shown. B) Frequency domain plot evaluated at 900 nm for the Au/TiO_2 − TiO_2 difference spectra. Analysis performed using modulation data in **Figure S13**. Reaction conditions: 240 °C, modulation frequency of 1/90 Hz, He + EtOH (1kPa) → He + EtOH (1kPa) + O_2 (1.5kPa). Unreferenced Au/TiO_2 in **Figures S16A** and **S16C** are shown for comparison.

References

[1] J.B. Rawlings, J.G. Ekerdt, Chemical reactor analysis and design fundamentals, Nob Hill, Madison, WI, 2002.

[2] T.F. Edgar, D.M. Himmelblau, L.S. Lasdon, Optimization of chemical processes, 2nd ed., McGraw-Hill, New York, NY, USA, 2001.

[3] A. Carlsson, A. Puig-Molina, T.V.W. Janssens, New method for analysis of nanoparticle geometry in supported fcc metal catalysts with scanning transmission electron microscopy, J. Phys. Chem. B, 110 (2006) 5286-5293.

[4] P.D. Srinivasan, H. Zhu, J.J. Bravo-Suárez, In situ UV–vis plasmon resonance spectroscopic assessment of oxygen and hydrogen adsorption location on supported gold catalysts, Mol. Catal., 507 (2021) 111572.

[5] P.D. Srinivasan, B.S. Patil, H. Zhu, J.J. Bravo-Suárez, Application of modulation excitation-phase sensitive detection-DRIFTS for in situ/operando characterization of heterogeneous catalysts, React. Chem. Eng., 4 (2019) 862-883.

[6] P.D. Srinivasan, S.R. Nitz, K.J. Stephens, E. Atchison, J.J. Bravo-Suárez, Modified harrick reaction cell for in situ/operando fiber optics diffuse reflectance UV–visible spectroscopic characterization of catalysts, Appl. Catal., A, 561 (2018) 7-18.

[7] B.S. Patil, P.D. Srinivasan, E. Atchison, H. Zhu, J.J. Bravo-Suárez, Design, modelling, and application of a low void-volume in situ diffuse reflectance spectroscopic reaction cell for transient catalytic studies, React. Chem. Eng., 4 (2019) 667-678.